A method for searching for ultrarelativistic magnetic monopoles with the Very Energetic Radiation Imaging Telescope Array System (VERITAS)

Leandro Rizk

Department of Physics

McGill University

Montréal, Québec

August 2025

A thesis submitted to McGill University in partial fulfillment of

the requirements of the degree of Master of Science

Abstract

Magnetic monopoles (MMs) are hypothesized particles that bear only a north or south magnetic pole. Under a certain mass limit ($< 10^8$ GeV/c^2), cosmic MMs are plausibly accelerated to ultrarelativistic speeds ($\gamma > 10^3$) by galactic magnetic fields over large timescales. If such a magnetically charged particle traverses the Earth, it is expected to emit Cherenkov radiation in the atmosphere with an intensity 4700 times greater than an ultrarelativistic particle that carries an elementary electric charge. Imaging atmospheric Cherenkov telescopes—designed to detect very-high-energy gamma rays by the Cherenkov radiation emitted when they produce electromagnetic showers—should also be able to detect ultrarelativistic MMs. In this work, simulations of ultrarelativistic MMs in the atmosphere are built using the Cosmic Ray Simulations for Kascade (CORSIKA) program to study how their signal would be detected by the Very Energetic Radiation Imaging Telescope Array System (VERITAS). A dedicated search through VERITAS archival data is also discussed.

Sommaire

Les monopôles magnétiques (MM) sont des particles hypothétiques qui ne portent qu'un seul pôle nord ou sud magnétique. En deçà d'une certaine masse ($< 10^8$ GeV/c^2), les MM cosmiques pourraient bien être accélérés à des vitesses ultrarelativistes ($\gamma > 10^3$) grâce aux champs magnétiques galactiques, sur de grandes échelles de temps. Si l'une de ces particules de charge magnétique traversait la Terre, elle émettrait vraisemblablement un rayonnement Tcherenkov dans l'atmosphère avec une intensité 4700 fois supérieure à ce que ferait une particule utlrarelativiste de charge électrique élémentaire. Les télescopes à imagerie Tcherenkov atmosphériques, conçus pour détecter les rayons gamma de très haute énergie par le rayonnement Tcherenkov émis lorsqu'ils produisent des cascades électromagnétiques, devraient aussi être capables de détecter les MM ultrarelativistes. Dans cet ouvrage, des simulations de MM ultrarelativistes dans l'atmosphère sont construites avec le programme Cosmic Ray Simulations for Kascade (CORSIKA) afin d'étudier la façon dont leur signal serait détectable par le réseau Very Energetic Radiation Imaging Telescope Array System (VERITAS). Une recherche spécialisée dans les archives de VERITAS est aussi abordée.

Acknowledgements

I would first and foremost like to thank my supervisor, Prof. Kenneth Ragan, for his kindness and compassion, for his advice, and for his guidance throughout my time at McGill. A special thanks is owed to Matthew Lundy, who gave me the idea and plan for this project and who helped me on too many occasions to name, even when he was busy with his own thesis. Many thanks to Stephan O'Brien for assisting me countless times with Eventdisplay and for helping me write a very useful script for my simulations. Thank you to Samantha Wong for her insight and feedback not only in this work but also in other VERITAS projects, especially those involving Gammapy. I would like to acknowledge Juan Gallego for his help in finding solutions to seemingly impossible problems in the computer systems. Thank you as well to Gernot Maier for answering my questions about Eventdisplay and `VTS-SimPipe` and, of course, for his work in developing the software. Thank you to Prof. Simon Caron-Huot for a helpful discussion on magnetic monopoles early on. I also would like to recognize the work done every day by the staff at the Trottier Space Institute and the McGill Physics Department. Finally, I would like to thank my family and friends for their unwavering support.

Table of contents

List of figures

List of tables

List of abbreviations

AMANDA-II The Antarctic Muon And Neutrino Detection Array

ANTARES The Astronomy with a Neutrino Telescope and Abyss environmental RESearch project

BDUNT The Baikal Deep Underwater Neutrino Telescope

C.L. Confidence level

CARE CAmera and REadout

CERN The European Organization for Nuclear Research

CFD Constant fraction discriminator

CORSIKA COsmic Ray SImulations for KAscade

CTAO The Cherenkov Telescope Array Observatory

d.c. Digital counts

DL Data level

EAS Extensive air shower

ED Eventdisplay

EM Electromagnetic

FOV Field of view

GUT Grand Unified Theory

H.E.S.S. The High Energy Stereoscopic System

IACT Imaging atmospheric Cherenkov telescope

IMM Intermediate-mass (magnetic) monopole

KASCADE The KAarlsruhe Shower Core and Array DEtector

L Level # (of the VERITAS trigger system)

LHC Large Hadron Collider

MACRO The Monopole, Astrophysics and Cosmic Ray Observatory

MAGIC The Major Atmospheric Gamma Imaging Cherenkov Telescopes

MM Magnetic monopole

NSB Night sky background

PMT Photomultiplier tube

RHV Reduced high voltage

RICE The Radio Ice Cherenkov Experiment

SLIM The Search for Light Monopoles experiment

SM Standard Model

UV ultraviolet

VBF VERITAS bank format

VERITAS The Very Energetic Radiation Imaging Telescope Array System

VHE Very-high-energy

Contributions of the author

- **Chapters 1 through 5:** The literature review (magnetic monopoles, Cherenkov radiation, imaging atmospheric Cherenkov telescopes, and muon ring images) was performed by the author.
- **Chapter 6:** The author installed CORSIKA, GrOptics, and CARE and used them to build simulations of muons and magnetic monopoles. The plan was conceived by the author. The author had no hand in the development of the simulation software.
- **Chapter 7:** The author analyzed the simulation results with Eventdisplay. Three VERITAS observation runs were also analyzed by the author. The analyzed real data runs were not taken by the author; however, the author has taken on observing shifts at VERITAS, gathering data for other science goals of the collaboration. The author had no hand in the development of Eventdisplay.
- **Chapters 8 and 9:** The interpretation of the results and the discussion on expanding the method as well as on prospects for the future are the original work of the author.

Chapter 1

Introduction

In all our observations of magnetism, magnetic fields arise from the motion of electric charges and changes in electric fields. There are currently no known physical examples of a "magnetic charge," consisting of an isolated north or south pole, which acts as a source or sink of magnetic fields [1]. Yet, if they exist, magnetically charged particles—termed "magnetic monopoles" (MMs)—would have interesting properties and would be, in one way or another, a gateway to new physics.

One of the more remarkable characteristics attributed to MMs is an exaggerated Cherenkov effect when they travel at relativistic speeds through a dielectric medium [2]. This property has been the focus of targeted monopole searches in many experiments.

Under the assumption that ultrarelativistic MMs (with a Lorentz factor of 10^3 or greater) behave in Earth's atmosphere similarly to highly energetic muons, their strong Cherenkov effect could be picked up by the muon detection software of imaging atmospheric Cherenkov telescopes (IACTs). In this work, CORSIKA [3] simulations of MMs are built to understand how they would be observed with the Very Energetic Radiation Imaging Telescope Array System (VERITAS).

While VERITAS is an IACT array constructed for the study of gamma rays, it may also have the potential to serve as a MM detector. With over 10,000 hours of observations taken

since 2007, VERITAS data might contain the signal of a MM waiting to be found. If the data is searched and no signal is identified, an experimental constraint can be placed on the flux of ultrarelativistic MMs. In this work, three VERITAS observation runs (totaling 80 minutes) are analyzed as a demonstration of the method developed herein to search for MMs.

This thesis is organized as follows: Chapter 2 introduces MMs and describes their expected properties, Chapter 3 specifically covers Cherenkov radiation, and Chapter 4 presents the most notable past searches of MMs of cosmic origin. Chapter 5 is a presentation of the VERITAS observatory and the science that underlies its operation. Chapter 6 covers the methodology behind the MM simulations and the choices that are made. Finally, results are presented in Chapter 7 and discussed in Chapter 8, with a look at future possibilities.

Chapter 2

Magnetic monopoles

2.1 Expanding Maxwell's equations

Maxwell famously revolutionized 19th century physics by combining Gauss's law, Faraday's law, and an improved Ampère's law into a system of four equations which describe electricity and magnetism as the same force [1]:

$$\vec{\nabla} \cdot \vec{E} = 4\pi\,\rho \tag{2.1}$$

$$\vec{\nabla} \cdot \vec{B} = 0 \tag{2.2}$$

$$\vec{\nabla} \times \vec{E} = -\frac{1}{c}\frac{\partial \vec{B}}{\partial t} \tag{2.3}$$

$$\vec{\nabla} \times \vec{B} = \frac{1}{c}\frac{\partial \vec{E}}{\partial t} + \frac{4\pi}{c}\,\vec{J}\,. \tag{2.4}$$

In the above expressions, $\vec{E}$ is electric field, $\vec{B}$ is magnetic field, ρ is electric charge density, $\vec{J}$ is electric charge current density, and c is the speed of light. Note that these equations and all others in this work are expressed in Gaussian units. In this realm, the unit for electric charge is the statcoulomb (statC), which is equivalent to $\mathrm{g}^{1/2}\ \mathrm{cm}^{3/2}\ \mathrm{s}^{-1}$.

Maxwell's equations are striking in that their descriptions of the electric field $\vec{E}$ and the magnetic field $\vec{B}$ are nearly symmetric. In fact, introducing additional terms to equations (2.2) and (2.3) would render equations (2.1) and (2.2) perfectly symmetric while mak-

ing equations (2.3) and (2.4) antisymmetric. With this, Maxwell's equations become [4]

$$\vec{\nabla} \cdot \vec{E} = 4\pi\,\rho$$

$$\vec{\nabla} \cdot \vec{B} = 4\pi\,\rho_m \tag{2.5}$$

$$\vec{\nabla} \times \vec{E} = -\frac{1}{c}\frac{\partial \vec{B}}{\partial t} - \frac{4\pi}{c}\,\vec{J}_m \tag{2.6}$$

$$\vec{\nabla} \times \vec{B} = \frac{1}{c}\frac{\partial \vec{E}}{\partial t} + \frac{4\pi}{c}\,\vec{J}.$$

In the above system, ρ_m represents a magnetic charge density and $\vec{J}_m$ represents a magnetic charge current density (i.e., the flux of magnetic charges). Both these terms imply the existence of a net magnetic charge: a single north pole without an accompanying south pole (or vice versa). The use of Gaussian units highlights the symmetry between ρ and its magnetic counterpart ρ_m and between $\vec{J}$ and $\vec{J}_m$, as these pairs are expressed in the same units ($\mathrm{g}^{1/2}\ \mathrm{cm}^{-3/2}\ \mathrm{s}^{-1}$ and $\mathrm{g}^{1/2}\ \mathrm{cm}^{-1/2}\ \mathrm{s}^{-2}$ respectively).

Mathematically, these equations are entirely self-consistent; nonetheless, there are currently no known physical manifestations of objects that bear a net magnetic charge. All magnets observed in the Universe are—at minimum—magnetic dipoles, having both a north and south pole, and are fundamentally the result of moving electric charges and varying electric fields (as described by equation (2.4)) [1]. There has been no convincing evidence of one of these poles being found isolated from the other. However, this has not dissuaded the many searches for a possible "magnetic monopole" (MM), a particle bearing a magnetic charge (see Chapter 4). These searches are not only motivated by the attainment of another natural symmetry; MMs can provide a justification for the quantization of electric charge [5]. Furthermore, a form of MMs is a prediction of Grand Unified Theories (GUTs) [6, 7], and MMs could also potentially make up some of the "missing mass" (dark matter) predicted to exist in the Universe [8].

2.2 The Dirac charge

The Dirac charge is the magnetic counterpart to quantized electric charge. In an effort to explain the quantization of both the elementary electric charge e and a possible elementary magnetic charge g, Dirac proposed in 1931 [5] that

$$\frac{e\,g}{c} = \mathrm{n}\,\frac{\hbar}{2}\,, \tag{2.7}$$

for some integer n. In this relation, the product of the two elementary charges is restricted to half-integer units of the reduced Planck's constant ($\hbar$). Considering the minimal case where n is unity, the Dirac charge is equal to

$$g = \frac{\hbar\,c}{2\,e} \approx 68.5\,e\,, \tag{2.8}$$

where the fine structure constant $\alpha = e^2/(\hbar c) \approx 1/137$ was used to convert away the other constants. In Dirac's definition, g is at minimum about two orders of magnitude larger than e.

2.3 Proposed monopole types

There are three main proposed types of MMs, which characterize their structure, mass, and properties: the classical MM, the GUT MM, and the intermediate-mass MM (IMM).

2.3.1 The classical magnetic monopole

The classical MM (also known as the Dirac monopole) would be a beyond-Standard Model (SM) fundamental point particle bearing a Dirac charge g. If we suppose that its radius is comparable to that of the classical electron radius r_e, defined as

$$r_e = \frac{e^2}{m_e\,c^2}\,, \tag{2.9}$$

where $m_e \approx 0.511$ MeV$/c^2$ is the mass of the electron, we can determine a mass scale for the classical MM [8]. The mass of the classical MM m_{MM} can be approximated as

$$m_{\mathrm{MM}} \sim \frac{g^2}{e^2} m_e \approx (68.5)^2 m_e \,. \tag{2.10}$$

This gives a value on the order of 2.4 GeV$/c^2$ for m_{MM}. At this mass scale, the MM can be probed by collider experiments, such as the Large Hadron Collider (LHC) at CERN. Collider searches have so far not yielded a particle consistent with a MM, even at centre-of-mass collisional energies as high as 13 TeV [8–10]. Searches for a classical MM with the LHC continue to be an active area of study. However, given the differences in experimental approach, the search for this proposed type of monopole will not be discussed further in this work.

2.3.2 The GUT magnetic monopole

The GUT MM is the type of monopole that is predicted to have been formed at $\sim 10^{-34}$ seconds after the Big Bang, during the phase transition from the GUT era to the electroweak era. According to current understanding in cosmology, the GUT era preceded cosmic inflation and was characterized by a universe so dense and hot ($k_B T \gtrsim 10^{16}$ GeV) that the three SM forces—strong, weak, and electromagnetic (EM)—were unified [11]. In the subsequent electroweak era, the strong interaction became distinct from the other two forces (still unified as the electroweak interaction). The symmetry breaking

$$\mathrm{SU}(5) \xrightarrow{k_B T < 10^{15}\,\mathrm{GeV}} \mathrm{SU}(3)_C \times [\mathrm{SU}(2)_L \times \mathrm{U}(1)_Y]^{\,*}$$

would give rise to one GUT MM as a topological defect for each causal domain [8, 9]. This immediately poses a problem: GUT MMs would consequently be overabundant—to the point where their density would exceed the critical density of the Universe. This cosmological incongruence is called the "monopole problem" and it is one of the problems

*In this expression, SU(5) is the special unitary group of the unified force, which breaks into the groups $\mathrm{SU}(3)_C$ (the strong force) and $[\mathrm{SU}(2)_L \times \mathrm{U}(1)_Y]$ (the electroweak force). The subscript C stands for "colour," L is for "left," and Y represents weak hypercharge.

solved by the postulation of cosmic inflation [11]. Inflation in the early universe would dilute GUT MMs from this formidable density to a density so low that they may in fact never be plausibly detectable.

Corresponding to the very large energy scale of the GUT-electroweak transition, GUT MMs would retain an energy (and therefore mass) of 10^{16} to 10^{17} GeV [9]. This tremendous mass would impede any acceleration induced on them by galactic magnetic fields. GUT MMs would thus remain gravitationally bound to the Galaxy (for MMs with speeds $\beta \sim 10^{-3}$), the Sun ($\beta \sim 10^{-4}$), or the Earth ($\beta \sim 10^{-5}$) [9].

One interesting property of GUT MMs is that they would retain the ability of violating baryon number conservation that is characteristic of the GUT era [8,9]. As a result of this, a GUT MM travelling through baryonic matter would be able to catalyze proton decay. This astonishing property is in fact the focus of some dedicated monopole searches.

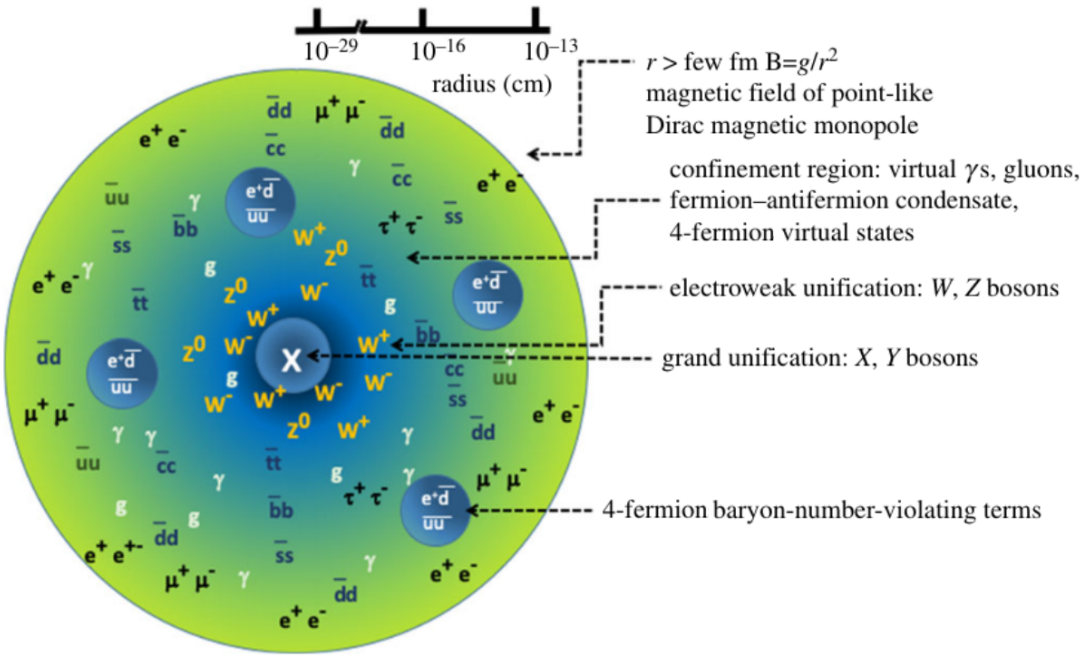

Figure 2.1: Internal structure of a GUT magnetic monopole. Taken from [9].

A GUT MM would be a composite particle made up of a GUT boson trapped in the centre, surrounded by layers of force bosons and fermions. A single MM would have a radius on the order 10^{-13} cm (1 fm). Contained within this radius are four-fermion condensates, which act as the baryon-number violating regions of the GUT MM [8, 9]. The structure of this object is illustrated in Figure 2.1.

2.3.3 The intermediate-mass magnetic monopole

IMMs are similar to GUT MM, except they would be produced at a later phase transition in the early universe. IMMs could have masses on the order of 10^5 to 10^{13} GeV/c^2 [9]. In contrast with GUT MMs, IMMs created in the early universe would not be diluted to minuscule densities because they would arise after inflation [8]. Since a MM behaves in a magnetic field the way an electron would behave in an electric field, MMs are accelerated in the direction of galactic field lines, not deflected around those lines. Over the coherent length of a galactic magnetic field, an IMM can plausibly reach ultrarelativistic velocities (defined in this work as having $\gamma > 10^3$) [8,9].

If all an IMM's kinetic energy is provided by a galactic magnetic field as the monopole travels along field lines, the maximum mass $m_{\max}$ that would allow it to reach a (minimum) Lorentz factor γ can be estimated with

$$m_{\max} = \frac{g\,B\,L}{(\gamma - 1)\,c^2}\,, \tag{2.11}$$

where B is the magnetic field strength and L its coherent length. Equation (2.11) is obtained by equating a monopole's kinetic energy $(\gamma - 1)\,m\,c^2$ with the work done on it by the magnetic field $g\,B\,L$, which is analogous to the work done by an electric field on an electric charge. Assuming very little monopole energy loss in the interstellar medium and choosing typical values of $B \approx 3 \times 10^{-6}$ G and $L \approx 10^{21}$ cm (approximately 300 pc) [8,9] reveals that an IMM of mass $\lesssim 10^{10}$ GeV/c^2 can reach a Lorentz factor of $\gamma = 50$[†]. For an

[†]This is around the minimum γ necessary for a charged particle to produce Cherenkov radiation in air at sea level, as will be discussed in Chapter 3.

ultrarelativistic $\gamma = 10^3$ or greater, an IMM would probably have to be no more massive than 10^8 GeV/c^2.

Contrary to GUT MMs, IMMs would not be able to catalyze nucleon decay [8,9]. However, relativistic and ultrarelativistic MMs are expected to be responsible for an exaggeratedly intense Cherenkov effect in their path through a dielectric medium (see Chapter 3). Structurally, an IMM is very similar to a GUT MM, with the notable exception of having no baryon-number violating regions [8,9]. The IMM structure is illustrated in Figure 2.2.

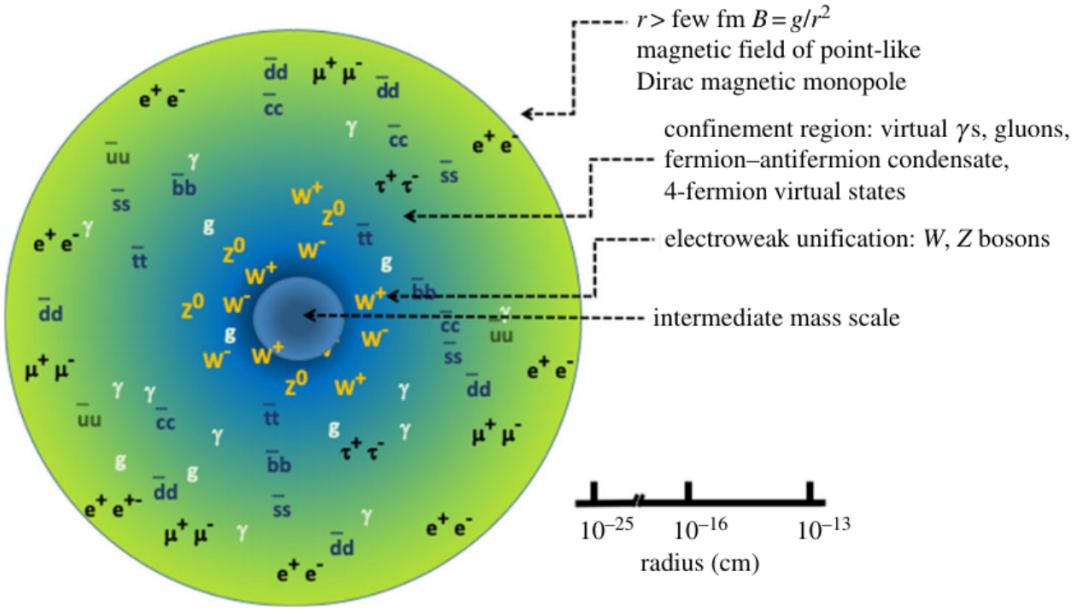

Figure 2.2: Internal structure of an intermediate-mass magnetic monopole. Taken from [9].

Table 2.1 presents a summary of the three different types of monopoles.

Table 2.1: Properties of different proposed types of magnetic monopoles

	Classical monopole	GUT monopole	Intermediate-mass monopole
Point-like or composite	Point-like	Composite	Composite
Mass range ($\log[\mathrm{GeV}/c^2]$)	~ 0	16 – 17	5 – 13
Context of creation	Unknown	GUT-to-electroweak phase transition	Phase transition later than GUT
Ability to induce nucleon decay	No	Yes	No
Likelihood to be observed with relativistic speed	Likely	Unlikely	Likely (for masses $\lesssim 10^{10}$ GeV/c^2)

2.4 Bounds on magnetic monopole flux

The flux of cosmic MMs detectable on Earth is weakly limited by theory. Two such upper limits are explored in this section: an essential bound from critical density and a bound imposed by galactic magnetic fields.

2.4.1 Critical density

To start at the most basic limit, we can be sure that the universal density of MMs cannot exceed the critical density of the Universe. This upper limit on MM density gives us a starting point for the flux of cosmic MMs for a potential detector on Earth.

Requiring the number density of cosmic MMs n_{MM} to be smaller than the critical density ρ_c divided by the monopole mass gives us an upper limit on the number flux Φ_{MM}. This flux, defined as the number of MMs (N) per detection area (A) per unit time (t) per solid angle of the sky (Ω), must have the constraint [8]

$$\Phi_{\mathrm{MM}}^{\mathrm{crit}} = \frac{dN}{dA\,dt\,d\Omega} = \frac{n_{\mathrm{MM}}\,\beta\,c}{4\pi} < \frac{\rho_c\,c}{4\pi}\,\frac{\beta}{m}$$

$$\Phi_{\mathrm{MM}}^{\mathrm{crit}} \lesssim 2.5\times 10^{-13}\,\mathrm{h}^2\,\frac{\beta}{m\,/\,(10^{17}\,\mathrm{GeV}/c^2)}\,\mathrm{cm}^{-2}\,\mathrm{s}^{-1}\,\mathrm{sr}^{-1}\,, \tag{2.12}$$

where $\mathrm{h} \approx 0.7$ is the dimensionless Hubble constant [12]. This limit is a function of both the mass m and relative speed β of MMs.

2.4.2 The Parker bound

MMs are accelerated by galactic magnetic fields. Consequently, they cannot be so abundant as to deplete galactic fields of their energy; otherwise, these fields would not be observed. The maximum energy acquired by MMs must therefore be less than the magnetic energy generated by the dynamo effect. The dynamo effect is approximated by the energy density of the galactic magnetic field ρ_B divided by the galactic rotation period τ. As such, the energy generated per unit volume per unit time is

$$\frac{dE_{\mathrm{dynamo}}}{dt\,dV} = \frac{\rho_B}{\tau} = \frac{B^2}{8\pi}\,, \tag{2.13}$$

where B is again the galactic magnetic field strength [8].

Energy transferred to MMs is $\vec{J}_{\mathrm{MM}} \cdot \vec{B}$ and cannot exceed the value given by equation (2.13). The MM current volume density $\vec{J}_{\mathrm{MM}}$ is equal to $g\, n_{\mathrm{MM}}\, \vec{v}$ (for some characteristic MM velocity $\vec{v}$). With this—and if we consider that cosmic MMs will travel largely in the direction of magnetic field lines—, we obtain an upper limit on the MM flux

$$\Phi_{\mathrm{MM}}^{\mathrm{Parker}} \lesssim \frac{B}{32\pi^2\,\tau\,g} \approx 10^{-16}\,\mathrm{cm}^{-2}\,\mathrm{s}^{-1}\,\mathrm{sr}^{-1}\,. \tag{2.14}$$

This upper limit imposed by the persistence of galactic magnetic fields is called the Parker bound [13]. A more careful analysis by Turner et al. [14] brings the Parker bound closer to about 10^{-15} cm^{-2} s^{-1} sr^{-1} by considering the random relation between MM direction and magnetic field lines and choosing reasonable astrophysical parameters. It is this looser value that is recurrently quoted as the benchmark for MM searches. Note that, contrary to the previous limit (equation (2.12)), the Parker bound is independent of MM mass and speed.

Primordial magnetic fields are expected to be greatly diluted by the expansion of the Universe. Taking into account the survival of an early seed of the galactic magnetic field, one can also define an "extended Parker bound"

$$\Phi_{\rm MM}^{\rm extd\ Parker} \lesssim 1.2 \times 10^{-16} \left(\frac{m}{10^{17}\,{\rm GeV}/c^2} \right) {\rm cm}^{-2}\,{\rm s}^{-1}\,{\rm sr}^{-1}\,, \tag{2.15}$$

which becomes a function of the monopole mass [15].

2.5 Magnetic monopole energy loss

Any strong interactions MMs might have with matter are unclear, so this work focuses only on EM interactions. But if these strong interactions occur, they would likely be the dominant interaction [16].

The energy loss of a MM per unit length of matter travelled is described by

$$-\frac{dE}{dx} = a + b\,E\,, \tag{2.16}$$

where a and b are terms that are only weakly dependent on the Lorentz factor $\gamma = 1/\sqrt{1-\beta^2}$ of the MM [17, 18]. Based on models of muon and tau lepton energy losses [19, 20], MM energy loss is divided into two components: a largely energy-independent ionization (the a term) and energy-dependent losses (the b term). This latter component is composed of bremsstrahlung, induction of pair production, and photonuclear interactions [17, 18]. Bremsstrahlung ("braking radiation") is the emission of a photon by a charged particle—in this case, magnetically charged—as it is accelerated (deflected) by the close encounter with an atom in matter. The intensity of this effect is inversely proportional to the square of the mass of the travelling charged particle [21]. In pair production, the MM is preserved, but part of its energy is lost to the creation of an electron-positron pair. In photonuclear interactions, energy from the MM is transferred in a collision with an atomic nucleus. Of these, bremsstrahlung is likely very negligible given the mass scale of GUT MMs and IMMs, and so it is safe to disregard it [17, 18, 22]. Ionization dominates

below $\gamma \sim 10^4$ while pair production and photonuclear effects are dominant in the ultrarelativistic regime. Figure 2.3 shows the energy loss experienced by a MM in air at different Lorentz factors.

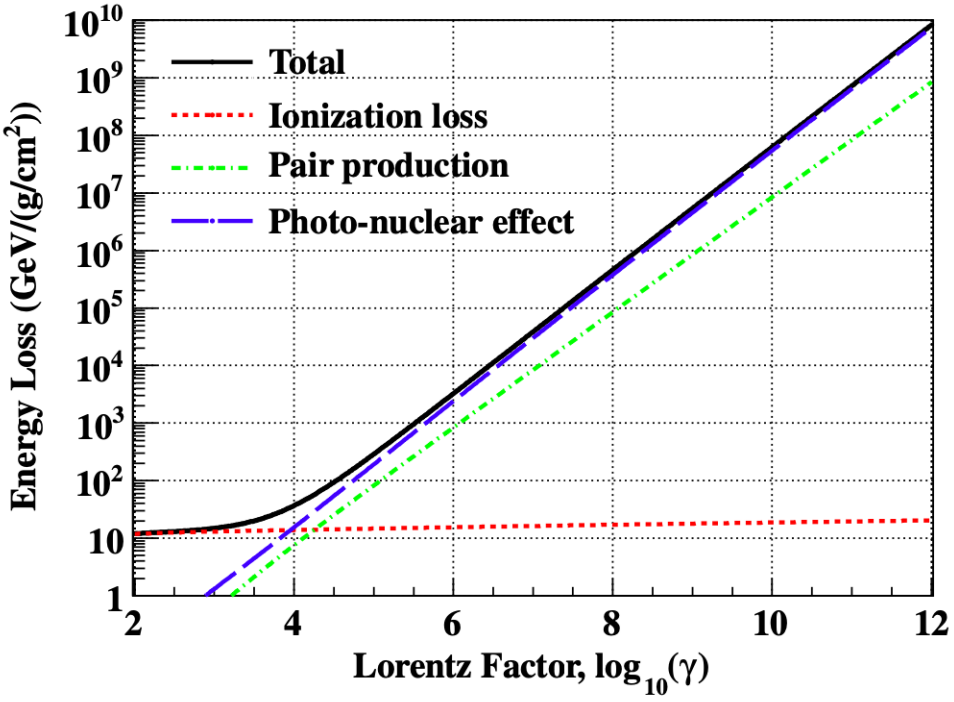

Figure 2.3: Energy loss of a magnetic monopole in air. The solid black curve represents the sum of all the energy loss mechanisms. The dotted red line is the contribution of ionization; it is very weakly dependent on MM energy and is the dominant mechanism below $\gamma \sim 10^4$. The blue and green dot-dashed lines are pair production and photonuclear effects respectively; these energy-dependent mechanisms dominate above $\gamma \sim 10^4$. The contribution of bremsstrahlung (also energy-dependent) remains negligible and is not shown. Taken from [22].

Because an IMM is so massive, it only loses a small fraction of its energy as it travels through matter at ultrarelativistic speeds. Following from Figure 2.3, an IMM with $\gamma \sim 10^4$ (and therefore total energy $\gtrsim 10^9$ GeV) loses only about 30 MeV for every cm travelled in air at sea-level density (1.205×10^{-3} g/cm^3 [23]). At $\gamma \sim 10^{12}$ (total energy

$\gtrsim 10^{17}$ GeV), the energy loss climbs to 10^7 GeV/cm—a tremendous amount to impart to the atmosphere, but still relatively small compared to the energy of the monopole. It is safe to assume that an ultrarelativistic MM reaching the Earth would not be effectively slowed down by the atmosphere [16].

The long-range interaction between a MM and a fermion, nucleus, or atom is due to magnetostatics. The work done on the electrically-charged object is described by

$$W \,=\, -\vec{\mu} \,\cdot\, \vec{B}_{\mathrm{MM}}\,, \tag{2.17}$$

where $\vec{\mu}$ is the magnetic dipole moment of the fermion, nucleus, or atom and $\vec{B}_{\mathrm{MM}}$ is the magnetic field generated by the MM [8]. For an electron interacting with a Dirac charge on the scale of a Bohr atomic radius, the energy of this interaction is comparable to atomic binding energies. We can therefore expect deformation of an atom when a MM passes nearby [8]. For a proton interacting with a Dirac charge at $\sim$1 fm, the interaction energy is greater than nuclear binding energies and so the nucleus can be deformed by a close encounter with a MM [8].

Different models have been proposed for the stopping power of MM slower than $\gamma \sim 100$ in matter. An appropriate model for monopoles with speeds $0.2 < \beta < 1$ follows an adapted Bethe–Bloch formula (proposed by S. P. Ahlen in 1978 [24]):

$$-\frac{dE}{dx} \,=\, \frac{4\pi\, n_e\, g^2\, e^2}{m_e\, c^2}\, \left[\ln\left(\frac{2\, m_e\, c^2\, \beta^2\, \gamma^2}{I}\right) \,-\, \frac{1}{2} \,-\, \frac{\delta}{2} \,+\, \frac{K}{2} \,-\, B\right]. \tag{2.18}$$

In the above equation, n_e is the electron density of the medium, $m_e \approx 0.511$ MeV/c^2 is the electron mass [25], and I is the mean ionization potential of the medium. Also included are correction terms δ (a density effect correction), K (a quantum electrodynamics correction), and B (called the Bloch correction). The density correction term δ is itself a function of β and is dependent on the medium. Methods to determine δ are described by R. M. Sternheimer and R. F. Peierls in [26]. As for K and B, they are respectively set to 0.406 and 0.248 for monopoles bearing a single Dirac charge, according to Ahlen [24].

For a slow MM travelling at $10^{-3} < \beta < 10^{-2}$, the medium is best approximated as a degenerate electron gas for metallic absorbers as well as for non-metallic absorbers with atomic number 10 and greater [8, 27]. The energy loss then follows

$$-\frac{dE}{dx} = \frac{2\pi\, n_e\, g^2\, e^2\, \beta}{m_e\, c\, v_{\rm F}} \left[\ln\left(\frac{2\, m_e\, v_{\rm F}\, a_0}{\hbar}\right) - \frac{1}{2}\right], \tag{2.19}$$

where $a_0 \approx 5.29 \times 10^{-9}$ cm is the Bohr radius and $v_{\rm F} = (\hbar/m_e)\,(3\pi^2 n_e)^{1/3}$ is called the Fermi velocity[‡] of the medium [8]. Equation (2.19) can be further multiplied by a factor of 1.37 to account for the coupling of a MM with an electron's magnetic moment [8]. This formula is useful to evaluate a slow monopole's energy loss through solid Earth but is not a good approximation for the atmosphere (where the predominant elements, nitrogen and oxygen, have atomic number smaller than 10).

MMs with speeds $\beta \lesssim 10^{-3}$ may not be efficient at exciting atoms. Energy loss would be primarily through elastic collisions caused by coupling with magnetic moments of atoms or nuclei. Energy loss through the medium would be released in the form of thermal and acoustic energy [8].

[‡]The Fermi velocity is the speed a fermion has if its kinetic energy is equal to the Fermi energy of a material. The Fermi energy is the energy difference between the highest and lowest states at absolute zero.

Chapter 3

Cherenkov radiation

3.1 Cherenkov radiation from electrically charged particles

In a dielectric medium with refractive index n, a photon only travels at speed c/n. Other particles, however, are not subject to this constraint. With sufficient energy, speeds $v > c/n$ are accessible to massive particles. When a charged particle traverses a dielectric medium faster than light can, there arises a disturbance which results in the production of observable photons [20, 28]. These photons, emitted by the dielectric medium rather than by the offending particle, propagate at an angle with respect to the particle's direction. This happens because the charged particle induces polarization of the surrounding molecules as it passes. As these become polarized and depolarized, they emit an electromagnetic (EM) pulse [28]. Unlike the case of the slow-moving charge, where the polarization remains symmetric along the path of travel (see Figure 3.1(a)), the pulses interfere destructively in all directions except at one angle related to the particle's velocity (see Figures 3.1(b) and 3.2). The resulting observable wavefront is called Cherenkov radiation (or Cherenkov–Vavilov radiation), named for the scientist who first described the phenomenon in 1934 [29]. For his discovery, Pavel Cherenkov was awarded the 1958 Nobel Prize in Physics, which he shared with Il'ja Frank and Igor Tamm for their interpretation of the effect [30]. The Cherenkov effect has been an indispensable detection tool for many particle and astroparticle experiments.

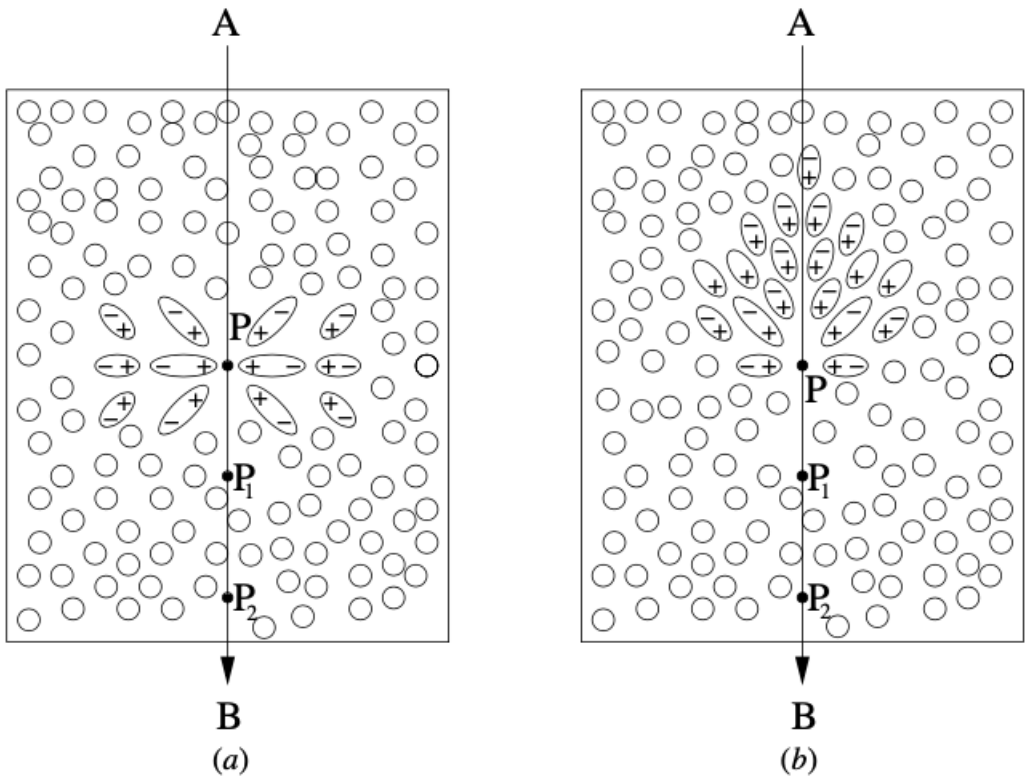

Figure 3.1: Polarization of a dielectric medium induced by the passage of a negatively charged particle. (a) Case of a slow-moving charged particle. (b) Case of a charged particle travelling at $v > c/n$. Taken from [28].

In the wake of a particle travelling at $\beta > 1/n$, the angle at which Cherenkov photons are emitted is called the Cherenkov angle (denoted θ_c) and is given by

$$\theta_c = \arccos\left(\frac{1}{\beta\, n}\right) , \tag{3.1}$$

as can be understood from Figure 3.2 [20, 28]. Cherenkov radiation is azimuthally symmetric around a charged particle's path. From every point along the path, the emitted photons form a Cherenkov cone with opening angle $2\,\theta_c$.

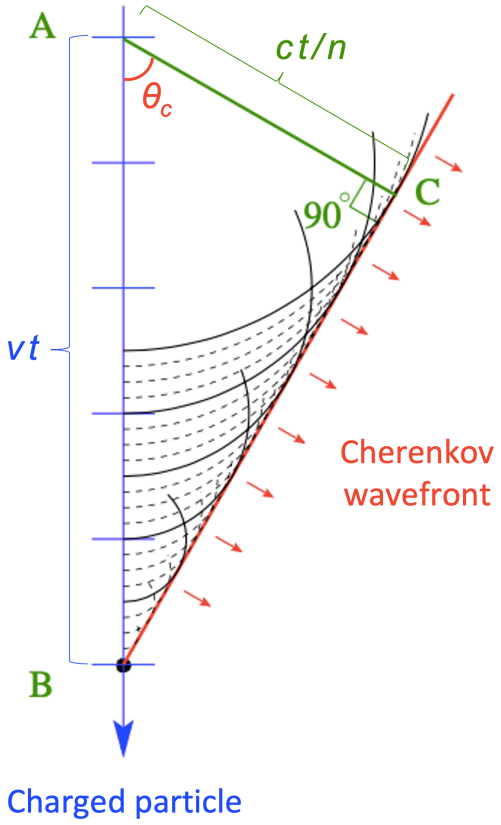

Figure 3.2: Cherenkov wavefront produced by the passage of a relativistic charged particle. In a time t, the particle travels a distance $v\,t$ from A to B while the EM pulse reaches a distance $c\,t\,/\,n$ from A. Photons emitted at the Cherenkov angle (θ_c) are coherent and make up the Cherenkov wavefront. Modified from [28].

The Cherenkov spectrum is described by the Frank–Tamm equation [20,31]:

$$\frac{dN}{dx\,d\lambda} = \frac{2\pi\,\alpha\,q^2}{e^2\,\lambda^2}\left(1 - \frac{1}{\beta^2\,n^2(\lambda)}\right) = \frac{2\pi\,\alpha\,q^2}{e^2\,\lambda^2}\,\sin^2(\theta_c(\lambda))\,, \tag{3.2}$$

where α is the fine structure constant, λ is the wavelength of the Cherenkov photon, q is the electric charge of the particle, and $e \approx 4.8 \times 10^{-10}$ statC is the elementary electric charge. It is important to note that the index of refraction is usually slightly dependent on wavelength and, consequently, the Cherenkov angle (equation (3.1)) is also a weak function of wavelength [32]. Equation (3.2) gives the number of Cherenkov photons emitted

per length dx travelled by the charged particle in a wavelength interval $d\lambda$. To obtain the total number of photons radiated along the particle's path, equation (3.2) must be integrated over the relevant length of the path and over all wavelengths for which $n(\lambda)$ meets the Cherenkov condition $\beta > 1/n$. The integral converges because this condition is not met at all wavelengths down to zero. An important takeaway from equation (3.2) is that Cherenkov emission is inherently independent of the particle's mass and depends on the particle's speed rather than its energy. As a result of this, among particles that are ultrarelativistic ($\beta \sim 1$), there is no appreciable difference in Cherenkov output or angle for any additional increase in energy, as these reach an asymptotic limit.

With the appropriate substitutions, equation (3.2) can reveal the energy provided by the particle to induce the Cherenkov effect. The energy per unit length travelled is

$$-\frac{dE}{dx} = \left(\frac{2\pi\, q}{c}\right)^2 \int_{\nu \,|\, \beta\, n(\nu) > 1} \nu\, \sin^2(\theta_c(\nu))\, d\nu\,, \tag{3.3}$$

where ν is the frequency of the Cherenkov photon. As particles must at least be relativistic to induce Cherenkov radiation, this energy loss is negligible for the particle.

3.2 Cherenkov radiation in the atmosphere

The index of refraction in air at sea level is approximately 1.00028 [32], with a weak dependence on wavelength—the index increases slightly for smaller and smaller wavelengths. In this medium, the minimum speed a charged particle must travel to be responsible for the emission of Cherenkov radiation is $\beta \sim 0.9997$; this corresponds to a Lorentz factor of $\gamma \sim 42$.

The Cauchy formula [33] is often used to describe the variation of n_{air} with wavelength:

$$n_{\text{air}}(\lambda) = 1 + \left(A + \frac{B}{\lambda^2} + \frac{C}{\lambda^4}\right)\,, \tag{3.4}$$

where $A = 2.73 \times 10^{-4}$, $B = 1.23 \times 10^{-14}$ cm^2, and $C = 3.56 \times 10^{-24}$ cm^4 are empirically determined [32].

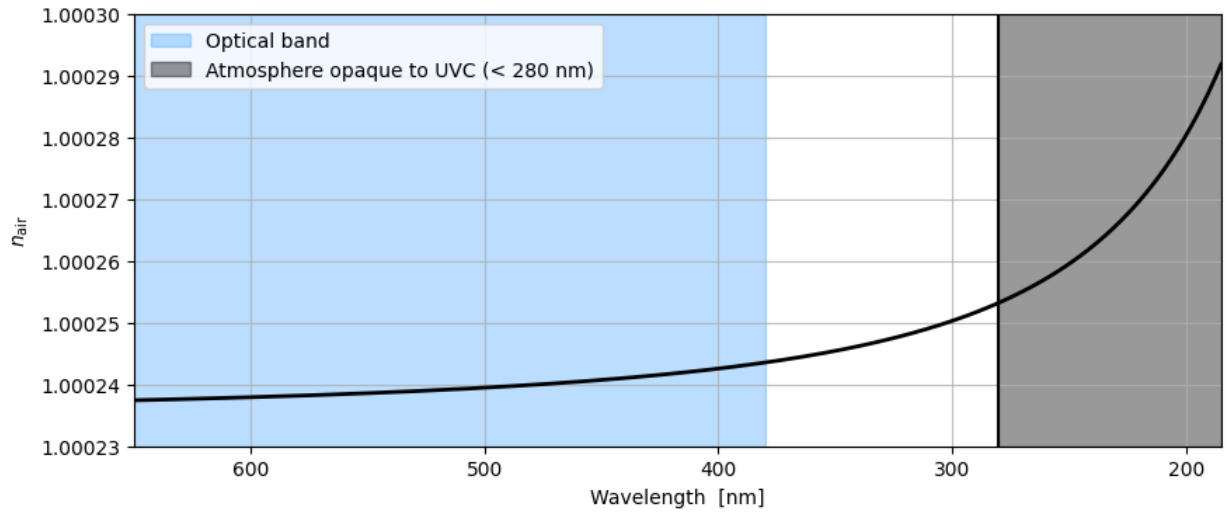

Figure 3.3: Refractive index of air as a function of wavelength at 1268 m above sea level (the altitude of the VERITAS observatory). The range plotted corresponds to the wavelengths to which the VERITAS photomultipliers are sensitive (nominally, 185 nm to 650 nm). The blue shaded region represents the optical band. The grey shaded region represents the UVC band (<280 nm), where the atmosphere is essentially opaque. The index is very weakly dependent on wavelength in the relevant (i.e., optical) range.

Altitude also modestly affects the index of refraction of air [32]. The altitude dependence of n_{air} is due to the change in air density. The pressure and temperature profiles of the atmosphere are the determinants for air density. Pressure variation with altitude follows an exponential relation, coming from hydrostatic equilibrium of Earth's atmosphere. The temperature profile is more complex as the direction of temperature change is different for each layer of the atmosphere [34]. Humidity in the troposphere is also an important factor affecting the temperature profile of this layer. Neglecting temperature, the variation of n_{air} with altitude h can be approximated by the exponential relation

$$n_{\text{air}}(\lambda,\, h) \;=\; 1 \;+\; (n_{\text{air},\,0}(\lambda) \;-\; 1)\; e^{-h\,/\,h_0}\,, \tag{3.5}$$

where $n_{\mathrm{air},\,0}(\lambda)$ is the index at sea level given by equation (3.4) and $h_0 = 8.4 \times 10^5$ cm is the scale height of the atmosphere [32]. As a result of this, the index of refraction is slowly increasing as a cosmic charged particle travels downwards through the atmosphere. The altitude at which the Cherenkov condition begins to be met therefore depends on the particle's speed and is slightly higher for the emission of shorter wavelengths.

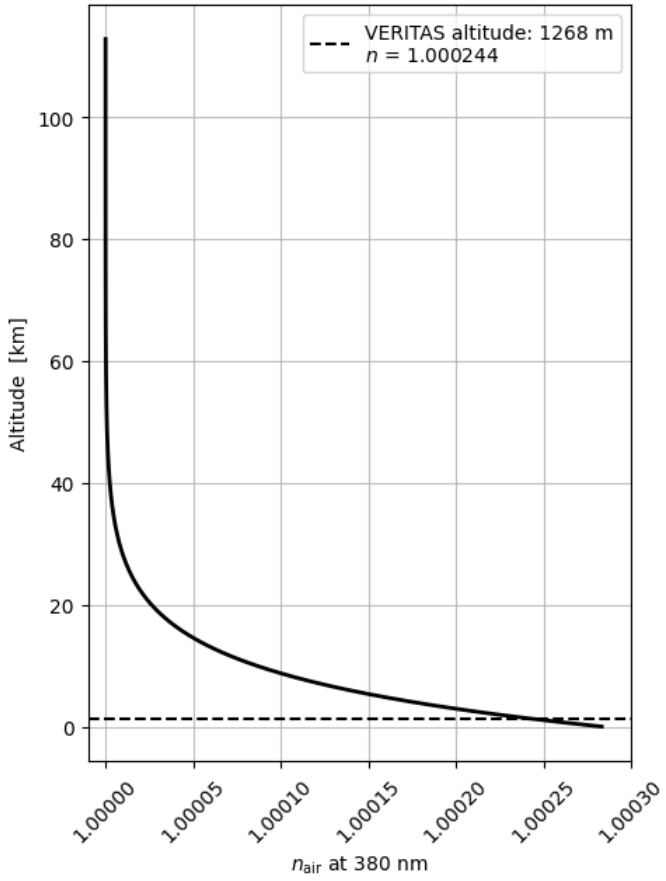

Figure 3.4: Refractive index of air as a function of altitude for 380-nm photons (around peak sensitivity of VERITAS photomultipliers). The dashed line indicates the altitude of the VERITAS observatory (1268 m), where $n_{\mathrm{air}}(\lambda = 380\,\mathrm{nm})$ is 1.000244. The index has an exponential relation with altitude as it closely follows air density and therefore atmospheric pressure.

Figure 3.3 shows the refractive index of air as a function of wavelength at the altitude of the VERITAS observatory (1268 m a.s.l.). Atmospheric absorption of the ultraviolet (UV) band C (100–280 nm) [34] greatly impedes the propagation of higher-energy Cherenkov photons. While equation (3.2) indicates higher-energy photons are radiated more abundantly, the relevant Cherenkov spectrum detectable in air peaks in the blue-UV band. Figure 3.4 shows the index as a function of altitude for 380-nm photons.

As can be understood from equation (3.1), the Cherenkov angle reaches an asymptotic limit as β approaches 1. This limit is 1.36° in air at sea level and 1.26° at 1268 m. Figure 3.5 shows how the Cherenkov angle evolves with a muon's energy. The high-energy muon is a good reference because it is relatively stable in its passage through the atmosphere.

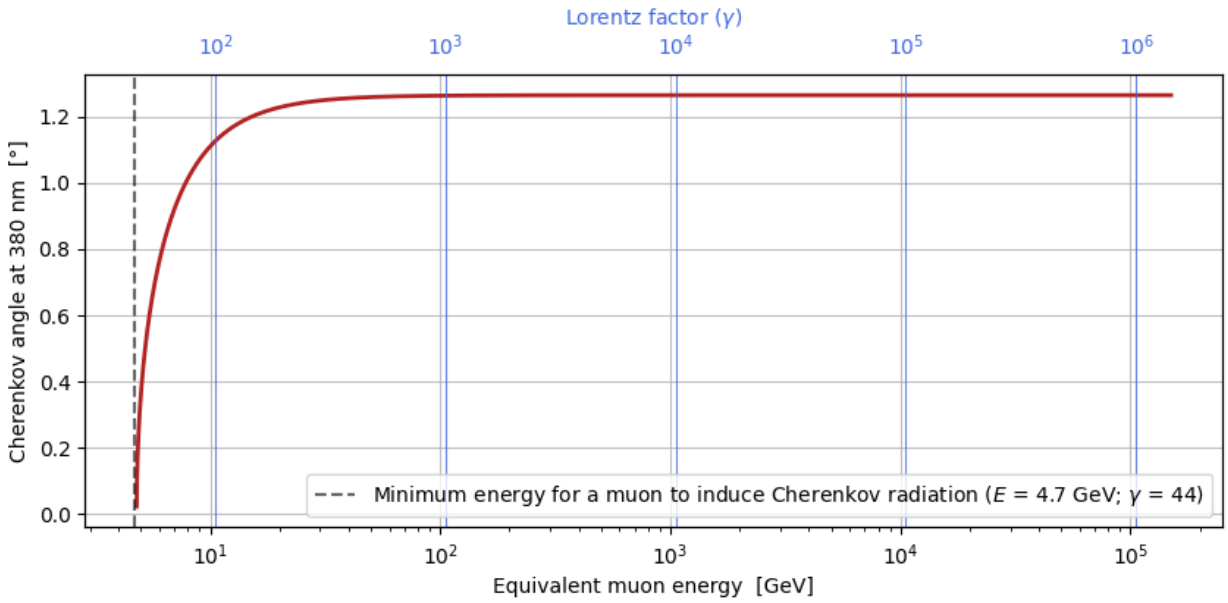

Figure 3.5: Cherenkov angle as a function of muon energy for 380-nm photons at 1268 m above sea level. Lorentz factor, which varies linearly with total energy, is indicated on the top ($\gamma = E/(m_\mu\, c^2)$ where $m_\mu\, c^2 \approx 0.106\,\mathrm{GeV}$ is the muon's rest energy [25]). The vertical dashed line indicates the minimum muon energy where Cherenkov photons with a minimum wavelength of 280 nm (UVB-UVC boundary) are produced. The high-energy muon is used as reference because it is relatively stable in its passage through the atmosphere.

3.3 Cherenkov radiation from a magnetic monopole

The relativistic passage of a magnetic charge through a dielectric medium is capable of inducing Cherenkov radiation through the same mechanism described in Section 3.1 [35]. The Cherenkov angle remains the same, so equation (3.1) and Figure 3.5 are applicable to MMs. The Frank–Tamm equation can be adapted to the case of a relativistic Dirac charge (g) by introducing a factor $(n\,g/e)^2$ to the $q = e$ case in equation (3.2) [2, 16]. Hence, the Cherenkov spectrum generated by a MM is

$$\frac{dN}{dx\,d\lambda} = \frac{\pi\,n^2(\lambda)}{2\,\alpha\,\lambda^2}\,\sin^2(\theta_c(\lambda))\,. \tag{3.6}$$

In air ($n \sim 1.00028$), this is roughly a 4700-fold uniform increase on the entire Cherenkov emission spectrum for a MM compared to a particle bearing an elementary electric charge at the same speed. Figure 3.6 shows the atmospheric Cherenkov spectrum of a MM with $\gamma \sim 10^4$ compared to that of a muon with the same speed.

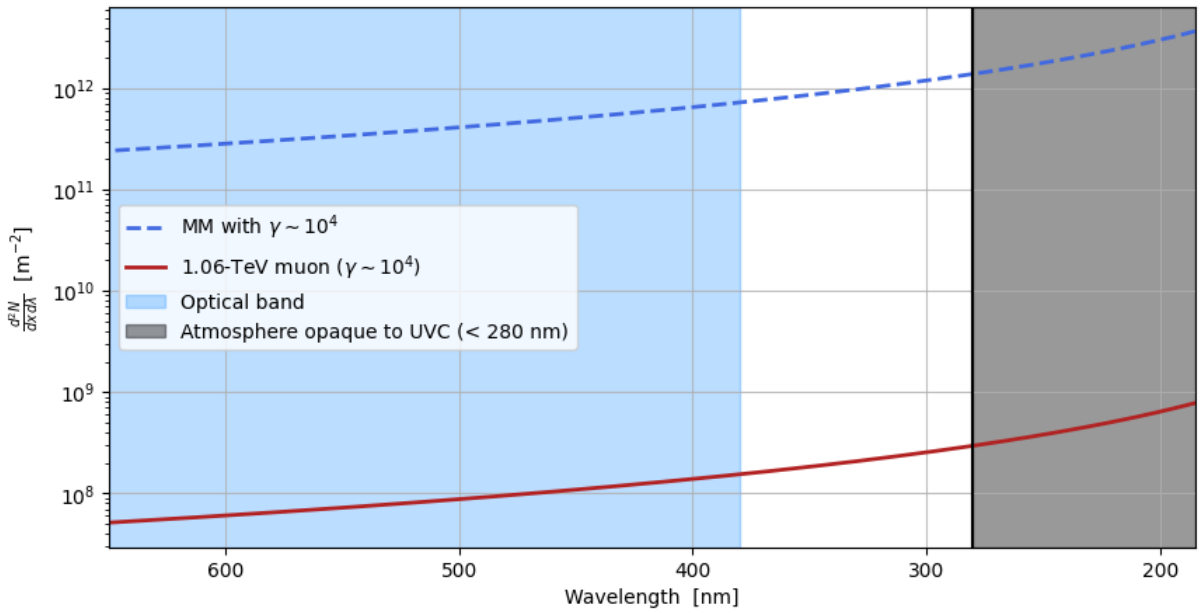

Figure 3.6: Atmospheric Cherenkov spectra of a magnetic monopole with $\gamma \sim 10^4$ (dashed blue curve) and of a muon with $\gamma \sim 10^4$ (solid red curve). The refractive index of air is evaluated for 1268 m above sea level (the altitude of the VERITAS observatory). The range plotted corresponds to the wavelengths to which the VERITAS photomultipliers are sensitive (nominally, 185 nm to 650 nm). The blue shaded region represents the optical band. The grey shaded region represents the UVC band (<280 nm), where the atmosphere is essentially opaque. The high-energy muon is used as reference because it is relatively stable in its passage through the atmosphere. A MM induces ∼4700 more atmospheric emission across the spectrum compared to a muon with the same speed.

Chapter 4

Past searches for GUT and intermediate-mass magnetic monopoles

4.1 Dedicated magnetic monopole experiments

In 1982, Blas Cabrera reported a signal consistent with a MM in his small-scale induction experiment at Stanford University, in California [36]. The event—nicknamed the "Valentine's Day monopole" for its occurrence on February 14th of that year—was a measured change in magnetic flux through a 5-cm-diameter superconducting loop wholly consistent with the passage of a Dirac charge. Cabrera remained prudent and never claimed a discovery as there was no way to rule out an instrument malfunction (Cabrera noted the possibility of a "spontaneous internal stress release mechanism" [36], although he deemed it improbable) or some accidental or malevolent human intervention (the lab was thought to be unoccupied at the time of the event but this could not be ascertained) [37]. The signal was not reproducible in later attempts by Cabrera [37].

In the years that followed the "Valentine's Day monopole," a number of large experiments were conceived with the goal of detecting cosmic MMs. Two important dedicated MM experiments were MACRO and SLIM. At the end of this chapter, Figure 4.1 shows the upper limits published by these MM experiments as well as upper limits established

by parasitic searches with experiments designed to study neutrinos, cosmic rays, and gamma rays. Table 4.1 presents a summary of the studies discussed in this chapter.

MACRO

MACRO (the Monopole, Astrophysics and Cosmic Ray Observatory) was a dedicated MM experiment which ran from 1989 to 2000 in Gran Sasso, Italy [38]. It incorporated many different search strategies, using scintillators, streamers, and a nuclear track-etch detector to measure the energy lost by MMs in matter. Together, these were sensitive to a wide range of monopole masses (10^6 GeV/c^2 and above) and velocities $4 \times 10^{-5} \leq \beta < 1$. After finding no detections in any of the sub-detectors, the combined velocity-dependent 90% confidence level (C.L.) upper limits were published, ranging from 1.3×10^{-16} to 3.1×10^{-16} cm^{-2} s^{-1} sr^{-1} [38]. MACRO also looked for evidence of Grand Unified Theory (GUT) MMs by searching for nucleon decay but found none [39].

SLIM

SLIM (the Search for Light Monopoles experiment) was an array of plastic nuclear track detectors designed to search for MMs at the Chacaltaya high-altitude laboratory in Bolivia from 2002 to 2006 [40]. During its run, it was sensitive to MMs with masses between 10^4 and 10^{18} GeV/c^2, but with a particular focus on intermediate-mass MMs (IMMs) with masses under 10^{13} GeV/c^2. SLIM did not restrict the search to MMs bearing only a single Dirac charge—as defined in equation (2.8)—; the possibility of $2g$ MMs, $>2g$ MMs, and dyons (particles having both magnetic and electric charge) was also studied. For the $1g$ case, two 90% C.L. upper limits were published: 1.3×10^{-15} cm^{-2} s^{-1} sr^{-1} for MM masses below 10^{13} GeV/c^2 (more stringent than MACRO) and 6.5×10^{-16} cm^{-2} s^{-1} sr^{-1} for masses above [40].

4.2 Neutrino experiments

Many experiments built to study neutrinos using water or ice Cherenkov detectors have also performed specific searches for MMs. Since neutrinos are neutral and so do not in-

duce Cherenkov radiation themselves, these experiments are designed to instead detect the radiation induced by the energetic charged particles coming out of the weak interactions between neutrinos and the nucleons in water molecules [41]. Neutrinos have an extremely small interaction cross section (on the order of 10^{-38} cm^2/GeV [42]), so these detectors must be very large to be effective. The index of refraction in water is $n \sim 1.33$ while it is $n \sim 1.31$ in ice [43], with some dependence on salinity and density. So following from equation (3.6), the Cherenkov radiation from a MM in water is as much as ∼8300 times more intense than that from a charged lepton at the same speed. This characteristic of MMs is what makes these Cherenkov experiments an interesting tool for their search. In general, the assumption must be made that cosmic monopoles can traverse the Earth at relativistic speeds—and so they are more likely to be in the mass range of IMMs rather than that of GUT MMs.

RICE

Embedded in the Antarctic ice of the geographic South Pole, RICE (the Radio Ice Cherenkov Experiment) was a neutrino detector that used 16 radio antennas sensitive to Cherenkov radiation in the 200–500 MHz band [17]. RICE was operational between 1999 and 2012. The MM search was sensitive to ultrarelativistic IMMs with $10^7 \leq \gamma \leq 10^{12}$ and masses between 10^4 and 10^9 GeV/c^2. In the dataset from 2001 to 2005, RICE established a speed-dependent 95% C.L. upper limit ranging from 9.5×10^{-19} to 2.2×10^{-18} cm^{-2} s^{-1} sr^{-1} [17].

BDUNT

BDUNT (the Baikal Deep Underwater Neutrino Telescope) was a water Cherenkov detector in the depths of Lake Baikal, in Siberia [44]. A MM search was conducted with data taken between 1998 and 2003, when BDUNT was under the "NT-200" configuration, consisting of eight strings fixed in the lake, each with 12 pairs of optical modules. The search was sensitive to MMs with mass $\geq 10^7$ GeV/c^2 and Lorentz factors between 1.67 and 10^3. The search produced 90% C.L. upper limits ranging from 4.6×10^{-17} to

1.83×10^{-16} cm^{-2} s^{-1} sr^{-1} depending on MM speed [44]. BDUNT was upgraded in 2015 to become the Baikal Gigaton Volume Detector (Baikal-GVD) [45].

AMANDA-II

AMANDA-II (the Antarctic Muon And Neutrino Detection Array) was a Cherenkov detector deployed at the South Pole, with 677 optical modules deep in the Antarctic ice [16]. A MM search was performed on data taken in the year 2000. The search considered monopole masses $\geq 10^5$ GeV/c^2 with $1.54 \leq \gamma \leq 10^{13}$. A distinction was made between downward-travelling and upward-travelling (through the Earth) MMs. Speed-dependent 90% C.L. upper limits ranged from 3.8×10^{-17} to 8.8×10^{-16} cm^{-2} s^{-1} sr^{-1} for the first category and 2.9×10^{-16} to 1.7×10^{-15} cm^{-2} s^{-1} sr^{-1} for the latter [16]. A search for monopole-induced nucleon decay was also performed but found no evidence of this. AMANDA-II is now integrated into the larger neutrino observatory, IceCube.

Super-Kamiokande

Located inside the Kamioka mine in Japan, Super-Kamiokande is a neutrino experiment consisting of a Cherenkov detector which contains 50,000 metric tons of pure water [46]. The approach taken with Super-Kamiokande was different than with other Cherenkov experiments: under the assumption that slow GUT MMs would be bound to the Sun and accumulate in its centre, Super-Kamiokande could detect the low-energy neutrinos produced following the monopole-induced decay of protons (p)

$$p \longrightarrow \text{mesons} + e^+ \text{ or } \mu^+ ,$$

where e^+ represents a positron and μ^+ a positively-charged muon [46]. The neutrinos in question would arise as decay products of mesons and of muons (these two decays are discussed in some more detail later in Section 5.2.2). The monopole search thus focused on GUT MM masses (10^{16}–10^{17} GeV/c^2) and speeds $10^{-5} \leq \beta \leq 5 \times 10^{-2}$. Finding no evidence of proton decay catalyzed by GUT MMs, very constraining speed-dependent 90%

C.L. upper limits were established, ranging from 6.3×10^{-28} to 8.8×10^{-24} cm^{-2} s^{-1} sr^{-1} [46].

IceCube

Successor to AMANDA-II, IceCube is a neutrino telescope inside a cubic kilometre of Antarctic ice at the geographic South Pole [41]. IceCube uses 5160 digital optical modules deployed across 86 vertical strings for the detection of Cherenkov light. The IceCube collaboration has already published a few results from MM searches. One such search [47] for monopoles with speeds $\beta \geq 0.51$ was performed on one year of data between 2011 and 2012, while assuming a general monopole mass around 10^{11} GeV/c^2. For the detection of MMs below the Cherenkov threshold in ice ($\beta < 0.76$), IceCube relied on the possibility for monopoles to knock off δ-electrons to above Cherenkov threshold. Following this search, a 90% C.L. upper limit of 1.55×10^{-18} cm^{-2} s^{-1} sr^{-1} was published in 2016 [47]. Another MM search [35] in eight years of IceCube data from 2011 to 2018 was sensitive to monopole masses between 10^8 and 10^{10} GeV/c^2 and speeds $0.75 \leq \beta \leq 0.995$. The IceCube collaboration published an overall 90% C.L. upper limit of 2.0×10^{-19} cm^{-2} s^{-1} sr^{-1} for this speed interval in 2022 [35]. Contrary to the search with AMANDA-II, the IceCube studies only considered upward-travelling events, owing to the fact that downward signals are overwhelmed by a background of atmospheric muons.

ANTARES

ANTARES (the Astronomy with a Neutrino Telescope and Abyss environmental RESearch project) was a Cherenkov experiment in the waters of the Mediterranean Sea, south of Toulon, France [48]. ANTARES used 12 vertical detection lines each composed of 75 optical modules. A search for monopoles with masses between 10^{10} and 10^{14} GeV/c^2 and speeds $0.55 \leq \beta \leq 0.995$ was performed with data taken between 2008 and 2022. Like with IceCube, ANTARES relied on signals from δ-electrons for the detection of MMs below the Cherenkov threshold in seawater ($\beta < 0.75$). Finding no evidence of MMs, 90% C.L. upper limits were calculated between 5.9×10^{-19} and 8.0×10^{-18} cm^{-2} s^{-1} sr^{-1}

depending on monopole speed [48]. As of this writing, these limits are in pre-publication. ANTARES is currently being replaced by KM3NeT (the Cubic Kilometre Neutrino Telescope).

4.3 Other experiments

Two other experiments are notable for their work on MMs: the Pierre Auger Observatory and H.E.S.S.

Pierre Auger Observatory

The Pierre Auger Observatory is an ultra-high-energy cosmic-ray experiment located in western Argentina [22]. It makes use of two detectors with an effective area of 3000 km^2: the Surface Detector, composed of 1660 water Cherenkov tanks, and the Fluorescence Detector, consisting of 24 telescopes in total [49]. The Surface Detector measures the water Cherenkov radiation coming from secondary particles as they travel through the tanks and can operate day and night. These secondaries are created in the hadronic showers initiated by cosmic rays in the atmosphere (cosmic rays and hadronic showers are discussed in more detail in Section 5.2.2). The Fluorescence Detector measures the ultraviolet (UV) light emitted by the nitrogen molecules that are excited by these same secondary particles and can only operate during clear, moonless nights. For the purpose of a MM search, the Pierre Auger collaboration studied only events that were detected by both detectors. The search focused on ultrarelativistic IMMs with a total energy equalling 10^{16} GeV, meaning that the searched monopole mass was constrained to vary inversely with γ. The search was sensitive to IMMs with $10^8 \leq \gamma \leq 10^{13}$. Speed-dependent 90% C.L. upper limits were found to range from 2.51×10^{-21} to 8.43×10^{-18} cm^{-2} s^{-1} sr^{-1} [22].

H.E.S.S.

H.E.S.S. (the High Energy Stereoscopic System) is a very-high-energy (VHE) gamma-ray experiment using five imaging atmospheric Cherenkov telescopes (IACTs) in the

Khomas highlands of Namibia [50]. The VHE band is generally defined as photons with energies ranging from 100 GeV to 100 TeV. How IACTs operate is discussed in more detail in Chapter 5, which presents the VERITAS telescope. The ability of IACTs to detect ultrarelativistic MMs is also explored in that chapter. In 2009, Gerrit Spengler [51] used simulations to determine the kind of images an ultrarelativistic MM would create in H.E.S.S. In his thesis, he asserted that MMs would produce a pair of bright clusters in the instrument's camera plane and searched for their signature through 2400 hours of data taken between 2004 and 2009. At the time of that analysis, H.E.S.S. only had four telescopes—the fifth telescope (larger than the other four) was only added in 2012 [50]. Spengler's work was never published in a scientific journal, but he established a 90% C.L. upper limit of 4.5×10^{-14} cm^{-2} s^{-1} sr^{-1} for MMs with mass $\geq 10^3$ GeV/c^2 and $\gamma \sim 10^5$ [51, 52]. The limit is very poorly constraining (even less so than the Parker bound), but Spengler showed the potential for IACTs to search for MMs in a novel way, independently from the methods used by dedicated MM experiments and by neutrino experiments. Additionally, the search with H.E.S.S. for ultrarelativistic MMs with a Lorentz factor of 10^5 is a parameter space not nominally explored by the Pierre Auger Observatory or RICE, which also considered only very high Lorentz factors. Spengler's thesis served as inspiration for this work with VERITAS.

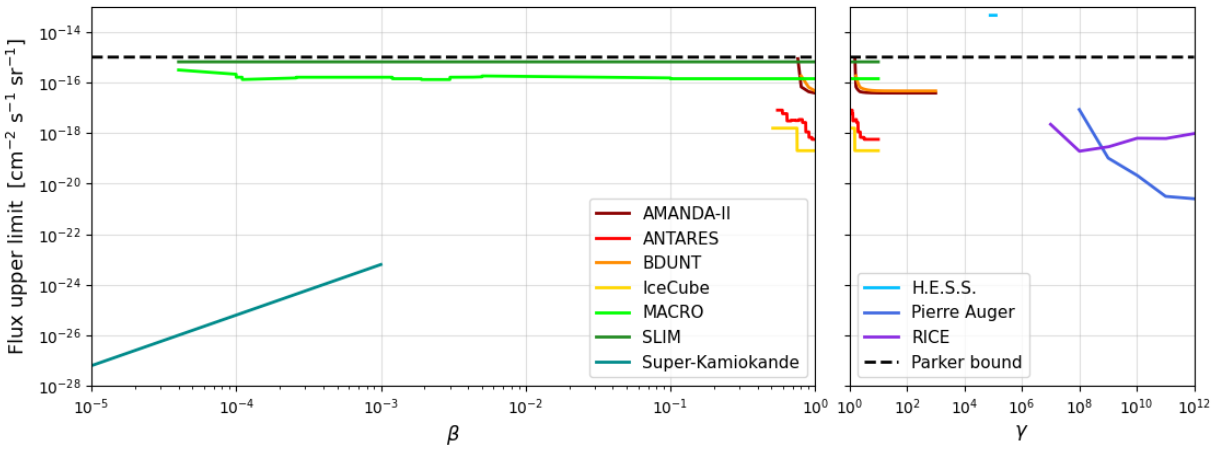

Figure 4.1: Flux upper limits for GUT and intermediate-mass magnetic monopoles with respect to monopole relative speed (β) and Lorentz factor (γ). Different coloured curves represent the results from different searches. All upper limits are 90% confidence level except for RICE's, which are 95%. For searches with multiple overlapping limits (e.g., AMANDA-II's direction-dependent limits, SLIM's mass-dependent limits), only the most stringent limit is shown. These limits do not all apply to the same monopole mass range. The Parker bound (dashed black line) is set at 10^{-15} cm^{-2} s^{-1} sr^{-1}. Note that these curves are approximations; for more detailed graphical representations, the reader is referred to the individual publications cited.

Table 4.1: Notable searches for GUT and intermediate-mass magnetic monopoles. All flux upper limits are 90% confidence level except for RICE's, which are 95%.

Experiment	Experiment type	Livetime (days)	Exposure (cm^2 sr s)	MM mass range ($\log[\mathrm{GeV}/c^2]$)	MM velocity range	Flux upper limits (cm^{-2} s^{-1} sr^{-1})
AMANDA-II [16]	Ice Cherenkov neutrino telescope	155		5–18	$\beta = 0.76$ (up)	$\leq 8.8 \times 10^{-16}$
					$\beta = 0.8$ (up)	$\leq 6.7 \times 10^{-17}$
					$\beta = 0.8$ (down)	$\leq 1.7 \times 10^{-15}$
					$\beta = 0.9$ (up)	$\leq 4.3 \times 10^{-17}$
					$\beta = 0.9$ (down)	$\leq 4.2 \times 10^{-16}$
					$\beta \sim 1$ (up); $\gamma \leq 10^3$	$\leq 3.8 \times 10^{-17}$
					$\beta \sim 1$ (down); $\gamma \leq 10^3$	$\leq 2.9 \times 10^{-16}$
ANTARES [48]	Undersea Cherenkov neutrino telescope	3286		10–14	$0.5500 \leq \beta < 0.5945$	$\leq 8.0 \times 10^{-18}$
					$0.5945 \leq \beta < 0.6390$	$\leq 5.8 \times 10^{-18}$
					$0.6390 \leq \beta < 0.6835$	$\leq 3.0 \times 10^{-18}$
					$0.6835 \leq \beta < 0.7280$	$\leq 3.2 \times 10^{-18}$
					$0.7280 \leq \beta < 0.7725$	$\leq 3.1 \times 10^{-18}$
					$0.7725 \leq \beta < 0.8170$	$\leq 3.4 \times 10^{-18}$
					$0.8170 \leq \beta < 0.8615$	$\leq 2.6 \times 10^{-18}$
					$0.8615 \leq \beta < 0.9060$	$\leq 1.1 \times 10^{-18}$
					$0.9060 \leq \beta < 0.9505$	$\leq 6.7 \times 10^{-19}$
					$0.9505 \leq \beta \leq 0.9950$	$\leq 5.6 \times 10^{-19}$
BDUNT [44]	Underwater Cherenkov neutrino telescope	1003		$\geq$7	$\beta = 0.8$	$\leq 1.83 \times 10^{-16}$
					$\beta = 0.9$	$\leq 6.5 \times 10^{-17}$
					$\beta \sim 1$; $\gamma \leq 10^3$	$\leq 4.6 \times 10^{-17}$
H.E.S.S. [51]	IACT array	100		$\geq$3	$\gamma = 10^5$	$\leq 4.5 \times 10^{-14}$
IceCube [35,47]	Ice Cherenkov neutrino telescope	311		$\sim$11	$0.510 \leq \beta \leq 0.870$	$\leq 1.55 \times 10^{-18}$
		2886		$\geq$8–10	$0.750 \leq \beta \leq 0.995$	$\leq 2.0 \times 10^{-19}$
MACRO [38]	Dedicated MM detector experiment (scintillators, streamers, nuclear track detectors)	3470		$\geq$6	$4.0 \times 10^{-5} \leq \beta < 1.0 \times 10^{-4}$	$\leq 2.1 \times 10^{-16}$–3.1×10^{-16}
					$1.0 \times 10^{-4} \leq \beta < 1.1 \times 10^{-4}$	$\leq 1.6 \times 10^{-16}$
					$1.1 \times 10^{-4} \leq \beta < 2.6 \times 10^{-4}$	$\leq 1.3 \times 10^{-16}$–1.5×10^{-16}
					$2.6 \times 10^{-4} \leq \beta < 1.2 \times 10^{-3}$	$\leq 1.6 \times 10^{-16}$
					$1.2 \times 10^{-3} \leq \beta < 1.9 \times 10^{-3}$	$\leq 1.4 \times 10^{-16}$
					$1.9 \times 10^{-3} \leq \beta < 3.0 \times 10^{-3}$	$\leq 1.3 \times 10^{-16}$
					$3.0 \times 10^{-3} \leq \beta < 4.1 \times 10^{-3}$	$\leq 1.6 \times 10^{-16}$
					$4.1 \times 10^{-3} \leq \beta < 5.0 \times 10^{-3}$	$\leq 1.6 \times 10^{-16}$–1.66×10^{-16}
					$5.0 \times 10^{-3} \leq \beta < 0.1$	$\leq 1.5 \times 10^{-16}$–1.8×10^{-16}
					$0.1 \leq \beta < 1$	$\leq 1.4 \times 10^{-16}$
Pierre Auger [22]	Ultra-high-energy cosmic-ray detector (water Cherenkov tanks, UV fluorescence telescopes)		3.66×10^{17}	3–8	$\gamma = 10^8$	$\leq 8.43 \times 10^{-18}$
			3.00×10^{19}		$\gamma = 10^9$	$\leq 1.03 \times 10^{-19}$
			1.42×10^{20}		$\gamma = 10^{10}$	$\leq 2.18 \times 10^{-20}$
			9.94×10^{20}		$\gamma = 10^{11}$	$\leq 3.12 \times 10^{-21}$
			1.23×10^{21}		$\gamma \geq 10^{12}$	$\leq 2.51 \times 10^{-21}$

Table 4.1 continued

Experiment	Experiment type	Livetime (days)	Exposure (cm^2 sr s)	MM mass range ($\log[\mathrm{GeV}/c^2]$)	MM velocity range	Flux upper limits (cm^{-2} s^{-1} sr^{-1})
RICE [17]	Ice Cherenkov neutrino telescope	675		4–9	$\gamma = 10^7$	$\leq 2.2 \times 10^{-18}$
					$\gamma = 10^8$	$\leq 1.9 \times 10^{-19}$
					$\gamma = 10^9$	$\leq 2.8 \times 10^{-19}$
					$\gamma = 10^{10}$	$\leq 6.2 \times 10^{-19}$
					$\gamma = 10^{11}$	$\leq 6.0 \times 10^{-19}$
					$\gamma \geq 10^{12}$	$\leq 9.5 \times 10^{-19}$
SLIM [40]	Dedicated MM detector experiment (array of plastic nuclear track detectors)	1540		4–13	$4 \times 10^{-5} \leq \beta < 1$ (depending on magnetic & electric charges)	$\leq 1.3 \times 10^{-15}$
				13–18		$\leq 6.5 \times 10^{-16}$
Super-Kamiokande [46]	Water Cherenkov neutrino detector	2853		16–17	$\beta = 10^{-5}$	$\leq 6.3 \times 10^{-28}$
					$\beta = 10^{-4}$	$\leq 6.3 \times 10^{-26}$
					$\beta = 10^{-3}$	$\leq 6.3 \times 10^{-24}$

Chapter 5

VERITAS

5.1 Introduction to VERITAS

The Very Energetic Radiation Imaging Telescope Array System (VERITAS) is a ground-based stereoscopic array of four imaging atmospheric Cherenkov telescopes (IACTs) designed to study the gamma-ray universe, located south of Tucson, Arizona, at the base of Mount Hopkins ($+31^\circ\ 40'\ 30.21''$, $-110^\circ\ 57'\ 7.77''$, altitude 1268 m a.s.l.) [53]. It is on the site of the Fred Lawrence Whipple Observatory and part of the Smithsonian Astrophysical Observatory.

VERITAS does not observe gamma-ray photons directly. Instead, it measures the short flashes of Cherenkov light produced in the extensive air showers (EASs) that gamma rays initiate in the atmosphere [28, 54]. VERITAS is also sensitive to EASs initiated by cosmic rays, which are overwhelmingly more abundant. Section 5.2 discusses EASs in more detail. An important part of data reduction with VERITAS is to use the properties of EASs to distinguish the gamma-ray events from the cosmic-ray events.

Each of the four telescopes follows a Davies–Cotton design and is a 12-m dish composed of 345 hexagonal mirrors that reflect light into a central camera. Figure 5.1 is a photograph of one of the four telescopes. Each telescope's camera (see Figure 5.2) is an array of 499 Hamamatsu R10560-100-20 photomultiplier tubes (PMTs) arranged in a hexago-

nal pattern [55]. These PMTs are sensitive to wavelengths between 185 and 650 nm [56]. Each telescope is steerable on an altitude-azimuth mount. The distance between any two telescopes ranges between 81.5 m and 172.5 m. The telescopes' positions on the site are plotted in Figure 5.3.

Figure 5.1: Photograph of one of the VERITAS telescopes (T4) stowed on its platform. Photo by the author.

VERITAS is a pointing instrument with a 3.5° field of view (FOV). The instrument's energy range for gamma rays is from 85 GeV to >30 TeV with an energy resolution of 17% and an angular resolution of 0.08° at 1 TeV [53]. PMTs offer an excellent time resolution, needed to identify the short flashes of Cherenkov light. As a performance metric, VERITAS can make a statistically significant detection of a gamma-ray source with 1% the flux of the Crab Nebula in 25 hours of observation [53].

VERITAS saw first light as a four-telescope array in 2007 and then was upgraded in 2009, at which time telescope T1 was repositioned further to improve the stereoscopy of

the array [53]. Another upgrade in 2012 involved replacing the PMTs and improving the electronics, which resulted in an increase in photon collection efficiency by 50% [57]. Its location in the Sonoran desert is advantageous because the area is dry and receives little cloud coverage and rain throughout most of the year. The surrounding mountains act as shields from the light pollution coming from nearby cities Tucson and Nogales. VERITAS halts operations during the summer season (July and August) due to monsoons [53].

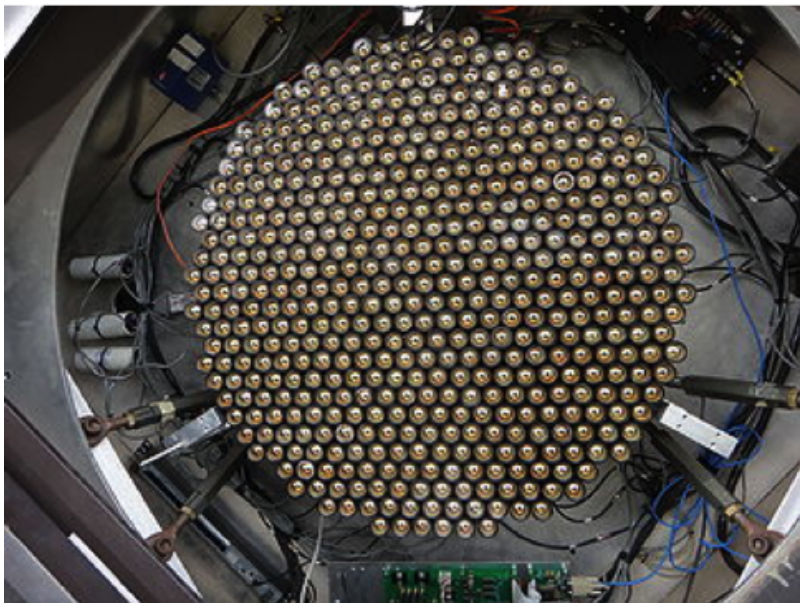

Figure 5.2: Photograph of the 499 photomultiplier tubes that form a VERITAS camera. Taken from [57].

Gamma-ray observations are performed only at night under dark conditions. Dark runs last about three weeks and are bookended by periods of 8 or 9 days where the moon is over 90% full. VERITAS can be operated at reduced high voltage (RHV) when the moon is 30 to 65% illuminated in the sky to avoid wearing out the PMTs and overwhelming the electronics. RHV observations are reserved for sources that are known to be very-high-energy (VHE) gamma-ray-bright and to monitor for possible blazar flares. Over 10 months each year, VERITAS typically observes 750 hours of dark time and 200 hours of moonlight time [53].

Gamma-ray sources observed by VERITAS include a variety of active galactic nuclei (especially blazars) and galactic sources such as supernova remnants, pulsar wind nebulae, pulsars, microquasars, and X-ray binaries [28]. Dark-matter-rich dwarf spheroidal galaxies are not known to contain notable astrophysical sources of gamma rays but can be good targets for the search of gamma rays generated by possible dark matter interactions [58].

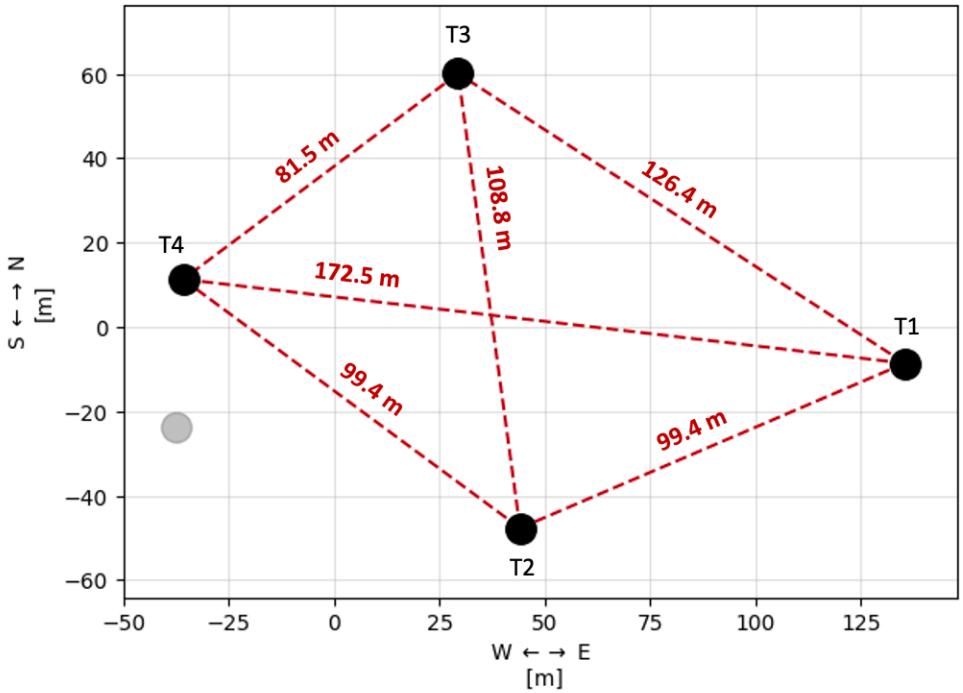

Figure 5.3: Positions of VERITAS telescopes T1 through T4 at the Fred Lawrence Whipple Observatory. The gray circle represents T1's position prior to 2009. The origin of the plot is the centre of the original array (before 2009).

5.2 Extensive air showers

There are two main types of EASs: electromagnetic (EM) showers and hadronic showers.

5.2.1 Electromagnetic showers

Earth's atmosphere is not transparent to gamma rays. When a highly energetic photon ($h\nu \gg 1$ MeV) passes through a medium—like air—, it is predominantly subject to pair production [20]. The average length a photon can travel in a medium without pair-producing depends on the composition of the medium as well as its density. This length is very large in the interstellar and intergalactic media; so gamma rays can travel from many distant sources to Earth with little hindrance. In Earth's atmosphere, the gamma-ray photon is quickly converted into a particle-antiparticle pair. Overwhelmingly, this means the creation of an electron (e^-) and a positron (e^+) (the lightest charged fermions), which share the energy of the initial photon (γ):

$$\gamma \longrightarrow e^- + e^+ .$$

Pair production by a single photon in a vacuum is forbidden because the resulting daughter particles could not simultaneously conserve the energy and momentum of the photon. In a medium, the surrounding molecules can receive the change in momentum brought on by this process.

The daughter particles of pair production are still highly energetic. Beyond a critical energy of $\sim$88 MeV*, electrons (and positrons) travelling through the atmosphere will lose energy predominantly through bremsstrahlung [20]. This process is driven by the deviation of the electron by a close encounter with a nucleus of the medium. The electron's total energy is split between itself and the photon it emits:

$$e^- \longrightarrow e^- + \gamma$$
$$e^+ \longrightarrow e^+ + \gamma .$$

The average length an electron travels in a medium before this process occurs is called the radiation length. In dry air, the radiation length is 36.62 g/cm^2 [23] (to get a proper

*88 MeV is the critical energy for electrons in dry air at 1 atm [23].

length, one must divide this number by density). The average length a photon travels before pair production is comparable to this value: it is roughly 9/7 times the radiation length [28].

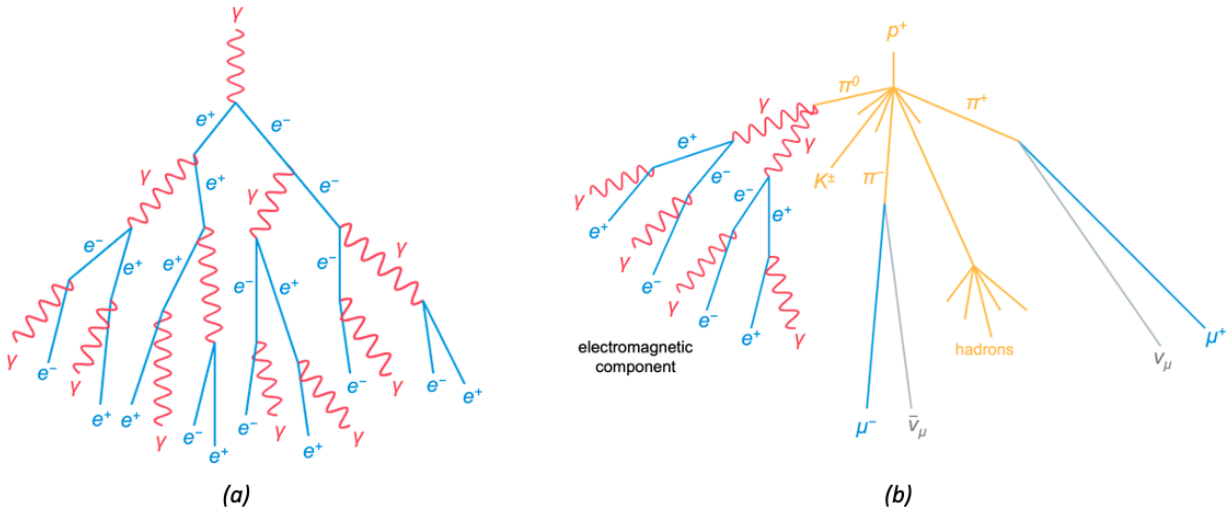

Figure 5.4: Extensive air shower diagrams. (a) An electromagnetic shower initiated by a primary gamma ray. As long as it is energetic enough, each photon (γ) in the cascade produces an electron (e^-)-positron (e^+) pair and each electron and positron emits a photon by bremsstrahlung. Shower maximum is reached at the step where daughter particles begin to fall below critical and the shower propagation dies down. (b) A hadronic shower initiated by a proton. The primary proton (p^+) collides with an atmospheric nucleus and produces many hadrons, including nucleons and mesons (notably pions ($\pi^\pm$, π^0) as well as kaons ($K^\pm$, K^0, $\overline{K}^0$)). Charged pions decay into a muon ($\mu^\pm$) and neutrino (ν_μ, $\overline{\nu}_\mu$). Neutral pions quickly decay into a pair of gamma rays, which then produce secondary EM showers. Other hadronic species, such as an α particle or a heavy nucleus, can serve as the primary particle in a hadronic shower. Overall, hadronic showers are much more complex and have greater lateral spread compared to EM showers.

Hence, in the atmosphere, a highly energetic primary gamma ray, electron, or positron will initiate a cascade of particles which successively undergo pair production and bremsstrahlung until the daughter particles pass under the energy threshold required to main-

tain the two processes. At this point, shower maximum is reached and the shower propagation begins to die down [28]. The cascades initiated by these three particle types are called EM showers and they are somewhat predictable and "clean" in their pattern. It is very difficult to distinguish an EM shower initiated by a photon from one initiated by an electron or positron. However, highly energetic electrons and positrons of cosmic origin are rare: these charged particles have highly deflected paths between their source and the Earth due to galactic magnetic fields, and so their energy is easily depleted due to synchrotron radiation before their arrival. Gamma rays are therefore the main initiators of (purely) EM showers that we observe in the atmosphere [28]. Figure 5.4(a) depicts a cartoon of an EM shower initiated by a gamma ray.

5.2.2 Hadronic showers

Cosmic rays are high-energy massive particles that propagate through the Universe and arrive nearly isotropically on Earth. These are predominantly protons, but α particles (helium nuclei) and heavier nuclei are also common. The flux of cosmic rays on Earth is many orders of magnitude greater than that of gamma rays [28].

When a cosmic ray enters the atmosphere, it collides with atoms in the atmosphere to create particles born from strong interactions, which themselves go on colliding and producing more particles, generating a hadronic shower. Because of the heavier components produced in hadronic showers, conservation of momentum requires that they grow more broadly than EM showers. Pions make up a large component of hadronic showers, stealing energy away from whatever baryons remain after collisions [28]. Any baryons produced that are more massive than nucleons—for example Δ resonances—are unstable and their decay often includes pions in their final state. Pions have short lifetimes and their decay channels are different depending on whether they are charged or neutral. The lifetime of a neutral pion (π^0) is 8.4×10^{-17} s [25] and its main decay channel is electromagnetically into two gamma-ray photons (γ):

$$\pi^0 \longrightarrow \gamma + \gamma \,.$$

These gamma rays go on to produce their own EM showers in the atmosphere [54]. Charged pions ($\pi^{\pm}$) cannot decay electromagnetically and so must decay via the weak interaction, providing them with a considerably longer lifetime of 2.6×10^{-8} s [25]. The main decay channel for a charged pion is into a muon ($\mu^{\pm}$) and muon neutrino pair (ν_{μ} or $\overline{\nu}_{\mu}$):

$$\pi^{+} \longrightarrow \mu^{+} + \nu_{\mu}$$
$$\pi^{-} \longrightarrow \mu^{-} + \overline{\nu}_{\mu}\,.$$

Figure 5.4(b) depicts a cartoon of a hadronic shower initiated by a proton.

Muons

Muons are products of hadronic showers but can also occasionally come from neutrino charged-current interactions in the atmosphere. Muons are about 200 times more massive than electrons, so their energy loss via bremsstrahlung is $\sim 4 \times 10^{4}$ times less efficient than that of electrons [21]. Thus, once produced in an EAS, they will lose little energy via this process and will likely propagate to ground level without extending the shower any further (unless they decay).

Muons decay into an electron (e^{-}), an electron antineutrino ($\overline{\nu}_{e}$), and a muon neutrino (ν_{μ})—or the antimatter partners of these (e^{+}, ν_{e}, and $\overline{\nu}_{\mu}$ respectively):

$$\mu^{-} \rightarrow e^{-} + \overline{\nu}_{e} + \nu_{\mu}$$
$$\mu^{+} \rightarrow e^{+} + \nu_{e} + \overline{\nu}_{\mu}\,.$$

If the created electron or positron is energetic enough, it will then initiate its own EM shower. Muons have a (proper) lifetime of 2.20 μs [25]. However, due to time dilation, the highly energetic muons created in a shower at an altitude on the order of 10 km can easily reach Earth's surface before decaying. Figure 5.5 shows the probability for a muon to survive a travel distance for different muon energies.

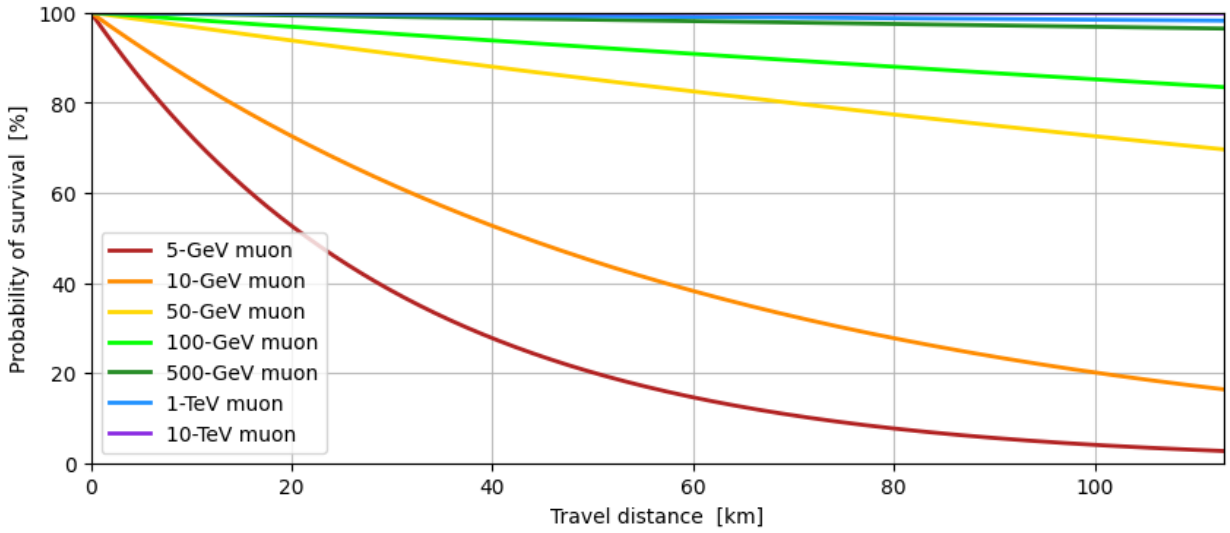

Figure 5.5: Probability of survival for a muon as a function of distance travelled. This only considers muon decay, not inelastic collisions that may be destructive to the muon. Different coloured curves represent different energies. Time dilation is responsible for prolonging the muon's survival for higher and higher energies. As its Lorentz factor increases with energy, the lifetime of the muon (a proper time) is observed to be dilated in the Earth frame. Muons are predominantly produced in hadronic showers at tens of kilometres above Earth's surface.

Neutrinos

The many neutrinos created in a hadronic shower rarely interact with matter [42]. Being neutral, neutrinos are incapable of inducing Cherenkov radiation on their own. Neutrinos (of cosmic or atmospheric origin) are ignored in the context of this work.

5.3 The VERITAS trigger system

Optical light from stars and stray light from local origins and from the night sky background (NSB) are picked up by VERITAS's PMTs. These are noise in the context of gamma-ray observations. VERITAS thus employs a three-level trigger system [59] to conserve only the information from an EAS (an "event"). The trigger system relies on

VERITAS's stereoscopic ability; an atmospheric event is expected to be seen by more than one telescope.

Level 1 trigger

The level 1 (L1) trigger happens at the PMT level. Because of backgrounds, PMTs sit at a "pedestal" voltage of around -20 mV. When enough photons are detected by a PMT such that the voltage passes a threshold, that PMT will trigger and pass on the information to the next level. L1 uses a constant fraction discriminator (CFD), which evaluates the pulse from a PMT to trigger at the same point in time with respect to the pulse shape, regardless of its amplitude [60]. Under normal VERITAS operations, the CFD threshold is set at -60 mV. During observations, across all PMTs in the array, L1 is passed at a rate of $\sim$400 MHz [61].

Level 2 trigger

The level 2 (L2) trigger happens at the telescope level. If three or more contiguous PMTs in a camera all pass L1 within $\sim$6 ns, then L2 is passed for this telescope. This occurs at a rate of $\sim$5 kHz [61]. Not all patterns are acceptable for the purpose of L2: notably, three triggered pixels in a straight line are not enough to pass.

Level 3 trigger

The level 3 (L3) trigger happens at the array level. If two or more telescopes pass L2 within a coincidence window of 50 ns, then L3 is passed and the event is saved. Typical L3 rates are about 300–400 Hz [61]. The threshold for L3 is sometimes increased to three telescopes during observation runs with a lot of backgrounds (e.g., targets near the Galactic Centre).

VERITAS's trigger system is effective at removing NSB and local noise as well as most muon events (see Section 5.6). The large majority of events that pass L3 are hadronic showers (1000 times more abundant than gamma ray events) [28]. Analysis of shower

images is what then allows for the discrimination between gamma rays and cosmic rays—referred to as gamma-hadron separation.

5.4 Image analysis

Both kinds of EASs (and particularly EM showers) appear roughly as ellipses in the camera plane. The charged particles produced in an EAS are responsible for inducing the atmospheric Cherenkov radiation detected by IACTs. This radiation roughly forms a conical light pool, typically with an apex near shower maximum at $\sim$10 km above ground level and a base of radius $\sim$130 m [54]. Telescopes that are caught in this light pool and pointing in the direction of the incoming primary particle are able to detect the shower. The images formed in different telescopes are not identical; instead, the orientation of the images in the camera plane reveal the arrival direction of the primary particle (see Figure 5.6). Extending the major axes of the ellipse-like shapes allows for the reconstruction of the source location where they intersect [54]. This is the advantage of having multiple IACTs in an array.

More energetic primary particles lead to the production of more Cherenkov radiation. In a sense, VERITAS uses the atmosphere as a calorimeter [28]: more energetic primaries produce larger signals. This energy-to-output relationship for the primary is unlike the relationship described by equation (3.2), which characterizes the speed-dependent Cherenkov output for a single charged particle. This is because higher-energy primaries create a larger number of charged secondaries—that will each generate Cherenkov photons according to (3.2) for as long as they exist and meet the Cherenkov condition—before these secondaries reach critical energy and the shower stops propagating. The size and intensity of the images in the camera plane thus allow for the reconstruction of the energy of the primary.

VERITAS and other IACTs are limited to detecting EM showers initiated by gamma rays in the VHE band (between 100 GeV and 100 TeV). This is because photons less ener-

getic than VHE produce showers that are too small to reliably detect while photons more energetic than VHE are too infrequent and would require an array that covers a larger area to make significant detections [28].

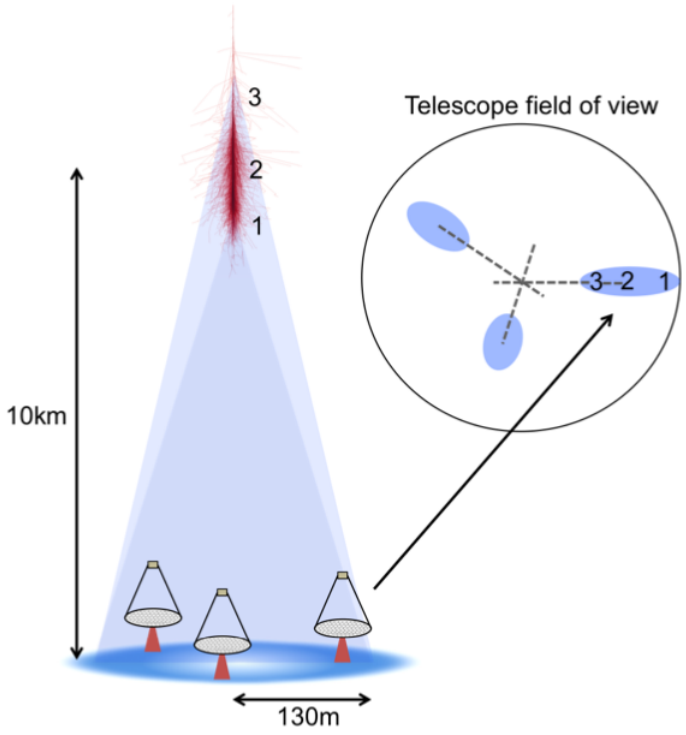

Figure 5.6: Cherenkov light pool from an electromagnetic shower and stereoscopic imaging of the event. Each telescope has a different view of the shower. Extending the major axes of the ellipses reveals the arrival direction of the gamma ray where they intersect in the camera plane. Taken from [54].

Images of EM showers and those of hadronic showers differ significantly in their size and shape. Gamma-ray images are generally smaller and are more likely to resemble an ellipse while cosmic-ray images are larger and more irregular (see Figure 5.7). Image parameters are therefore instrumental in discriminating between showers initiated by a gamma ray and those by a cosmic ray [28, 54]. The geometric parameters of the image, such as length and width, are called Hillas parameters [62]. These are used by analysis

packages proper to VERITAS to perform gamma-hadron separation, whereby the cosmic-ray background is cut out of the data.

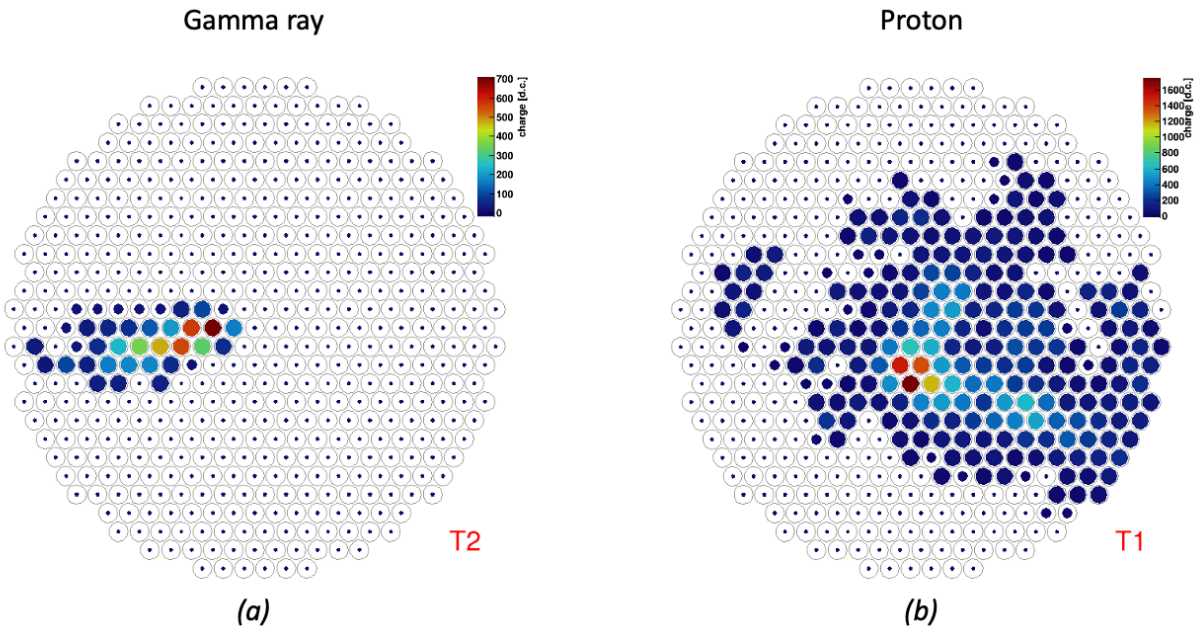

Figure 5.7: Images of a gamma-ray shower and a cosmic-ray shower as seen by VERITAS. Images were made by simulating an extensive air shower in the atmosphere using CORSIKA and processed using Eventdisplay. The colour scale represents the digital counts attributed to each of the 499 PMTs, which are 0.15°-wide pixels on the camera plane. (a) An electromagnetic shower initiated by a gamma ray. (b) A hadronic shower initiated by a proton. Gamma-ray images tend to be smaller and more likely to resemble an ellipse compared to the larger and more irregular cosmic-ray images.

5.5 Analysis packages

VERITAS analysis is traditionally done with one of two specialized analysis packages: Eventdisplay (ED) [63] and VEGAS [64]. Both are written in ROOT/C++ and perform the same tasks. Either package is usually used to confirm the results of the other. The

analysis stages—common to both, even though they do not share the same stage names nor code—are roughly as follows:

1. **Calculation of calibration parameters** (e.g., pedestal, gain, timing offset).
2. **Application of calibration and single-telescope image analysis**. This generates a data level (DL) 1 product.
3. **Event reconstruction**. Image parameters are determined and used to calculate event energy and shower core position and direction. This generates a DL2 product.
4. **Gamma-hadron separation**. Image parameters are used to separate gamma-ray events from cosmic-ray events. This generates a DL3 product.
5. **High-level analysis**. This produces binned data products (DL4) as well as analysis results (DL5): source detection analysis, spectral analysis, temporal flux analysis.

In addition to the two in-house packages, VERITAS has recently begun to incorporate Gammapy [65] in its analyses. Gammapy is an open-source Python-based package being developed for CTAO (the Cherenkov Telescope Array Observatory) [66] and is meant to be usable by all existing gamma-ray experiments. Before it can be used, Gammapy requires some pre-processing with either ED or VEGAS up to the step of gamma-hadron separation (DL3).

ED is the analysis package used in this work. The main script utilized is `evndisp` for its ability to recognize and analyze muon images.

5.6 Muon images

One notable source of noise during gamma-ray observations with VERITAS is the detection of circular rings or arcs attributable to muons landing in or near a telescope reflector.

Once produced in an EAS, muons travel through the atmosphere mostly undisturbed and can induce Cherenkov radiation in the air all along their path, from their creation until they hit the ground. Muons that arise from hadronic showers begin tens of kilometres above Earth's surface. A highly energetic muon ($E \gtrsim 1$ TeV or, equivalently, $\gamma \gtrsim 10^3$) is very unlikely to decay in its path (see Figure 5.5). Multiple scattering and the Earth's magnetic field have small effects on the trajectory of an ultrarelativistic muon [32]. Their longevity and negligible energy losses make (high-energy) muons the only Standard Model (SM) particles that may be comparable to MMs, from the perspective of an IACT. MMs could indeed share muons' ability of generating rings and arcs with VERITAS. To understand how a MM could be detected and imaged by VERITAS, it is worth looking at how muon images are formed.

5.6.1 Muons hitting the centre of a reflector

The simplest and clearest case of muon detection with VERITAS is a muon hitting the centre of one of the reflectors, either head-on or at a small angle with respect to the telescopes' pointing. The result of this event is the appearance of a full, uniform ring on the camera plane (see Figure 5.8(a)) [32]. This is explained by the fact that the telescopes are focused at infinity to view the sky and the reflectors are designed to translate photon angles into positions on the camera plane. Parallel rays hitting different parts of the reflector land on the same position in the PMT camera. So, although a muon hitting the reflector will bathe all mirror facets in Cherenkov light, the single polar angle (the Cherenkov angle) and all 360° in azimuth are translated into a clean, circular ring with a radius equal to the Cherenkov angle. Rings reach a maximum radius of 1.26°, corresponding to the angle produced in air at 1268 m a.s.l. by muons travelling at $\beta \sim 1$.

The angle of incidence of the muon with respect to the telescopes' pointing only affects the position of the ring image on the camera plane [32]. Because of VERITAS's 3.5° FOV, the ring begins to be cropped as the image moves off the plane when the muon's angle of incidence is greater than 0.5°. If the angle of incidence is above 3°, then the ring moves out of the PMT camera entirely and is thus no longer visible.

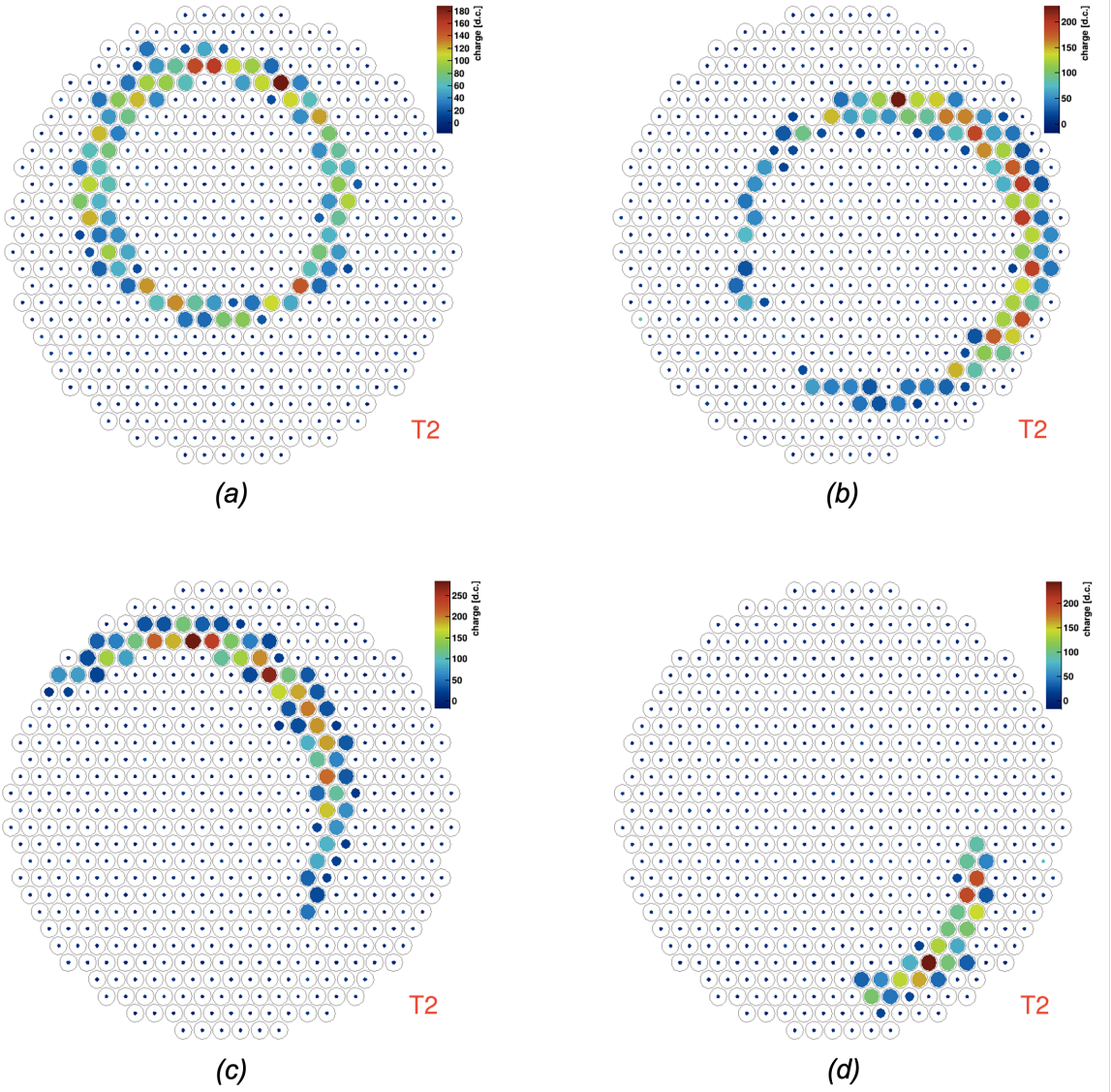

Figure 5.8: Muon images as seen by VERITAS. Images were made by simulating muons in the atmosphere using CORSIKA and processed using Eventdisplay. Each image is a separate event seen in T2 in the simulation pipeline. The colour scale represents the digital counts attributed to each of the 499 PMTs, which are 0.15°-wide pixels on the camera plane. (a) A complete, uniform muon ring. This suggests the muon travelled through the central part of the reflector. (b) A muon ring with differential intensity along its perimeter. The ring is still (nearly) complete, meaning the muon travelled through the reflector but did so off-centre. (c) A muon half-ring. This is caused by a muon hitting the edge of the reflector. (d) A small muon arc. The muon impacted outside the telescope.

For the null-impact scenario (i.e., a muon hitting the centre of the reflector), the total intensity of the ring in number of photoelectrons in a camera's PMT is dependent solely on the muon's speed and is given by integrating equation (3.2) over the relevant wavelengths and the relevant path length while accounting for telescope efficiency. The relevant length is also dependent on muon speed because of the geometry: Cherenkov photons begin to hit the reflector from a larger distance if the Cherenkov angle is smaller. This path length is simply

$$l \;=\; \frac{D}{2\,\tan\theta_c}\,, \tag{5.1}$$

where $D \;=\; 12$ m is the reflector diameter. Equation (5.1) relies on the approximation that the Cherenkov angle remains constant between the altitude at position $x = 0$ (on the ground) and the altitude at $x = l$. This is a safe approximation outside of the edge case of a muon near the threshold energy of ∼4.7 GeV, where the θ_c is extremely small at $x = 0$ and vanishing rapidly with altitude. Further applying the small angle approximation to θ_c and neglecting its small wavelength dependence, the double integration of equation (3.2) gives

$$N_{pe} \;=\; \pi\,\alpha\,D\,\theta_c \int_{\lambda_{\min}}^{\lambda_{\max}} \frac{\varepsilon\,R(\lambda)\,QE(\lambda)}{\lambda^2}\,d\lambda\,, \tag{5.2}$$

where ε is an overall efficiency factor (evaluated at 0.85 for VERITAS), QE is the wavelength-dependent quantum efficiency of the PMTs, and R is the average mirror reflectivity (also wavelength-dependent) [67]. With the approximations made, the integral with respect to wavelength is independent of Cherenkov angle and so it can be seen that the relationship between the number of photoelectrons and Cherenkov angle is linear. This relation is plotted in Figure 5.9. Equations (5.1) and (5.2) remain good approximations for particles with small incident angles with respect to telescope pointing.

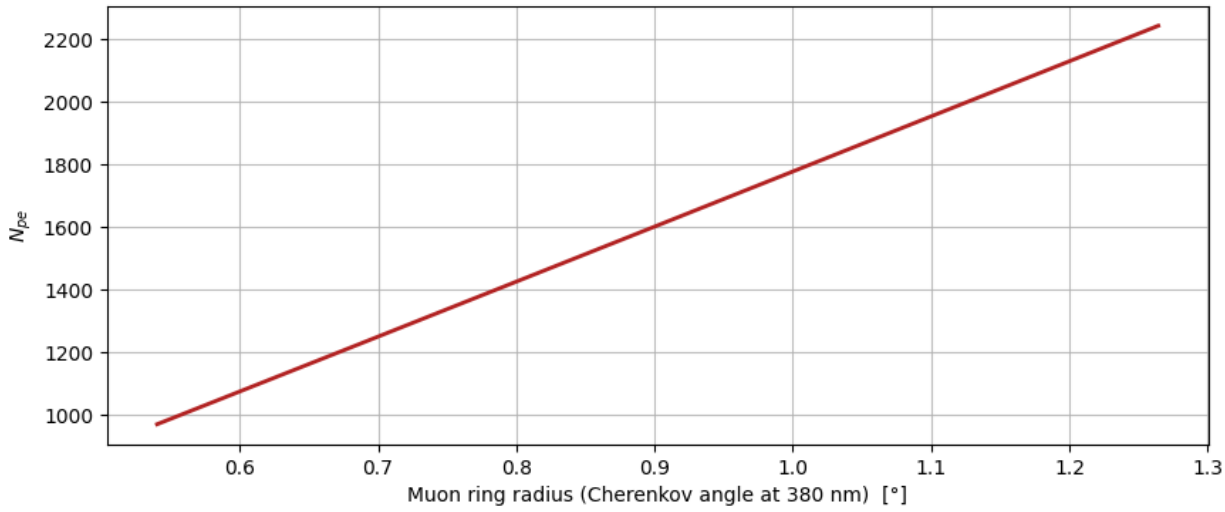

Figure 5.9: Total number of photoelectrons forming a ring image as a function of muon ring radius. This assumes the muon hits the centre of the reflector and has a small angle of incidence with respect to the telescope pointing. The ring radius is equal to the Cherenkov angle for a 380-nm photon at 1268 mm above sea level (the altitude of the VERITAS observatory). Muon ring radii below 0.54° are not plotted, as recognizable rings are not reliably produced by these muons. Ring radii reach an asymptotic limit at 1.26° when $\beta \sim 1$. This graph is produced by numerically evaluating equation (3.2) after including VERITAS efficiency factors. The relationship is very close to linear.

5.6.2 Muons hitting off-centre or outside a reflector

In general, a muon does not usually hit the centre of a reflector. The distance of a muon's impact from the centre (the impact parameter) changes the relative intensity along the azimuth of the ring [32]. With the loss of radial symmetry, the Cherenkov radiation received by the PMTs is no longer invariant with respect to the azimuthal angle of the photon (see Figure 5.8(b)). At an impact of $D/2$ (6 m), half the ring reaches zero intensity and thus vanishes in the image (see Figure 5.8(c)). With impacts greater than $D/2$, more and more of the ring is invisible, leaving an image of a smaller and smaller arc (see Figure 5.8(d)). Overall, the total integrated intensity of the muon image is always reduced as the impact parameter increases.

The relative total intensity compared to the null-impact scenario is

$$F(\xi) \,=\, \frac{2}{\pi} \int_0^{\psi(\xi)} \sqrt{1 \,-\, \xi^2 \sin^2 \varphi}\; d\varphi \,, \tag{5.3}$$

where ξ is the impact parameter in number of telescope radii and φ is azimuthal angle [32]. The normalized impact parameter ξ is measured on the plane of the reflector, which is not exactly level with the ground for pointings of non-zero zenith angle. The upper bound of integration $\psi(\xi)$ is an angle given by the piecewise function

$$\psi(\xi) \,=\, \begin{cases} \arcsin\left(1/\xi\right) , & \xi > 1 \\ \pi/2 \,, & \xi \leq 1 \,. \end{cases} \tag{5.4}$$

The total number of photoelectrons forming a muon ring or arc is therefore given by multiplying equation (5.2) by this factor $F(\xi)$, still assuming a small enough incidence angle with respect to telescope pointing. For impacts with $\xi \geq 1$, the angular length of the muon arc is given by $2 \arcsin\left(1/\xi\right)$ [32]. Figure 5.10(a) shows the relative intensity along the perimeter of the muon ring for different impact distances while the total intensity across the image is plotted against the impact parameter in Figure 5.10(b).

The maximum impact parameter for which Cherenkov photons can reach a reflector is a physical limit related to the geometry of the Cherenkov emission. For larger and larger impact parameters, the Cherenkov photons must come from higher and higher in the atmosphere. Yet, at greater heights, the Cherenkov angle is smaller and smaller (as per equation (3.4)). Figure 5.11 shows the how far from the charged particle a Cherenkov photon lands on the ground as a function of the altitude where it is emitted assuming the particle is descending with zero zenith angle[†].

[†]In the case of non-zero zenith angles, the x-axis of Figure 5.11 can also be interpreted as the distance from impact of a Cherenkov photon on the reflector plane (rather than on the ground), assuming the particle's incidence angle with respect to telescope pointing is small.

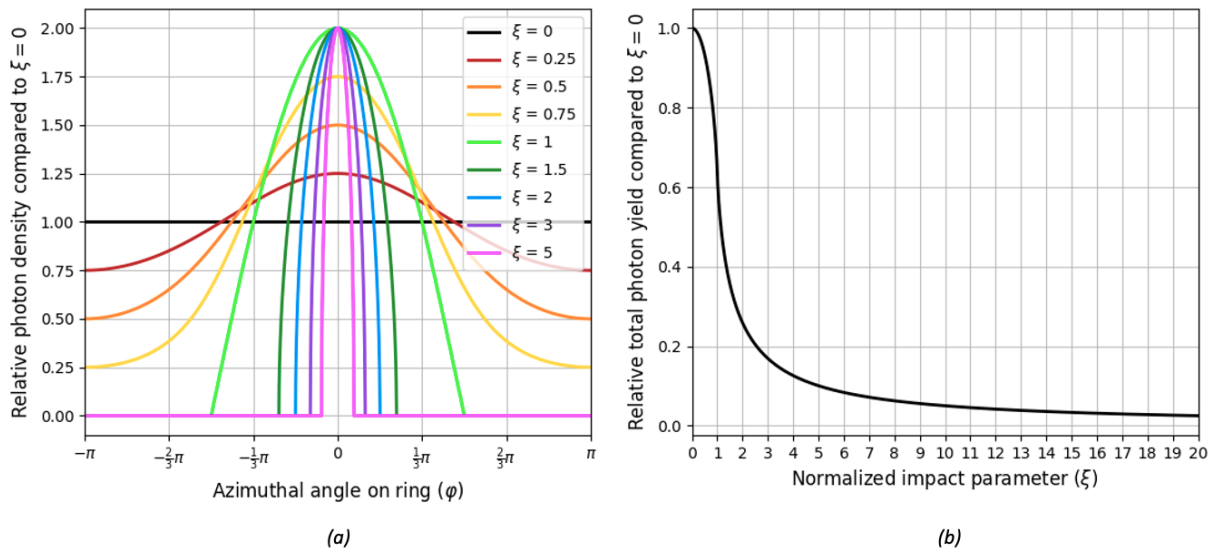

Figure 5.10: Variations in intensity in a muon image with respect to impact distance. (a) Relative photon density compared to the null-impact scenario ($\xi = 0$) as a function of azimuthal angle along the muon ring. For convenience, azimuthal angle $\varphi = 0$ is where the ring is the most intense. Different coloured curves represent different normalized impact parameters ξ, which is the impact distance from the reflector's centre divided by 6 m (reflector radius). At $\xi = 0$, the photon density is uniform along the ring. At $\xi = 1$, half the ring reaches zero intensity. For $\xi > 1$, the arc gets smaller and smaller with increasing impact distance. (b) Total integrated intensity in a muon ring image as compared to the null-impact scenario ($\xi = 0$) as a function of the normalized impact parameter. For every ξ in this curve, the y-value is the area under the corresponding curve in (a). This plot is described by equation (5.3). Although some parts of the ring may become more intense with increasing ξ, the overall intensity in the whole image is always decreasing with larger ξ.

A Lorentz factor around 50 ($E \sim 5.3$ GeV) is probably the lower limit for a muon to produce a reasonably recognizable ring image with VERITAS. Charged particles with $\gamma \lesssim 50$ will induce Cherenkov photons with angles between 0 and no more than 0.54° that all land within 6 m of the impact point (see Figure 5.11). Consequently, when these lower-energy muons strike the reflector, they tend to produce small discs rather than true

rings. Given that VERITAS PMTs each have a size of $\sim$0.15° on the camera plane, these discs are only about seven pixels wide or less.

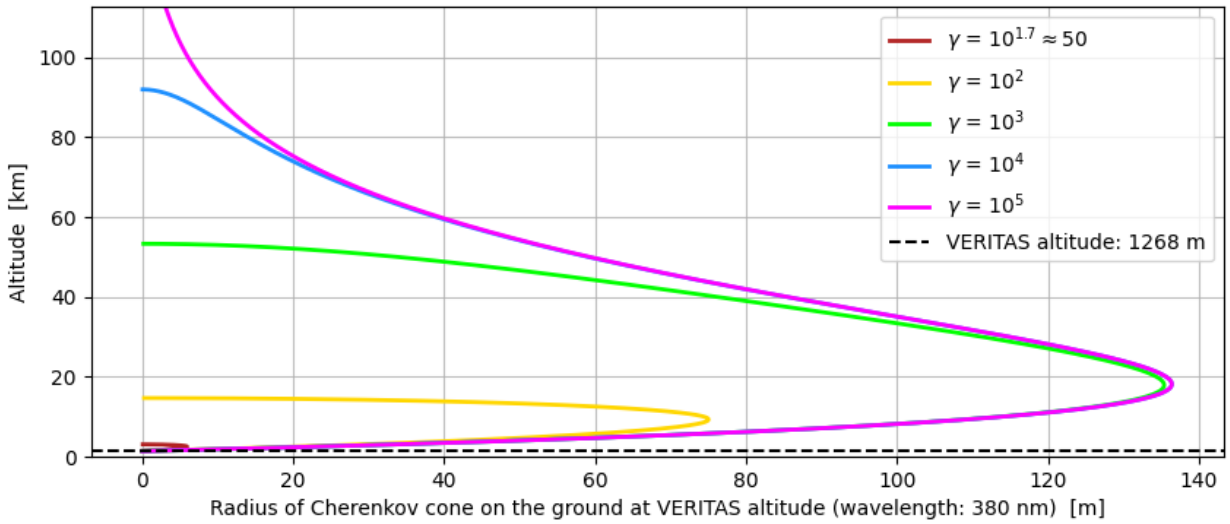

Figure 5.11: Radius of cone on the ground with respect to emission altitude of a 380-nm Cherenkov photon in the case of a charged particle arriving from 0° zenith. The dashed line represents the ground at 1268 m above sea level (the altitude of the VERITAS observatory). Different coloured curves represent different Lorentz factors of the responsible charged particle (e.g., muon). As the particle descends through thicker atmosphere, the Cherenkov angle opens, but the ground gets closer. For the highest-energy particles, the radius of the Cherenkov cone on the ground reaches a maximum limit of $\sim$136 m. For particles with $\gamma \lesssim 50$ (red curve), the radius on the ground never exceeds 6 m (the radius of a VERITAS reflector). The emission associated with the upper part of each curve is much weaker than that of the lower part and is unlikely to contribute to forming an observable image with an IACT. The Cherenkov cones from particles descending with non-zero zenith angles draw ellipses on the ground, rather than circles, with semimajor axes greater than the radii shown here. An alternative interpretation of the x-axis, in the context of VERITAS telescopes pointing in the direction of the incoming particle, is the distance from impact that the 380-nm Cherenkov photon hits the reflector plane (rather than the ground).

5.6.3 Ring broadening

Many factors contribute to the thickness of a muon ring or arc [32]:

- **Pixel size.** Due to the VERITAS pixels' discrete size, the minimum width a ring can have on the camera plane is 0.15° and increases in width go up in steps of 0.15°.
- **Mirror aberrations.** Imperfections in the reflector mirrors can occasionally send the Cherenkov photons to the wrong PMT, creating a broader image. This effect is small but likely the most important factor in ring broadening overall.
- **Variability of Cherenkov angle with wavelength.** As illustrated in Figure 3.3, the refractive index of air is slightly dependent on wavelength. As such, bluer Cherenkov photons are emitted at a marginally larger angle than redder photons. This differential gives width to the ring image appearing on the camera plane but is a very small effect.
- **Variability of Cherenkov angle with altitude.** As can be seen in Figure 3.4, the refractive index of air increases considerably with descending altitude. Cherenkov photons emitted lower in the atmosphere have a larger angle than those emitted above, resulting in a wider ring image. However, the path length responsible for the Cherenkov photons that reach a telescope is relatively small (see equation (5.1)), and so this effect is very limited.
- **Muon multiple scattering.** As a muon descends through the atmosphere, it experiences Coulomb scattering that diverts it in its trajectory. For an ultrarelativistic particle ($\beta \sim 1$), the deviation from a straight line follows an approximately Gaussian distribution with a standard deviation that is inversely proportional to the particle's linear momentum. Consequently, this effect is more pronounced for lower-energy muons. The changing incline of a muon's path broadens the ring image by slightly shifting the ring position on the camera plane as Cherenkov photons are received. Overall, multiple scattering is the biggest factor contributing to ring broadening for the smaller rings created by lower-energy muons. This effect becomes much less important for muons with higher energies.

- **Muon energy losses.** As a charged particle loses energy by ionizing particles in the air, its speed must decrease. Energy loss due to ionization is inversely proportional to a particle's mass and largely independent of its energy. In the energy regime of muons capable of inducing Cherenkov radiation, ionization losses are very small compared to the total energy of the muon. Any decrease in β and in Cherenkov angle are therefore negligible. This is the smallest effect impacting muon ring broadening.

5.6.4 VERITAS calibration using muon rings

Muons being the only SM charged particles with a relatively stable trajectory through the atmosphere at the energies involved, the ring and arc images they produce in an IACT are a notable signature, distinguishable from the shower images produced by gamma rays and cosmic rays. The relationship between ring radius and number of photoelectrons detected—as described by equation (5.2) for muons landing in the centre of a reflector—becomes an important and reliable tool in calibrating the telescope [67, 68].

The normalized impact parameter can be found by evaluating the distance between the centroid of the ring image and the centre of the ring [67]. The total measured intensity in the image can thus be corrected to the equivalent null-impact scenario using equation (5.3). Impact-corrected muon events from VERITAS observation runs can populate a ring radius vs. intensity graph, with intensity (also referred to as muon "size") measured in number of digital counts (d.c.). The ratio between the slope fit to the ring vs. size graph and the slope in Figure 5.9 (where intensity is in number of photoelectrons) gives the gain of the telescope, i.e., the number of d.c. recorded per photoelectron detected [67].

VERITAS constantly receives detectable muon signals regardless of where the telescopes are pointing. However, compared to the number of muon ring images that are potentially observable, relatively few muon events are actually saved during observations. Because they are in fact so abundant, one of the reasons for VERITAS's three-level trigger system (particularly L3) is to discard images produced by muons [59]. Without

the L3 trigger, muons would become a tremendous background. Muon rings and arcs are in fact very local events. If a full ring is visible in one telescope, it is not very likely that an image of this same muon will form in another telescope given their distances within the array (see Figure 5.3). This is because, although a muon with enough energy has the potential to send Cherenkov photons over an area with radius greater than 100 m (see Figure 5.11), the signal is suppressed at large impact distances (see Figure 5.10(b)). A muon arc is able to appear in more than one telescope if the muon hits a location in the array close enough to two or more telescopes, which can be sufficient to pass all three trigger levels. Full muon rings can also pass L3 if they coincide with other events detected in other telescopes. It is not uncommon for a muon ring to be accompanied by the detection of a cosmic-ray event as muons are born from hadronic showers.

5.7 Using VERITAS to search for magnetic monopoles

Under the assumption that ultrarelativistic MMs remain stable and conserve their energy as they traverse the atmosphere, their Cherenkov emission should create images that resemble muon rings and arcs. For the same Lorentz factor, the Cherenkov angle—and therefore image radius—should be identically $\arccos(1/(\beta\, n))$ for both MM and muon. The largest distinction is in the number of emitted Cherenkov photons: bearing a magnetic charge g instead of an electric charge e, a MM would be responsible for an emission 4697 times greater (in air at the altitude of VERITAS). For the same ring radius, a MM image would have that much more intensity than a muon image. This is the same defining characteristic of MMs that motivated searches with neutrino experiments (see Section 4.2).

The question then becomes what appearance a MM image would have with VERITAS and whether or not it would be easily distinguishable from a muon image. To answer this question, ultrarelativistic MMs are simulated using the VERITAS simulation pipeline and processed with Eventdisplay. A large number of muons are also simulated to produce a background to which the MMs are compared. The analysis of these simulations can then inform a search through VERITAS observation runs.

Chapter 6

Event simulations

6.1 The VERITAS simulation pipeline

The VERITAS simulation pipeline `VTS-SimPipe` [69] is used in the VERITAS collaboration to simulate EM and hadronic showers. They are crucial in calculating the instrument response functions of the telescope. It is thanks to these simulations that VERITAS is able to convert image parameters into shower energies as well as determine effective areas, necessary to calculate a flux. `VTS-SimPipe` makes use of three programs in succession: CORSIKA [3] to simulate air showers and produce Cherenkov photons that reach the ground, GrOptics [70] to simulate the ray tracing of the photons reflected by the VERITAS mirrors into the camera, and CARE [71] to simulate the response of the photomultiplier tubes (PMTs) as well as the electronics.

6.1.1 CORSIKA

CORSIKA (the COsmic Ray SImulations for KAscade) is a Monte Carlo extensive air shower simulator originally written in 1989 by Dieter Heck, Tanguy Pierog, and Johannes Knapp for the KASCADE (KAarlsruhe Shower Core and Array DEtector) experiment [72, 73]. With an eighth version currently in development, CORSIKA is widely used in modern gamma-ray, cosmic-ray, and neutrino experiments. The program is coded in standard FORTRAN. CORSIKA version 7 is used in this work.

CORSIKA tracks the transport of particles in the atmosphere while simulating hadronic interactions (differently for high and low energies) and electromagnetic (EM) interactions [72]. Additionally, it tracks the decay of unstable particles. In a particle's path through the atmosphere, CORSIKA considers energy losses from ionization as well as deflections due to multiple scattering and the geomagnetic field. Nominally, particles with energies up to 10^{11} GeV can be simulated [72]. The atmosphere is modelled in several layers to account for the altitude-dependent change in density. By default, simulated primary particles start at the top of the atmosphere (112.8 km or otherwise depending on the model), but the starting point can be set lower by the user. Parameters for the geomagnetic field and for the atmosphere are input by the user as appropriate for the location of the simulated observatory. CORSIKA has preset definitions for a variety of primary particles: photons, charged leptons, neutrinos, mesons, baryons, as well as nuclei up to a nuclear mass of $A = 56$ [72]. However, CORSIKA has no definition for any kind of MM nor any beyond-Standard Model (SM) particle.

Add-ons allow CORSIKA to additionally simulate Cherenkov radiation from the primary and secondary particles of an air shower [72]. With the selection of the appropriate options, CORSIKA can be set to consider the wavelength-dependent index of refraction in air. Atmospheric refraction of Cherenkov photons travelling through the atmosphere, although small, can also be taken into account. In the context of `VTS-SimPipe`, only Cherenkov photons that reach a telescope* on the observation level are recorded—there is no use for the data on the multitude of simulated secondaries to be saved.

6.1.2 GrOptics

GrOptics is a ray-tracing program written in ROOT/C++, designed in part for VERITAS telescopes. GrOptics receives simulated Cherenkov photons from CORSIKA, traces those photons' paths through the telescope, and outputs to CARE (see Section 6.1.3) the photons that successfully strike the camera. GrOptics simulates the telescope pointing with

*For the purposes of CORSIKA, the program only cares if a Cherenkov photon intersects a predefined volume around a telescope. GrOptics later considers whether or not a photon hits a mirror.

respect to the incoming radiation while considering the position and orientation of the hexagonal mirrors that make up the reflector as well as their reflectivity [74]. Figure 6.1(a) shows the average reflectivity for each of the VERITAS telescopes. Additionally, GrOptics simulates photon shadowing, which is when a photon cannot strike a mirror because it is intercepted by one of the telescope's quad arms, which hold up the camera, or by the camera box itself (seen in Figure 5.1). The extinction of Cherenkov photons in the atmosphere is also statistically taken into account at this stage.

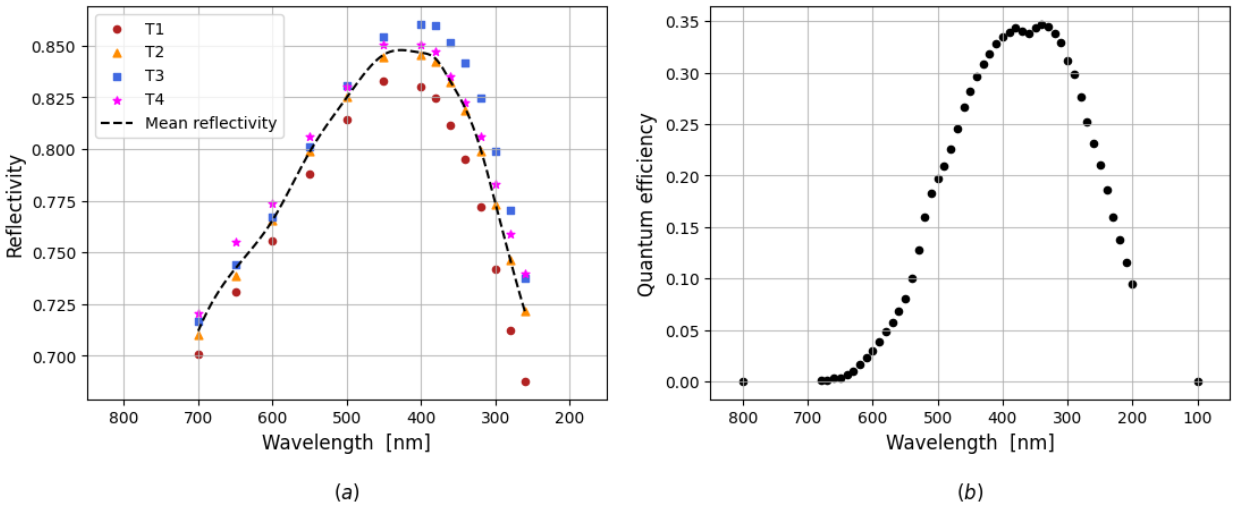

Figure 6.1: (a) Wavelength-dependent reflectivity of VERITAS reflectors (T1 through T4). Data points are taken from [69] and come from measurements made in 2011. The black dashed curve represents the interpolated average of all four reflectors. (b) Wavelength-dependent quantum efficiency of VERITAS PMTs. Data points are taken from [69].

6.1.3 CARE

CARE—which stands for "CAmera and REadout"—is a ROOT/C++ program written to simulate the VERITAS camera response. It receives photon information (wavelength, location on the focal plane, and time of arrival) from GrOptics and translates it into the digital signal written onto a VERITAS bank format (VBF) file—a binary file which contains raw telescope data. CARE considers the positions of all the PMTs in each camera and

their quantum efficiency [71]. Figure 6.1(b) shows the quantum efficiency of the Hamamatsu R10560-100-20 PMTs. CARE notably simulates all three levels of the VERITAS trigger system (see Section 5.3). CARE also simulates night sky background (NSB) in the PMTs.

Figure 6.2 is a redrawing of Figure 3.6 that takes into account reflectivity, quantum efficiency, and an overall efficiency factor of 0.85 to show the Cherenkov spectrum as detectable by VERITAS.

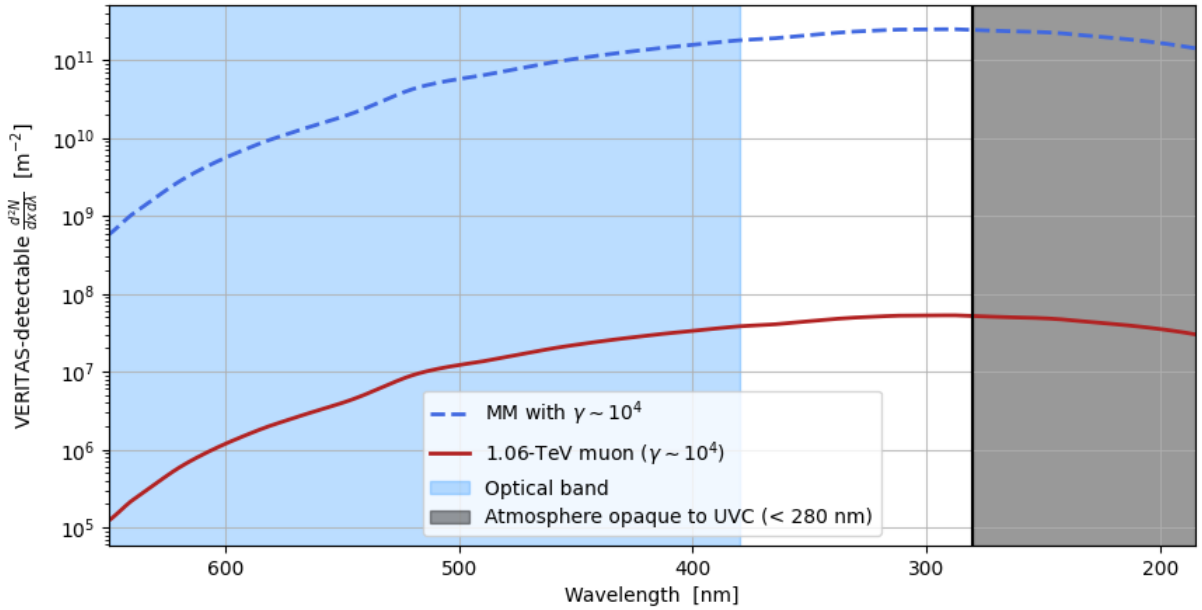

Figure 6.2: VERITAS-detectable atmospheric Cherenkov spectrum. Shown spectra are of a magnetic monopole (dashed blue curve) and a muon (solid red curve), both with $\gamma \sim 10^4$. These are the same spectra from Figure 3.6 multiplied by the instrument's wavelength-dependent efficiency factors. Atmospheric absorption is not incorporated into these curves. Instead, the grey shaded region represents (<280 nm), where atmospheric absorption quickly reaches nearly 100%.

6.2 Simulating magnetic monopoles

Since CORSIKA has no predefined MM as a primary particle, a MM have to be "engineered" by using another particle type. The natural choice for simulating a MM with CORSIKA is to start with a muon. As evoked at the start of Section 5.6, muons are the SM particles most resembling MMs in the context of interactions in the atmosphere. At high enough energies, a muon travelling through the atmosphere will induce Cherenkov radiation continuously until it reaches the ground, with a very low chance of decaying or starting a shower. If MMs must remain stable to conserve magnetic charge, this matches their expected behaviour.

To simulate a MM with $\gamma = 10^4$, a muon energy of $E = 10^4\, m_\mu c^2 = 1.06\,\mathrm{TeV}$ (where $m_\mu \approx 0.106\,\mathrm{GeV}/c^2$ is the muon mass [25]) is chosen. The mass of the simulated MM does not need to be increased from its preset m_μ to the scale of an intermediate-mass MM (IMM) because this has no effect on the Cherenkov emission. While all simulated MMs are monoenergetic at the equivalent muon energy of 1.06 TeV, background muons are simulated at energies ranging from 5.3 GeV to 10 TeV in order to recreate a plausible muon background and populate a ring radius vs. size graph (see Figure 5.9). CORSIKA distributes primary particle energies according to a power law,

$$\frac{dN}{dE} \propto E^{-\Gamma}\,, \tag{6.1}$$

with an index Γ being selectable by the user. An index of 2.7 is chosen for the simulated background muons as this matches the power law index of the energy distribution of cosmic rays detected by VERITAS [28].

Cherenkov photon output

Most importantly, the Cherenkov output of the simulated MM has to be multiplied by 4697 to match the modified Frank–Tamm formula for MMs (equation (3.6)). This is done by inserting a Python script between the CORSIKA and GrOptics stages which duplicates all the Cherenkov photons written in the photon data file by CORSIKA. This reuse of the

same photon information (direction, position, arrival time, wavelength) is not expected to make the simulation more granular. The initial number of photons output by CORSIKA for a muon with energy >100 GeV is on the order of 10^6 and only a fraction of these end up reaching the PMTs (because of factors like reflector area and orientation, reflectivity, and quantum efficiency). The photon multiplication limits the efficiency of simulating large number of MMs as it much more work for CARE and requires a large memory allocation.

Multiple scattering and geomagnetic field effects

With $\gamma \gtrsim 10^3$, both muons and MMs are expected to suffer very little energy loss in their descent. Multiple scattering becomes negligible for muons with very high momenta and especially so for IMMs given their larger mass. It is unfortunately not possible to modulate or turn off muon multiple scattering in CORSIKA without making substantial modifications to the code and recompiling the program. It was decided that it is not necessary to do this given the high Lorentz factor of the simulated CORSIKA muon masquerading as a monopole. The effect of Earth's magnetic field is not the same on muons as it is on MMs but is small in both cases. To replicate the smaller deflective effect of the geomagnetic field on a MM compared to that on a muon of the same speed, the magnetic field strength is reduced by a factor of 10^4 of its `VTS-SimPipe` values in CORSIKA for simulated MMs—this reduction reflects the case for a monopole mass of 10^5 GeV/c^2. The direction of the deflection is also corrected for the monopole case.

Starting altitude

While muons generally start their journey at ∼10 km above ground level, cosmic MMs stream down from the top of the atmosphere. In the case of both particles, Cherenkov photons hit a reflector if they are emitted from a position between ground level and ∼272 m up the particle's path (see equation (5.1))—assuming a normalized impact parameter $\xi \sim 0$. This length moves up with increased impact parameter; for example, in the case of $\xi \sim 3$, the interval shifts up to between about 544 and 1087 m up the particle's path. However, as Figure 5.11 reveals, Cherenkov photons emitted very high in the atmo-

sphere (around an altitude of 90 km for particles with $\gamma \sim 10^4$ impacting the telescope) where the Cherenkov angle is extremely small, have the potential of reaching the reflector as well. Cosmic MMs should generate these photons as they pass, whereas muons are very unlikely to exist at this height. Nonetheless, the Cherenkov emission at this height is suppressed by the smallness of the angle. Also revealed by Figure 5.11, at large impact parameters for particles with large γ, these two emission points become closer in altitude (the higher emission point sinks lower while the lower emission point is higher). Yet, with impact parameters larger than $\xi \sim 5$, an arc image barely spans a few pixels in the camera plane and becomes virtually unrecognizable. For these reasons, both simulations of control muons and of MMs need not start in the atmosphere at much higher than 1100 m from above ground level, disregarding the higher emission of very small Cherenkov angle and focusing the analysis only on one telescope near the impact point. (This is a departure from Spengler's method with H.E.S.S. [51].) This shortened starting height also greatly limits the deflections that might be caused by multiple scattering and by the geomagnetic field.

Scatter radius

To control for impact parameter, only one telescope (T2) is targeted in all simulations. This is done by dramatically reducing the scatter radius of particles in CORSIKA and moving the position of T2 to the centre of the array. This strategy of targeting a single telescope requires the deactivation of the L3 trigger in CARE. For simulated background muons, the scatter radius is set to 18 m. This produces normalized impact parameters ξ between 0 and 3. At $\xi = 3$, the arc image is $2\arcsin(1/\xi) \approx 40^\circ$. For a radius of 1.26° on the camera plane and considering that each pixel covers 0.15°, the arc image spans five or six pixels. This is judged to be a reasonable limit for recognizable arcs. Simulated MMs are confined to a smaller area by selecting a scatter radius of 7 m. This gives possible impact parameters ξ between 0 and 1.2 and a minimum arc of 118° (∼17 pixels). Considering the much smaller number of MMs being simulated, this smaller scatter radius is chosen to give a probability of ∼73% of MMs striking the reflector to produce a full ring image (as opposed to the ∼11% of simulated background muons). Because simulated MMs are

made to impact closer to the centre of T2 than simulated muons, it is possible to lighten the MM simulation by having monopoles start at a slightly lower altitude.

Atmosphere

`VTS-SimPipe` uses two different atmospheric models for the observatory site: "ATM 61" for the winter season and "ATM 62" for summer. These two models are characteristically different in their humidity. For the purpose of this work, the choice is made to simulate in ATM 61 only. CORSIKA simulates the atmosphere as flat layers, although a "CURVED" option exists for simulating a spherically accurate atmosphere. The use of this option improves air shower simulations only marginally and begins to matter only for zenith angles over 60° [75], which are rare pointings for VERITAS. For this reason, `VTS-SimPipe` does not utilize the CURVED option nor do the simulations in this work.

Zenith angle, night sky background, and wobble

Six CORSIKA-simulated monoenergetic MMs (with $\gamma = 10^4$) are appended to a simulated background of 100,000 muons. All particles are set to travel at a zenith angle of 10°, chosen in CORSIKA. GrOptics ensures that the telescope is pointing in the arrival direction of the simulated particle plus a pointing offset called "wobble." A NSB of 100 MHz is selected for CARE. Zenith angle and NSB are fixed values because these are expected to have only second-order effects on the detection and analysis of ring images. On the other hand, the pointing offset matters a great deal. As evoked in Section 5.6.1, ring and arc images are cropped for an offset between 0.5° and 3° and fall completely off the camera beyond that. Eventdisplay struggles with tracing rings and arcs when they are cropped, so a maximum wobble is chosen to be 1.4°. Fifteen wobbles are selected between 0.0° and 1.4°, inclusively. In `VTS-SimPipe`, each choice of wobble reuses the output from the CORSIKA stage to produce a separate run. In total, 1,500,090 events are obtained for analysis.

Table 6.1 shows the parameters chosen for the simulations in this work.

Table 6.1: Selected parameters for simulated magnetic monopoles and muons

Simulation parameters	Monopoles	Muons
Number simulated	6	100,000
Equivalent muon energy [GeV]	1.06×10^3	5.3–10^4
Power law distribution index	n/a	2.7
Scatter radius [m]	7	18
Starting altitude [m]	2000	2500
Atmosphere	ATM 61	
Zenith angle [°]	10	
Night sky background [MHz]	100	
Wobbles [°]	0.0–1.4	

Chapter 7

Results

7.1 Simulation results

With the choices described in Section 6.2, `VTS-SimPipe` outputs 15 VERITAS bank format (VBF) files—one for each pointing offset—for the simulated MMs and for the simulated muon background. Using Eventdisplay (ED) to visually inspect the images of the six MMs confirms that they are indeed recognizable rings and arcs with very high counts (see an example monopole ring and arc in Figure 7.1). In these monopole images, photomultiplier tubes (PMTs) are saturating at $\sim$7000 digital counts (d.c.) (compare this with Figure 5.8, where an individual image-forming PMT does not reach 300 d.c.). The simulation seems to have failed for one of the six MMs (event 4 is missing in the 15 monopole VBFs). The reason for this failure is unclear but it may be due to CARE being overwhelmed with the number of photoelectrons in this event.

ED's first stage (`evndisp`) provides an option to automatically find and parametrize muon images. With this option turned on, the DL1 product records, for each muon image:

- the ring centre position,
- the centroid position,
- the ring radius,

- the uncertainty on ring radius,
- the size (total number of d.c.),
- the impact-corrected size.

The impact-corrected size is equal to the size divided by the factor $F(\xi)$ from equation (5.3) to give the equivalent size the image would have if the impact point was at the centre of the reflector. ED determines $F(\xi)$ by using the ring radius θ_c and the distance d_c between centre and centroid positions on the camera plane [67], which are related by

$$\frac{\theta_c}{d_c} = \frac{2\,F(\xi)}{\xi}\,. \tag{7.1}$$

While ED does not record the normalized impact parameter ξ, it can be recovered by solving equation (7.1) or by dividing the true size by its impact-corrected value and inverting equation (5.3). Naturally, both methods yield the same result.

Although all simulated MMs except one produce an image in each of the 15 wobbles, ED is not able to reconstruct and parametrize all the images. No simulated MMs are successfully reconstructed for offset angles greater than 0.5°. For MMs and for muons, ED can only measure a size for full rings, discarding arcs and nearly all cropped images. This limitation is discussed in more detail in Chapter 8. Since the vast majority of background muons—simulated with a scatter radius of 18 m—land outside the 6-m-radius reflector, ED only reconstructs 4039 muon images in the 0° wobble result. This number drops to 3027 for the 0.5° case and to only 302 for 1.1° wobble, as more and more ring images get cropped—with increasing wobble, rings with a larger radius will crop first while those with smaller radius can stay contained within the field of view (FOV).

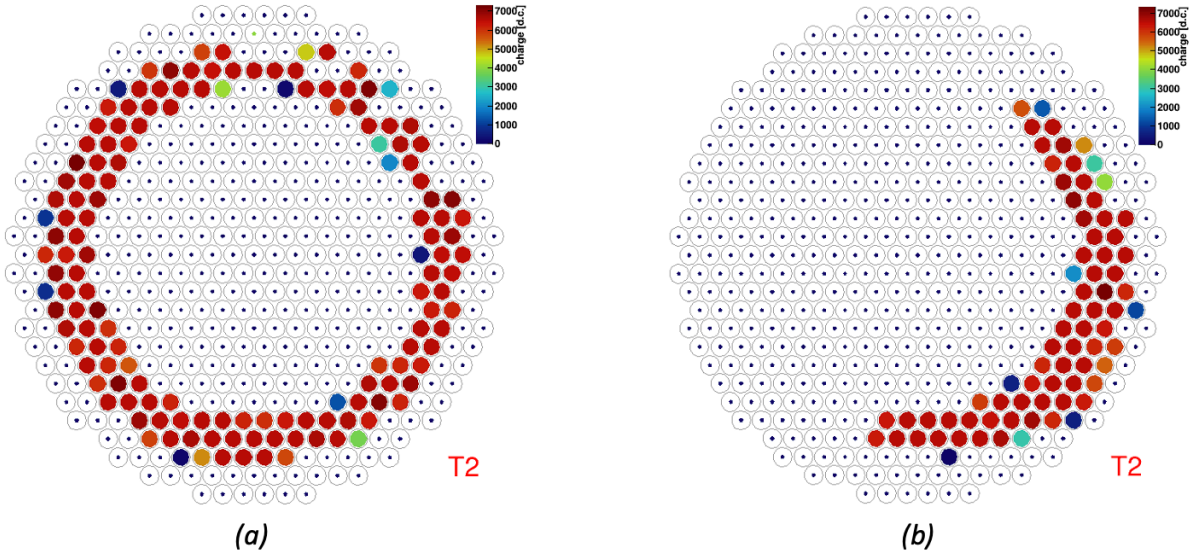

Figure 7.1: Monopole images as would be seen by VERITAS. Images are the result of the simulation with parameters presented in Table 6.1 and are processed with Eventdisplay. The colour scale represents the digital counts attributed to each of the 499 PMTs, which are 0.15°-wide pixels on the camera plane. PMTs forming the images reach saturation around 7000 d.c. Compare to muon images in Figure 5.8. (a) Monopole ring resulting from event 1 (0° wobble shown). (b) Monopole arc resulting from event 5 (0° wobble shown).

The quality of the image reconstruction can be judged by the uncertainty on the ring radius. This value is simply the standard deviation of the distance each ring pixel has from the ring centre. In all wobbles up to 1.1°, the distribution of these uncertainties is highly peaked around 0.06°–0.07° with a long tail reaching slightly beyond 0.35°. The distribution flattens with increasing offset angle, becoming nearly uniform at 1.4° wobble. Figure 7.2 shows the distribution of uncertainties in the 0° wobble result. A threshold of 0.12° in radius uncertainty is chosen to cut away images that are deemed too poorly reconstructed. The selection of this cutoff is such that it is the smallest threshold that preserves all the reconstructed monopole images. The rather large thickness of monopole rings could explain why they lie on the higher end of the radius uncertainty peak. The same cut is performed on all DL1 files. After this quality cut, there are 3945 surviving

muon images in the 0° wobble case, 2936 for 0.5° wobble, and 226 for 1.1° wobble. Table 7.1 presents the ring images found by ED and those surviving the quality cut for each iteration of offset angle. The number of images for different ξ intervals is presented as well. The implications of the offset angle and impact parameter dependence in ED's performance are examined in Chapter 8.

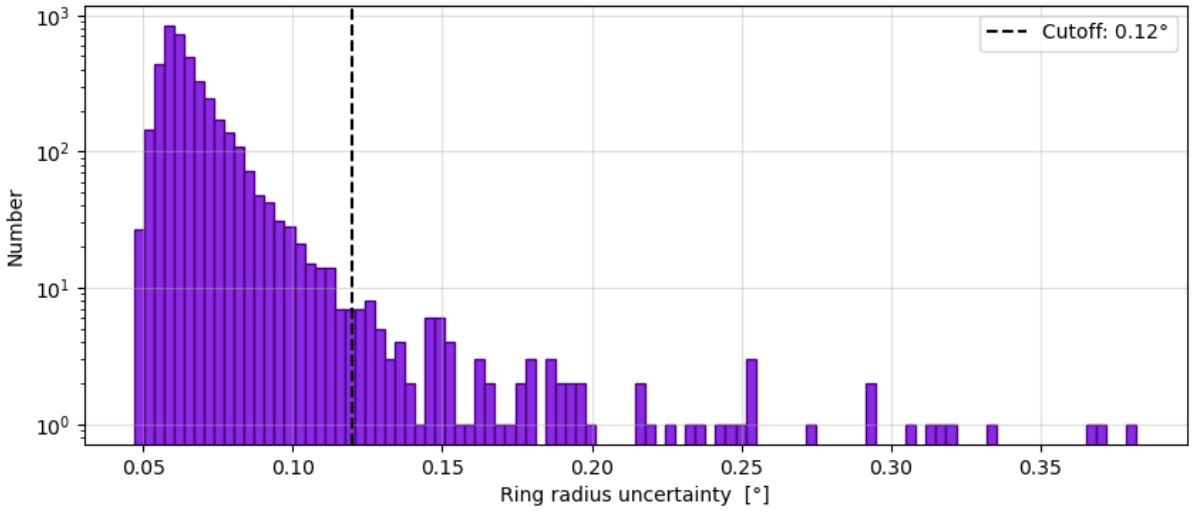

Figure 7.2: Distribution of ring radius uncertainties for reconstructed images resulting from simulation with 0° wobble (monopoles and muons combined). A cutoff is applied at 0.12° to discard poorly reconstructed events.

Table 7.1: Ring images processed from simulation results

	Monopoles			Muons			N_{rings} after cuts per ξ interval (monopoles and muons combined)					
Wobble [°]	Generated	Found	After cuts	Generated	Found	After cuts	$\xi \in [0.0, 0.2)$	$\xi \in [0.2, 0.4)$	$\xi \in [0.4, 0.6)$	$\xi \in [0.6, 0.8)$	$\xi \in [0.8, 0.1)$	$\xi \geq 1.0$
0.0	6	4	4	10^5	4039	3945	459	995	1193	1111	191	0
0.1	6	4	4	10^5	4043	3943	463	968	1216	1104	196	0
0.2	6	3	3	10^5	4028	3938	487	975	1197	1084	198	0
0.3	6	4	4	10^5	3978	3883	429	983	1233	1077	165	0
0.4	6	3	3	10^5	3700	3607	390	910	1153	971	186	0
0.5	6	3	3	10^5	3027	2936	274	785	1011	748	121	0
0.6	6	0	0	10^5	2243	2135	200	548	765	543	79	0
0.7	6	0	0	10^5	1578	1488	140	429	517	365	37	0
0.8	6	0	0	10^5	1133	1030	104	288	367	243	28	0
0.9	6	0	0	10^5	789	686	68	180	259	163	16	0
1.0	6	0	0	10^5	489	392	43	112	143	81	13	0
1.1	6	0	0	10^5	302	226	26	69	69	55	7	0
1.2	6	0	0	10^5	180	103	6	33	43	18	3	0
1.3	6	0	0	10^5	115	57	6	17	18	14	2	0
1.4	6	0	0	10^5	56	17	1	4	9	3	0	0

The parameters of the simulated MM and muon events which survive the quality cuts are used to produce a plot of ring radius vs. impact-corrected size. The resulting graph for the 0° wobble case is shown in Figure 7.3. In the six cases where they are reconstructed by ED (wobbles 0° through 0.5°), the MM rings appear in a background-free region of the parameter space, far above the linear relationship traced by the muon rings. The impact-corrected size of a MM ring is two orders of magnitude greater than that of a muon ring with the same radius. This demonstrates that, under the right conditions, VERITAS is capable of identifying ring images that would be formed by MMs in its muon analysis software and that these images appear unambiguously distinct from all those produced by muons. A search for MM candidates among the ring images picked up by ED is therefore feasible.

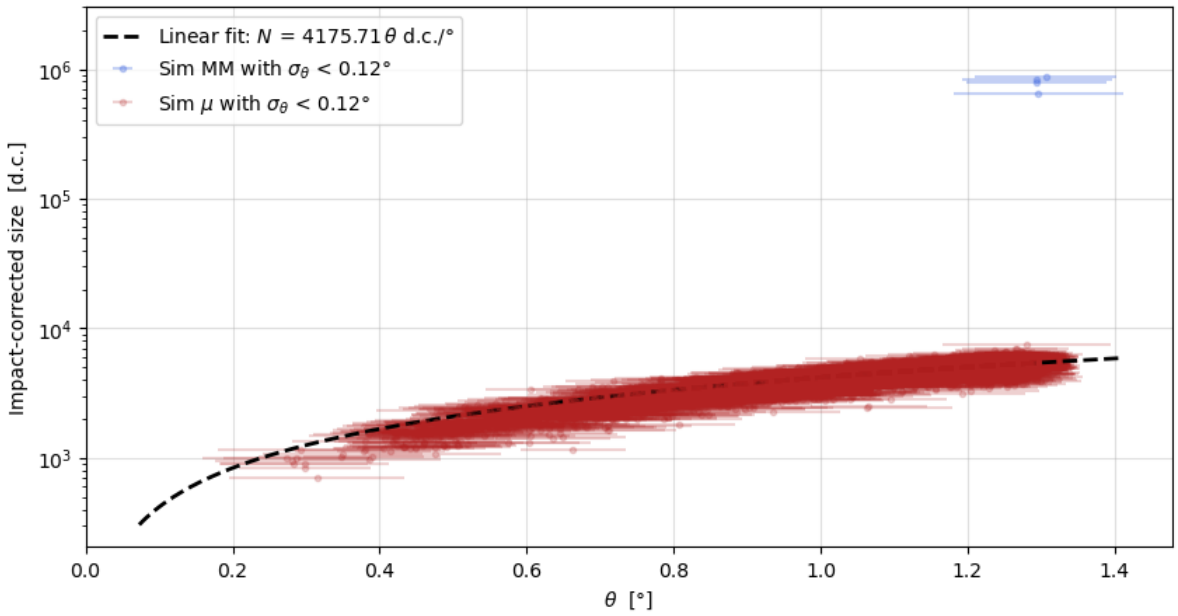

Figure 7.3: Impact-corrected ring size as a function of radius (θ) for well reconstructed images resulting from simulation with 0° wobble. An image is considered well reconstructed if the uncertainty on its radius is smaller than 0.12°. The four MM rings (blue data points) are far above the muon rings (red data points), in a background-free region of the parameter space. A linear fit to the muon images is plotted (dashed black curve). The fit does not appear linear because the y-axis is logarithmic while the x-axis is not.

7.2 Analyses of observation runs

In order to demonstrate this method of searching for ultrarelativistic MMs, the ED muon analysis done on the simulations is repeated with three VERITAS observation runs. The first selected run (number 62338) is a single-telescope 20-minute observation from May 2012 (just before the PMT upgrade) pointing at a region labelled "DARK_044_8.05." This is a region of the sky with no known gamma-ray source and where the brightest star has a visual magnitude of 8.05. Dark regions such as this one are targeted regularly for calibration purposes. Run 62338 uses only telescope T3 and bypasses the L3 trigger. A label associated with this run indicates that it was taken for a muon study—which explains the need to remove the barrier posed by L3. This single-telescope run is chosen because its muon image population should resemble that of the simulations produced for this work. Owing to the fact that VERITAS's purpose is for observations that take advantage of the entire array, there are no single-telescope runs that were found to have the same length and quality as 62338 from after the PMT upgrade. The second run (number 111644) is a 30-minute observation with all four telescopes from March 2025 targeting the dwarf spheroidal galaxy Ursa Major III (a potential dark matter source). This run is chosen to represent a typical VERITAS observation with no significant detection of gamma rays. The third run (number 110277) is another 30-minute observation with all four telescopes targeting the Crab Nebula in December 2024. The Crab Nebula is the brightest consistent source of very-high-energy gamma rays in the sky [28] and so this run is chosen to represent a typical observation with significant detection. All three runs are verified to be of good quality using VERITAS's Data Quality Monitoring database.

Unlike the simulations, the observation runs contain a large cosmic-ray background as well as some gamma-ray signals. Unaware, ED's muon ring analysis attempts to calculate muon ring parameters for all events in a run and succeeds in returning parameters for many images that are in fact from cosmic rays or gamma rays (see Figure 5.7). Fortunately, the distribution of ring radius uncertainties can be used to discard the misidentified muon rings. In all analyzed runs, the distribution reveals three apparent populations of images

reconstructed as "rings" by ED. These distributions are plotted in Figure 7.4. The same cutoff of 0.12° used for the simulation data is applied to the three sets of real data. This quality cut does a good job of separating the true muon images (first population with small peak near 0.07°) from the noise (second population with large central peak near 0.25°). However, a subpopulation of events with small radius, small radius uncertainty, and a wide spread of sizes (in terms of d.c.) survives the 0.12° cutoff. With images spanning no more than six pixels in diameter on the camera plane, it is virtually impossible to distinguish rings from other shapes. These events are likely small showers and not true muons. A conservative cut of requiring the ring radius to be at least 0.4° (corresponding to the Cherenkov angle of a 5.0-GeV muon at VERITAS altitude) removes this subpopulation. The enhancement at 0.40° seen in Figure 7.4 for all three runs seems to come from a third population of events for which ED associates a ring radius near 1.13°–1.16°. Upon inspection, these are found to be large events that trigger nearly every pixel of the camera. Even though an image covering the entire FOV is manifestly not a ring, ED's fit unfortunately succeeds. On the camera plane, the mean distance all 499 pixels have from the centre is close to 1.16°, while the standard deviation of this distance for all pixels is around 0.40°—effectively explaining the sharp peak in radius uncertainty at this value. Ultimately, this population of events is efficiently removed by the quality cuts and is thus not relevant to this work. Table 7.2 presents the important characteristics of the analyzed VERITAS runs and the ring images found as well as those surviving the quality cuts.

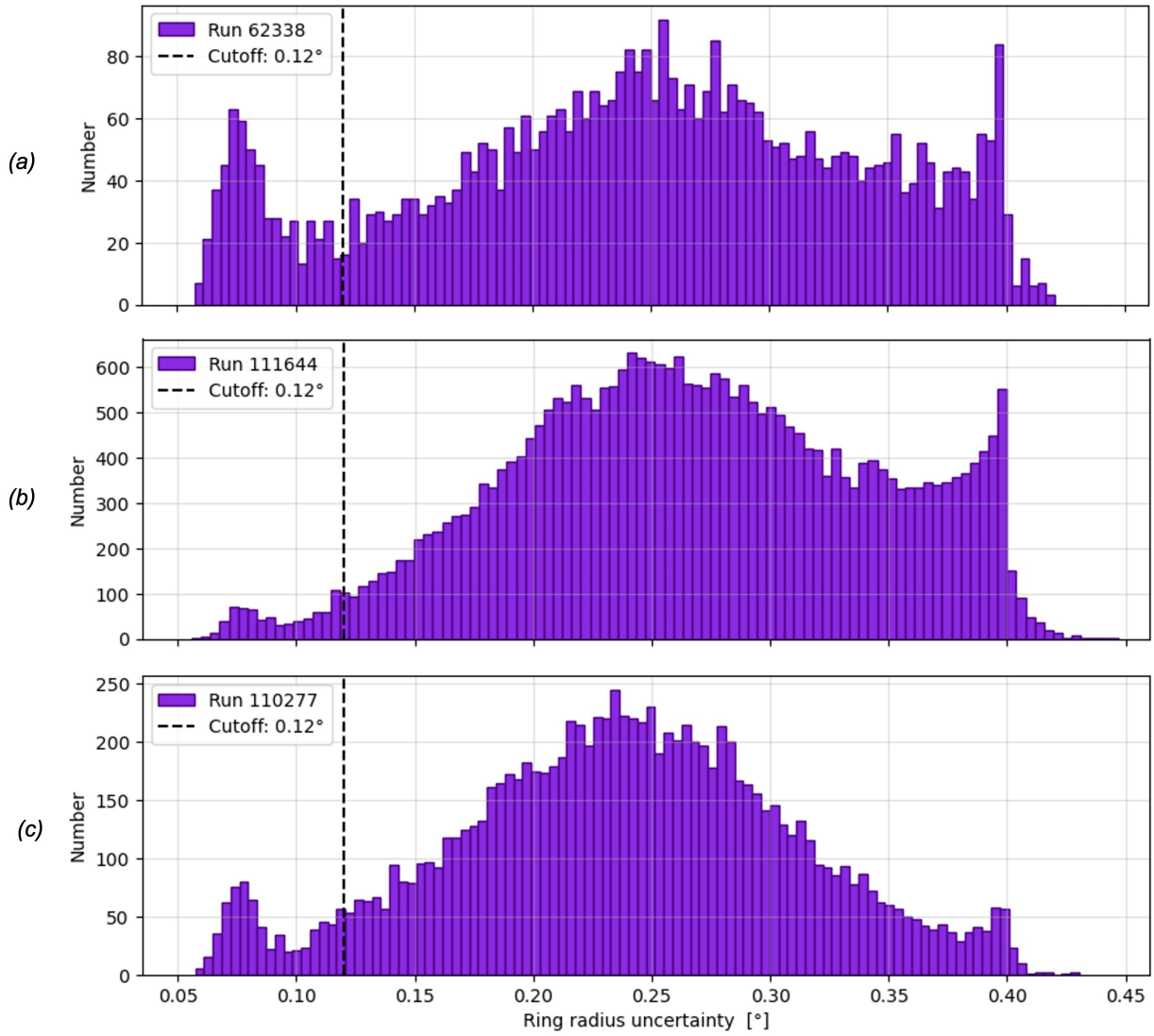

Figure 7.4: Distribution of ring radius uncertainties for reconstructed images in three VERITAS runs. (a) Run 62338 is a single-telescope observation of a dark sky region lasting 20 minutes. (b) Run 111644 is a 30-minute observation of Ursa Major III using all four telescopes. (c) Run 110277 is a 30-minute observation of the Crab Nebula using all four telescopes. In all three distributions, distinct populations of events can be seen, with true muons composing the leftmost peak (compare with Figure 7.2). A cutoff is applied at 0.12° to discard poorly reconstructed rings, thus preserving the true muon events and possibly any candidate monopole events. The enhancement at 0.4° in all three runs comes from events that trigger nearly all pixels in a camera, covering the entire field of view. These events are not rings and are not relevant to this work.

Table 7.2: Ring images analyzed in VERITAS observation runs

Run number	Target	Zenith angle [°]	Telescopes	Runtime [min]	N_{rings} found	N_{rings} after cuts
62338	DARK_044_8.05	20	1	20	4584	468
111644	Ursa Major III	16	4	30	30486	404
110277	Crab Nebula	48	4	30	10316	471

Identically to the procedure with the simulated data, the parameters of the surviving ring images are plotted on a ring radius vs. impact-corrected size graph. Figure 7.5 is the result of this exercise. The higher slope in runs 111644 and 110277 compared to run 62338 is expected because of the PMT upgrade in between them: VERITAS produces more d.c. per photoelectron in the two later runs than in the earlier run. Another interesting difference between the runs is the higher proportion of large rings in both 111644 and 110277 compared to 62338. This is the result of the L3 trigger in the four-telescope runs; lower-energy muons are unlikely to survive the trigger system because they are inherently much more local events. While higher-energy muons have the potential of inducing Cherenkov photons that reach more than one telescope if they are created at high enough altitude (see Figure 5.11), lower-energy muons are much more reliant on coincidence with other events for their images to be recorded by VERITAS. Table 7.2 also reveals the effectiveness of L3 at removing muons, as very few ring images remain after cuts in 111644 and in 110277 despite their longer runtime compared to 62338 and the opportunity for muons to hit any of four telescopes instead of just one. A key point is that the gamma-ray source in 110277 is not an impediment to ED's ability to detect ring images.

The absence of MM candidates is evident in Figure 7.5. This allows the calculation of an upper limit to the flux of ultrarelativistic MMs, based on these runs (see Section 8.2).

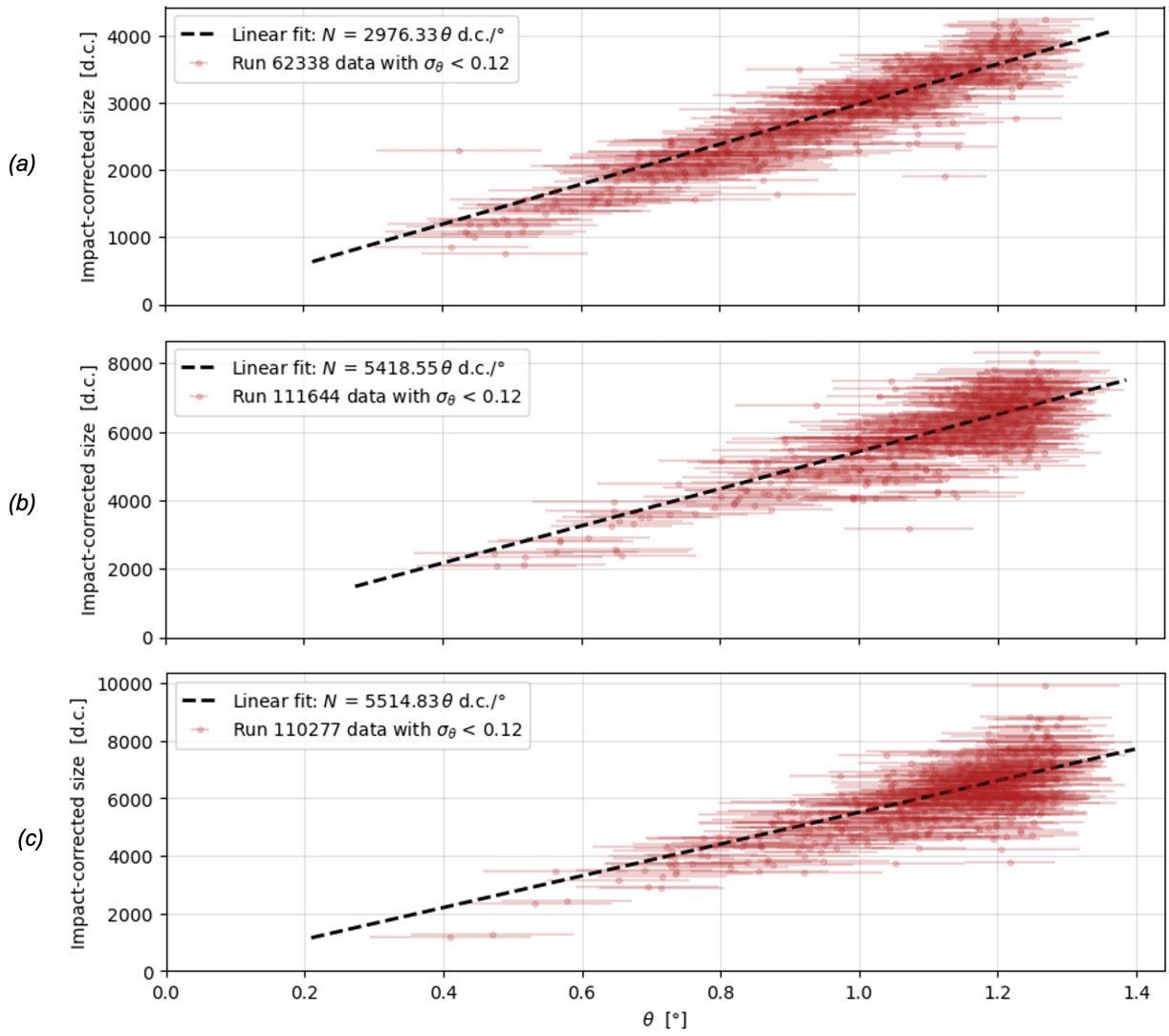

Figure 7.5: Impact-corrected ring size as a function of radius (θ) for well reconstructed images in three VERITAS runs. (a) Run 62338 is a single-telescope observation of a dark sky region lasting 20 minutes. (b) Run 111644 is a 30-minute observation of Ursa Major III using all four telescopes. (c) Run 110277 is a 30-minute observation of the Crab Nebula using all four telescopes. In all datasets, an image is considered well reconstructed if the radius is $\geq 0.4°$ with an uncertainty of $< 0.12°$. A linear fit to the data is plotted (dashed black line). The are no data points lying outside of the plotted region and no identifiable monopole candidates.

Chapter 8

Discussion

8.1 Evaluating the performance of the simulation and of Eventdisplay

Except for the noticeably missing simulated MM (event 4) in all wobble iterations, the simulation reaches completion without major errors. One way to verify that the simulations are produced successfully by `VTS-SimPipe` and processed properly by Eventdisplay (ED) is to look at the distribution of ring radii picked up by the software. The background muons are generated by CORSIKA with a power-law energy distribution described by equation (6.1). Since energy determines speed and therefore Cherenkov angle, the distribution of ring radii can be precisely predicted given the muons' energy distribution*. Given the chosen simulation parameters of an index $\Gamma = 2.7$ for energies between 5.3 and 10^4 GeV, a probability distribution is plotted as the blue curve in Figure 8.1. The area under the curve (between its bounds) is matched to equal the number of well reconstructed muon images found in wobbles 0° to 0.5° (the sum of the first six entries in the "muons after cuts" column in Table 7.1). The curve can then be compared to the actual distribution of these images (red bins in Figure 8.1). Keeping in mind that the curve

*It can be shown that the distribution of muon ring radii must follow

$$\frac{dN}{d\theta} = \frac{N_{\text{total}}\,(\Gamma + 1)}{E_{\text{max}}^{\Gamma+1} - E_{\text{min}}^{\Gamma+1}}\,(m_\mu\,c^2)^{\Gamma+1}\left(1 - \frac{1}{n^2\,\cos^2\theta}\right)^{-1/2\,\Gamma\,-\,3/2}\frac{\tan\theta}{n^2\,\cos^2\theta}\,.$$

does not account for the effects of reconstruction smearing, the distribution appears to align with rudimentary expectations. On the smaller-radius end of the distribution, there seems to be a smaller number of muon images than expected while there are images identified by ED to have a radius smaller than would be formed by a muon at 5.3 GeV. This can be explained in part as energy loss of the lower-energy muons of the simulation. At lower energies, a small loss provokes a big change in Cherenkov angle.

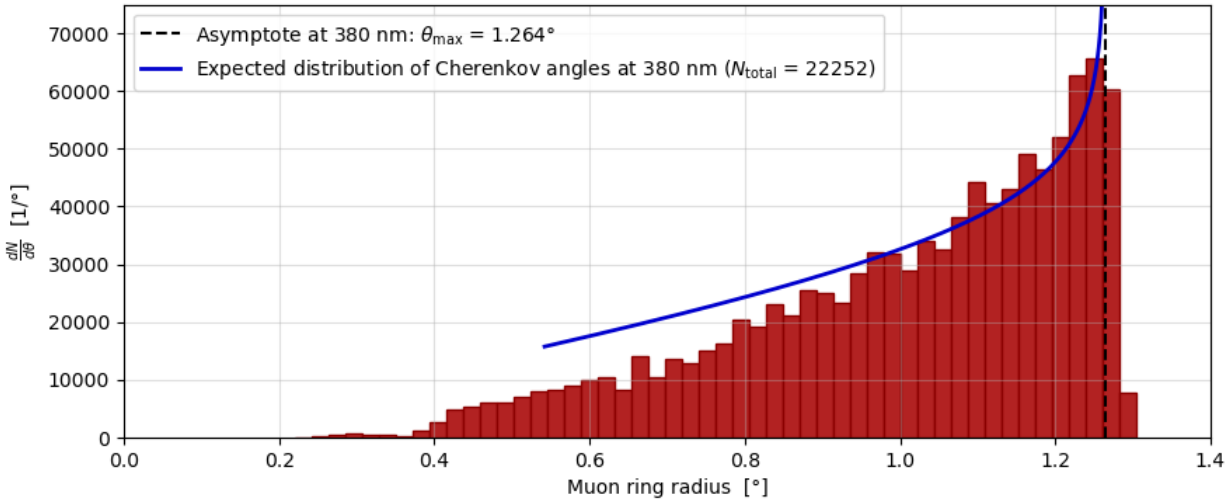

Figure 8.1: Distribution of ring radii of simulated background muons (wobbles 0° to 0.5°). This is a density plot—to obtain the absolute number N in each bin, multiply the y-value by the bin size 0.02°. Only muon ring images which survive quality cuts are shown. The expected distribution (blue curve) is that of a population of muons with energies between 5.3 and 10^4 GeV following a power law with index $\Gamma = 2.7$, with no correction for smearing during the reconstruction step. The total number of muons ($N_{\text{total}} = 22252$) is matched to the number of well reconstructed images across the DL1 files of wobbles 0° to 0.5°.

Although rings and arcs produced by either simulated MMs or background muons are viewable with `evndisp`, the muon option only parametrizes rings that are complete and that are fully enclosed in the camera. This means that arcs ($\xi \geq 1$) are automatically thrown out in the analysis. It also means that the effective area for the detection of MMs

through this method is limited to no more than the area of the VERITAS reflector ($A_{\text{eff}} = \pi\,(600\,\text{cm})^2 \approx 1.1\times10^6\,\text{cm}^2$). Further, any offset angle that shifts an image beyond the edge of the camera is also rejected as the truncated shape can no longer form a closed ring. This limitation is more forgiving to smaller rings because their centres can be shifted farther from the camera centre before they reach the edge of the field of view (FOV). Since all ultrarelativistic MMs are expected to form rings with the largest possible radius of 1.26°, the maximum tolerated offset angle for MMs is no more than $w = 0.5°$—the radius of the VERITAS FOV being 1.75°. For this reason, it is understandable that no simulated MM image is reconstructed in wobbles greater than 0.5°. This limitation constrains the solid angle of the sky from where a cosmic MM can arrive and be detected. The solid angle is thus limited to $\Omega = 2\pi\,(1 - \cos w) \approx 2.4 \times 10^{-4}$ sr.

Even before reaching the hard limits on ξ and on w, ED's performance in parametrizing ring images suffers with increasing impact distance and with increasing offset angle. This can be seen in the numbers presented in Table 7.1. To illustrate the decreasing efficiency as a function of these variables, Figure 8.2(a) shows the total number of simulation images that are well reconstructed by ED for each of the 15 tested wobbles while Figure 8.2(b) shows the proportion of images (combined across wobbles 0° to 0.5°) that are well reconstructed depending on their impact distance as attributed by ED. It is important to recall that each iteration of the simulation gives a set offset angle to the incoming particles while the impact point is simulated at random over an area of a chosen scatter radius. For each wobble, 100,006 events (MMs and muons combined) are generated—the vast majority of which impact outside the reflector and so are not parametrized. In Figure 8.2(b), the number of generated events for each ξ interval is an estimation based on the uniform probability of impact over the scatter area. ED's performance seems rather stable between wobbles 0° to 0.3°, but then dips even before the largest rings (radius 1.26°) are expected to become cropped at $w = 0.5°$. The decreased performance with increasing ξ may be due to the dimming of one part of the ring to the point where the photomultiplier tubes (PMTs) fail to trigger and complete the shape (see how ring intensity varies in azimuth at different ξ in Figure 5.10(a)), and it is reasonable to think that smaller rings are

more susceptible to this. ED's limitations are also seen in the observational data, but it is harder to gauge because the conditions aren't controlled like in the simulation.

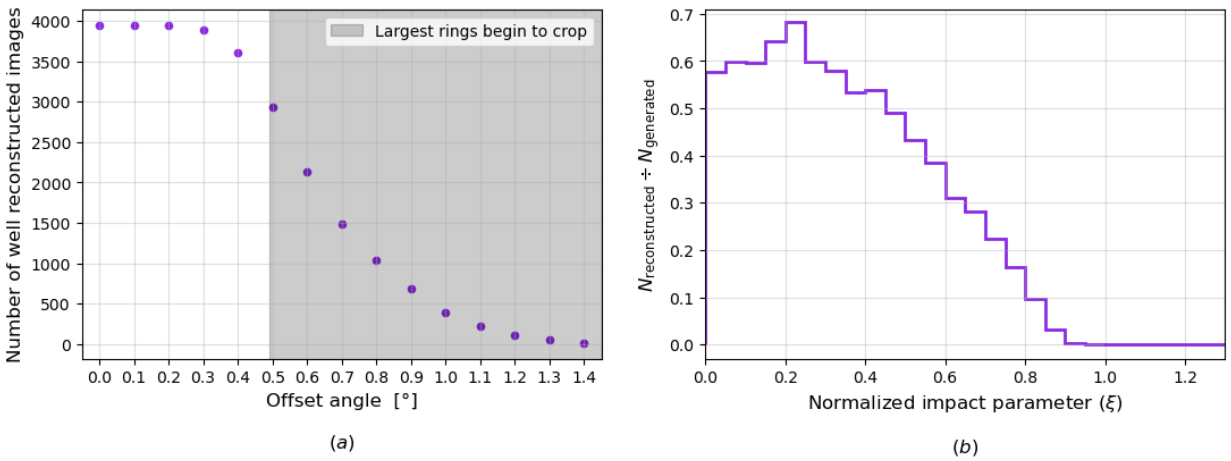

Figure 8.2: Performance of Eventdisplay in the reconstruction of simulation ring images (six monopoles and 100,000 muons combined) dependent on offset angle and impact distance. (a) Total number of well reconstructed images as a function of offset angle with respect to telescope pointing (wobble). The same total number of events (100,006) is generated at every wobble, but the vast majority of these impact outside the reflector and are not reconstructed. The largest ring images have a radius of 1.26° and begin to move off the 3.5° field of view at offsets greater than 0.49° (indicated by the grey shaded region). (b) Proportion of well reconstructed images as a function of the normalized impact parameter ξ as attributed by Eventdisplay. This encompasses all wobbles between 0° and 0.5°. For every ξ interval, the number of generated events is estimated based on uniform probability of impact over a given area. Eventdisplay does not reconstruct arc images ($\xi \geq 1$).

On top of its standard muon option, ED offers another method for finding ring images, based on the Hough transform [76]. Instead of iteratively fitting a ring to the image, the Hough transform method makes use of a voting procedure with a lookup table to find the best ring parameters. The Hough transform method is also limited to finding closed rings that are fully contained in the FOV, but it may offer better performance in identify-

ing rings than the standard method. The parameters returned by the Hough transform method are different than those listed in Section 7.1 and so the possibility of obtaining ring radius and size for the identification of MM candidates with the Hough transform is left for future work.

8.2 Setting an upper limit on the flux of ultrarelativistic magnetic monopoles

After searching through observation runs (62338, 111644, 110277) and finding no MM candidates, the flux of MMs with $\gamma \gtrsim 10^4$ can be constrained by setting a 90% confidence level (C.L.) upper limit obtained by

$$\Phi_{\mathrm{MM}}^{90\%\mathrm{C.L.}} \leq \frac{2.44}{\text{efficiency} \times \text{exposure}} \,. \tag{8.1}$$

The value of 2.44 in the numerator follows from the Feldman–Cousins approach for a Poissonian process with zero background [77]. Exposure is the product of effective area, solid angle observed, and livetime ($A_{\mathrm{eff}}\,\Omega\,t$). However, since the efficiency of ED ($\varepsilon_{\mathrm{ED}}$) is a function of ξ and w, the denominator becomes an integral:

$$\begin{aligned} \text{efficiency} \times \text{exposure} &= t \int_0^{\Omega_{\max}} \int_0^{A_{\max}} \varepsilon_{\mathrm{ED}}(\xi, w)\, dA_{\mathrm{eff}}\, d\Omega \\ &= t\, D^2\, \pi^2 \int_0^{w_{\max}} \int_0^{\xi_{\max}} \xi\, \sin(w)\, \varepsilon_{\mathrm{ED}}(\xi, w)\, d\xi\, dw \,, \end{aligned} \tag{8.2}$$

where D is again the reflector diameter. As discussed in the previous section, $w_{\max}$ and $\xi_{\max}$ are respectively 0.5° and 1.

Ideally, $\varepsilon_{\mathrm{ED}}(\xi, w)$ must be found specifically for the large, bright rings produced by MMs and not for rings with radii and sizes expected of muons. However, it is not feasible to test ED's performance on a large number of monopole events since their simulation is computationally expensive at the GrOptics and CARE levels. The geometry of MM rings is so distinct, with an overall light level so much above the muon background's, that the

additional computational complexity of injecting simulated MMs into a VERITAS data run is also not justified. This refinement is left for a future study. Instead, ED's performance on the simulation of six MMs plus a background of 100,000 muons (as illustrated in Figure 8.2) is used to determine $\varepsilon_{\mathrm{ED}}(\xi, w)$ and should be a good enough placeholder for this exercise. The function $\varepsilon_{\mathrm{ED}}(\xi, w)$ is thus approximated by a 2D interpolation using the proportion of well reconstructed images per ξ per w as an efficiency factor and equation (8.2) can be numerically integrated.

Unlike run 62338 and the simulation in this work, almost all VERITAS observations are done with multiple telescopes and utilize the full trigger system. As discussed in Section 5.6.4 and again in Section 7.2, the L3 trigger is an important barrier to the recording of muon images. However, because of its high Lorentz factor, an ultrarelativistic MM would be able to induce Cherenkov photons at high altitudes that can reach up to 136 m away from its impact point on the ground, assuming the MM travels from 0° zenith (see Figure 5.11). For non-zero zenith angles, the area covered on the ground increases, simply because of the geometry. This means that if a ring is viewable in one telescope because a MM impacts somewhere in its reflector, then there are Cherenkov photons from higher-altitude emission that can also reach other telescopes in the VERITAS array (see Figure 5.3), albeit hitting only a small number of PMTs. Even though the emission at higher altitude is suppressed by the smallness of the Cherenkov angle, MMs are still capable of inducing enough emission to be picked up by the farther telescopes. Moreover, this emission would trigger more than three PMTs in at least one of the farther telescopes and so the MM event would indeed pass the VERITAS trigger system. This is tested with a separate simulation of six MMs descending from an altitude of $\sim$90 km using `VTS-SimPipe`. In this dedicated simulation, the MMs are made to target one telescope and the L3 trigger multiplicity is set to 2 (the usual L3 setting in VERITAS observations). In all wobbles tested, all six MM events pass the full trigger system. This also confirms the work done by Spengler with H.E.S.S., which focused on the pair of bright clusters produced by MMs with high impact parameters [51]. However, the `VTS-SimPipe` simulation does not consistently show the clusters as a pair (some images in the far telescopes

had one or three clusters). Even though the clusters are bright, their inconsistent appearance would make them hard to distinguish from showers and from electronics noise in a VERITAS observation. The search for bright rings has an important limitation with regard to effective area, but these rings are more reliable signatures and would provide more convincing candidates.

Since MM events can plausibly pass the VERITAS trigger system, the analysis of the four-telescope runs 111644 and 110277 does not need to consider the efficiency—or rather the inefficiency—of L3. With four times as many telescopes, the effective area in these two runs is multiplied by 4, compared to single-telescope run. Together, the non-detection of MMs in runs 62338, 111644, and 110277 leads to a 90% C.L. flux upper limit of

$$\Phi_{\mathrm{MM}}^{90\%\mathrm{C.L.}} \leq 1.8 \times 10^{-6}\,\mathrm{cm}^{-2}\,\mathrm{s}^{-1}\,\mathrm{sr}^{-1}\,. \tag{8.3}$$

This is, of course, only a sampling of the search method with three runs totalling less than one and a half hours of observation. The exposure in the three analyzed runs is only 4.1×10^6 cm^2 s sr.

8.3 Potential upper limits achievable with VERITAS and future work

Under the assumption that ultrarelativistic MM events pass the full trigger system, virtually all VERITAS observation runs taken since 2007 are usable in the search for MM candidates using the method described in this work. With ∼14,000 hours of observations, a more constraining limit than (8.3) can be estimated. If no detection is made in ∼14,000 hours and with ED's muon software in its current state, VERITAS could produce a 90% C.L. flux upper limit of

$$\Phi_{\mathrm{MM}}^{90\%\mathrm{C.L.}} \lesssim 1.4 \times 10^{-10}\,\mathrm{cm}^{-2}\,\mathrm{s}^{-1}\,\mathrm{sr}^{-1}\,. \tag{8.4}$$

This limit is still five orders of magnitude higher than the Parker bound.

A more compelling limit with VERITAS will require expanding ED's acceptance of muon images to include arcs as well as cropped images. These are understandably more complex images to process because arcs and ring segments that are too small could be confused for ellipses created by air showers. And while an impact-corrected size can still be recovered for true arcs that are uninterrupted by the edge of the camera (using equation (7.1)), the same is not true for cropped rings. Being incomplete images, the "true" size and centroid position of cropped rings cannot easily be measured or calculated. As a result, cropped rings are of little use for plotting a radius vs. size graph in muon calibrations—and so there may be little motivation to accept these types of images from the perspective of muon studies. Nonetheless, MM images being two orders of magnitude greater in intensity than muon images at a radius of 1.26°, the detection of even a modest segment of a ring can be significant. For the purposes of MM detection, determining a radius with its uncertainty and only a partial size would be sufficient.

If we suppose that the software can be improved to accept arcs and ring segments that cover ten pixels in arc length—i.e., an arc of ∼68° out of 360°, plausibly enough to confidently determine curvature—, the maximum accepted impact becomes $\xi \approx 1.8$ and the maximum accepted offset angle becomes $w \approx 2.6°$. If we assume a modest average (uniform) detection efficiency of 0.6, the 90% C.L. flux upper limit for no detection in the full VERITAS dataset could then reach $\sim 1.0 \times 10^{-13}$ cm^{-2} s^{-1} sr^{-1}. This value accounts for the integrated probability of missing an arc because of the compounding of high impact and high offset. In a much more ambitious scenario of accepting as little as five pixels in arc length (an arc of ∼35°), the maximum impact and offset respectively become $\xi \approx 3.4$ and $w \approx 2.9°$ and a 90% C.L. flux upper limit of $\sim 1.5 \times 10^{-14}$ cm^{-2} s^{-1} sr^{-1} can be achieved.

With optimistic prospective limits still falling short of the Parker bound, it becomes evident that imaging atmospheric Cherenkov telescopes (IACTs) such as VERITAS are disadvantaged in the search for MMs. The requirement of identifying rings (and perhaps arcs)

as an unambiguous signature imposes a limited effective area. At the same time, the small FOV of the pointing instrument provides a minuscule solid angle in each observation. With their limited exposures, IACTs compare unfavourably to neutrino experiments—such as IceCube and ANTARES—that can view essentially the whole sky, have tremendous effective area, and operate on a nearly 100% duty cycle. It is worth pointing out, however, that one important advantage that IACTs have in this search is the fact that MM candidates would land in a background-free region of parameter space. Furthermore, IACTs offer an independent way to constrain the flux of ultrarelativistic MMs, especially in a parameter space that is poorly explored by previous studies (see Figure 4.1).

All IACT experiments are familiar with muon rings and possess software for their detection and characterization [68]. The method described here can therefore easily be exported to other IACTs. One interesting possibility is combining the VERITAS dataset with that of the other two current major IACT experiments, H.E.S.S. and MAGIC (the Major Atmospheric Gamma Imaging Cherenkov Telescopes, located in La Palma, Spain) [78], to do a combined search with the potential of producing a more constraining flux upper limit.

In the near future, CTAO will be the largest IACT array studying very-high-energy gamma rays. The array is planned to be composed of over 60 telescopes of three different sizes, spread across two sites (CTAO-North in La Palma, Spain, and CTAO-South in Paranal, Chile) [66]. The "Small-Sized Telescope" will have a primary reflector that is only 4.3 m in diameter but will offer a 9° FOV. The "Medium-Sized Telescope" will have a 12-m reflector and an 8° FOV. Finally, the reflector of the "Large-Sized Telescope" will be 23 m in diameter and its FOV will be 4.3°. With its decades-long operations, CTAO will achieve a much higher exposure in the search for MMs than VERITAS has. CTAO shows a lot of promise for the detection for ultrabright rings and arcs produced by ultrarelativistic monopoles.

Chapter 9

Conclusions

The term "magnetic monopoles" (MMs) refers to particles that possess an isolated magnetic charge (either north or south), but the existence of such particles has yet to be experimentally verified. Searches for MMs are motivated by the symmetry they would bring to Maxwell's equations and by the justification they would provide for the quantization of electric charge. Although classical MMs (light elementary particles) have largely been ruled out by collider experiments, the flux of very massive composite MMs of cosmic origin has not been fully constrained. These types of monopoles—classified as Grand Unified Theory (GUT) MMs or as intermediate-mass MMs (IMMs)—are a prediction of GUTs [6,7].

So far, the most constraining searches for cosmic MMs have been performed with neutrino and cosmic-ray experiments. These experiments have the advantage of operating on a nearly 100% duty cycle, being able to observe essentially the whole sky, and possessing a very large effective area for detection. With no MM candidate found in the data initially collected for the study of neutrinos and cosmic rays, these searches have produced 90% confidence level (C.L.) upper limits of around 10^{-20}–10^{-17} cm^{-2} s^{-1} sr^{-1} and even lower, depending on monopole parameters such as mass and speed. In general, searches with neutrino experiments have relied on the fact that MMs are expected to induce much more Cherenkov radiation than an electrically charged lepton of the same speed [2]. In water

and ice, MMs are responsible for the emission of ∼8300 times more Cherenkov photons. In air, this number is ∼4700.

The Very Energetic Radiation Imaging Telescope Array System (VERITAS), designed for the study of very-high-energy (VHE) gamma rays, can also participate in the search for MMs. Cosmic IMMs with masses up to 10^8 GeV/c^2 are able to reach Lorentz factors of 10^3 and beyond as they are accelerated by galactic magnetic fields [8,9]. The behaviour of these ultrarelativistic MMs in Earth's atmosphere should be very comparable to that of high-energy muons, which traverse the atmosphere with little energy loss and remain stable as they reach the ground. VERITAS constantly receives a large amount of noise from muons, which shows up as ring and arc images in the data, and is able to identify and parametrize these images. In the case of muons, the intensity of the ring image is very tightly related to the ring radius, such that a clear linear relationship can be drawn between the two parameters after accounting for the muon's impact point [67]. The simulations made in the context of this work confirm that MM images would be similar in appearance to muon images but would have digital counts around ∼100 times greater when detected and processed by VERITAS software. In the parameter space of ring radius and impact-corrected size (intensity), MM rings appear in a background-free region far above muon rings. The simulations are done using CORSIKA plus two VERITAS simulation programs—GrOptics and CARE—and involve six MMs with a Lorentz factor $\gamma \sim 10^4$ compared to a background of 100,000 muons with a distribution of energies, all impacting in or near a single telescope of the array at 15 different offset angles with respect to the telescope pointing.

Three VERITAS observation runs (a 20-minute single-telescope run and two 30-minute four-telescope runs) are analyzed using the same quality cut as the simulation analysis. With no MM candidate found in any of the runs, a 90% C.L. flux upper limit is set at 1.8×10^{-6} cm^{-2} s^{-1} sr^{-1}. This is a very weak constraint because of the limited time of the observation sample. Other important limitations are the effective area and solid angle which do not exceed $A_{\text{eff}} \approx 1.1 \times 10^6\ \text{cm}^2$ and $\Omega \approx 2.4 \times 10^{-4}$ sr respectively. These are

limitations imposed by the software, related to the inability to accept images that are not closed rings fully contained in the VERITAS field of view (FOV).

With improvements to the muon image detection software, the analysis of the full VERITAS dataset (∼14,000 hours) could optimistically produce a 90% C.L. flux upper limit as low as 1.5×10^{-14} cm^{-2} s^{-1} sr^{-1}. This is however still higher than the theoretical constraint imposed by the persistence of galactic magnetic fields (the Parker bound), considered to be 10^{-15} cm^{-2} s^{-1} sr^{-1}. Nonetheless, VERITAS presents an independent method for searching for MMs—especially with γ between 10^4 and 10^6, which is a parameter space less well constrained in previous searches. In the future, the next-generation VHE gamma-ray observatory CTAO (the Cherenkov Telescope Array Observatory) will provide better opportunities to constrain the flux of ultrarelativistic MMs thanks to its larger effective area, larger FOV, and greater number of telescopes.

Bibliography

[1] D. J. Griffiths, "Chapter 7 – Electrodynamics," in *Introduction to Electrodynamics*, pp. 296–354, Prentice Hall, 4th ed., 2017.

[2] D. R. Tompkins, "Total energy loss and Čerenkov emission from monopoles," *Phys. Rev.*, vol. 138, pp. B248–B250, Apr. 1965.

[3] D. Hack, J. Knapp, J. N. Capdevielle, G. Schatz, and T. Thouw, "CORSIKA: A Monte Carlo code to simulate extensive air showers," *Forschungszentrum Karlsruhe Report FZKA 6019*, 1998.

[4] K. A. Milton, "Theoretical and experimental status of magnetic monopoles," *Rep. Prog. Phys.*, vol. 69, p. 1637–1711, May 2006.

[5] P. A. M. Dirac, "Quantised singularities in the electromagnetic field," *Proc. R. Soc. Lond.*, vol. 133, pp. 60–72, 1931.

[6] G. 't Hooft, "Magnetic monopoles in unified gauge theories," *Nucl. Phys. B*, vol. 79, pp. 276–284, 1974.

[7] A. M. Polyakov, "Particle spectrum in quantum field theory," *JETP Lett.*, vol. 20, pp. 194–195, 1974.

[8] L. Patrizii and M. Spurio, "Status of searches for magnetic monopoles," *Annu. Rev. Nucl. Part. Sci.*, vol. 65, pp. 279–302, Oct. 2015.

[9] L. Patrizii, Z. Sahnoun, and V. Togo, "Searches for cosmic magnetic monopoles: past, present and future," *Phil. Trans. R. Soc. A*, vol. 377, p. 20180328, Dec. 2019.

[10] B. Acharya, J. Alexandre, S. Baines, P. Benes, B. Bergmann, J. Bernabéu, *et al.*, "Search for magnetic monopoles with the MoEDAL forward trapping detector in 2.11 fb^{-1} of 13 TeV proton–proton collisions at the LHC," *Phys. Lett. B*, vol. 782, pp. 510–516, 2018.

[11] B. W. Carroll and D. A. Ostlie, "Chapter 30 – The Early Universe," in *An Introduction to Modern Astrophysics*, pp. 1230–1278, Pearson, 2nd ed., 2014.

[12] B. W. Carroll and D. A. Ostlie, "Chapter 27 – The Structure of the Universe," in *An Introduction to Modern Astrophysics*, pp. 1038–1084, Pearson, 2nd ed., 2014.

[13] E. N. Parker, "The origin of magnetic fields," *ApJ*, vol. 160, p. 383, May 1970.

[14] M. S. Turner, E. N. Parker, and T. J. Bogdan, "Magnetic monopoles and the survival of galactic magnetic fields," *Phys. Rev. D*, vol. 26, pp. 1296–1305, Sept. 1982.

[15] F. C. Adams, M. Fatuzzo, K. Freese, G. Tarlé, R. Watkins, and M. S. Turner, "Extension of the Parker bound on the flux of magnetic monopoles," *Phys. Rev. Lett.*, vol. 70, pp. 2511–2514, Apr. 1993.

[16] R. Abbasi, Y. Abdou, T. Abu-Zayyad, J. Adams, J. A. Aguilar, M. Ahlers, *et al.*, "Search for relativistic magnetic monopoles with the AMANDA-II neutrino telescope," *Eur. Phys. J. C*, vol. 69, pp. 361–378, Oct. 2010.

[17] D. P. Hogan, D. Z. Besson, J. P. Ralston, I. Kravchenko, and D. Seckel, "Relativistic magnetic monopole flux constraints from RICE," *Phys. Rev. D*, vol. 78, p. 075031, Oct. 2008.

[18] M. Detrixhe, D. Besson, P. W. Gorham, P. Allison, B. Baughmann, J. J. Beatty, *et al.*, "Ultrarelativistic magnetic monopole search with the ANITA-II balloon-borne radio interferometer," *Phys. Rev. D*, vol. 83, p. 023513, Jan. 2011.

[19] S. I. Dutta, M. H. Reno, I. Sarcevic, and D. Seckel, "Propagation of muons and taus at high energies," *Phys. Rev. D*, vol. 63, p. 094020, Apr. 2001.

[20] R. L. Workman, V. D. Burkert, V. Crede, E. Klempt, U. Thoma, *et al.*, "Review of particle physics," *Prog. of Theor. and Exp. Phys.*, vol. 2022, p. 083C01, Aug. 2022.

[21] M. F. L'Annunziata, "Chapter 13 – Electromagnetic Radiation: photons," in *Radioactivity*, pp. 709–746, Elsevier, 3rd ed., 2023.

[22] A. Aab, P. Abreu, M. Aglietta, I. Al Samarai, I. F. M. Albuquerque, I. Allekotte, *et al.*, "Search for ultrarelativistic magnetic monopoles with the Pierre Auger observatory," *Phys. Rev. D*, vol. 94, p. 082002, Oct. 2016.

[23] Particle Data Group, "Atomic and nuclear properties of air (dry, 1 atm)." `https://pdg.lbl.gov/2014/AtomicNuclearProperties/HTML/air_dry_1_atm.html`.

[24] S. P. Ahlen, "Stopping-power formula for magnetic monopoles," *Phys. Rev. D*, vol. 17, pp. 229–233, Jan. 1978.

[25] S. Navas, C. Amsler, T. Gutsche, C. Hanhart, J. J. Hernández-Rey, C. Lourenço, *et al.*, "Review of particle physics," *Phys. Rev. D*, vol. 110, p. 030001, Aug. 2024.

[26] R. M. Sternheimer and R. F. Peierls, "General expression for the density effect for the ionization loss of charged particles," *Phys. Rev. B*, vol. 3, pp. 3681–3692, June 1971.

[27] S. P. Ahlen and K. Kinoshita, "Calculation of the stopping power of very-low-velocity magnetic monopoles," *Phys. Rev. D*, vol. 26, pp. 2347–2363, Nov. 1982.

[28] T. C. Weekes, *Very High Energy Gamma-Ray Astronomy*. Institute of Physics, 2003.

[29] P. A. Cherenkov, "Visible luminescence of pure liquids under the influence of γ-radiation," *Dokl. Akad. Nauk SSSR*, vol. 2, no. 8, pp. 451–454, 1934.

[30] Nobel Prize Outreach 2025, "Nobel Prize in Physics 1958." `https://www.nobelprize.org/prizes/physics/1958/summary/`.

[31] I. M. Frank and I. Y. Tamm, "Coherent visible radiation of fast electrons passing through matter," *Comptes Rendus (Dokl.) Acad. Sci. URSS*, vol. 14, pp. 109–114, 1937.

[32] G. Vacanti, P. Fleury, Y. Jiang, E. Paré, A. Rovero, X. Sarazin, *et al.*, "Muon ring images with an atmospheric Čerenkov telescope," *Astropart. Phys.*, vol. 2, pp. 1–11, Feb. 1994.

[33] A.-L. Cauchy, "Sur la réfraction et la réflexion de la lumière," *Bulletin de Férussac*, vol. 14, pp. 6–10, 1830.

[34] B. J. Skinner and B. Murck, "Chapter 11 – The Atmosphere," in *The Blue Planet*, pp. 321–346, John Whiley & Sons, 3rd ed., 2011.

[35] R. Abbasi, M. Ackermann, J. Adams, J. A. Aguilar, M. Ahlers, M. Ahrens, *et al.*, "Search for relativistic magnetic monopoles with eight years of IceCube data," *Phys. Rev. Lett.*, vol. 128, p. 051101, Feb. 2022.

[36] B. Cabrera, "First results from a superconductive detector for moving magnetic monopoles," *Phys. Rev. Lett.*, vol. 48, pp. 1378–1381, May 1982.

[37] A. Franklin and R. Laymon, "Chapter 8 – The Search for the Magnetic Monopole," in *Once Can Be Enough*, pp. 159–170, Springer, 2021.

[38] M. Ambrosio, R. Antolini, G. Auriemma, D. Bakari, A. Baldini, G. C. Barbarino, *et al.*, "Final results of magnetic monopole searches with the MACRO experiment," *Eur. Phys. J. C*, vol. 25, pp. 511–522, Nov. 2002.

[39] M. Ambrosio, R. Antolini, G. Auriemma, D. Bakari, A. Baldini, G. Barbarino, and B. o. Barish, "Search for nucleon decays induced by GUT magnetic monopoles with the MACRO experiment," *Eur. Phys. J. C*, vol. 26, pp. 163–172, Dec. 2002.

[40] S. Balestra, S. Cecchini, M. Cozzi, M. Errico, F. Fabbri, G. Giacomelli, *et al.*, "Magnetic monopole search at high altitude with the SLIM experiment," *Eur. Phys. J. C*, vol. 55, pp. 57–63, May 2008.

[41] IceCube Collaboration, "IceCube website." `https://icecube.wisc.edu/science/icecube/`.

[42] M. Tanabashi, K. Hagiwara, K. Hikasa, K. Nakamura, Y. Sumino, F. Takahashi, *et al.*, "Review of particle physics," *Phys. Rev. D*, vol. 98, p. 030001, Aug. 2018.

[43] J. S. Faughn and R. A. Serway, *College Physics*. Thomson Learning, 6th ed., 2003.

[44] V. Aynutdinov, A. Avrorin, V. Balkanov, I. Belolaptikov, N. Budnev, I. Danilchenko, *et al.*, "Search for relativistic magnetic monopoles with the Baikal neutrino telescope," *Astropart. Phys.*, vol. 29, pp. 366–372, July 2008.

[45] Baikal Neutrino Observatory, "BDUNT website." `https://www.inr.ru/eng/ebgnt.html`.

[46] K. Ueno, K. Abe, Y. Hayato, T. Iida, K. Iyogi, J. Kameda, *et al.*, "Search for GUT monopoles at Super–Kamiokande," *Astropart. Phys.*, vol. 36, pp. 131–136, Aug. 2012.

[47] M. G. Aartsen, K. Abraham, M. Ackermann, J. Adams, J. A. Aguilar, M. Ahlers, *et al.*, "Searches for relativistic magnetic monopoles in IceCube," *Eur. Phys. J. C*, vol. 76, p. 133, Mar. 2016.

[48] A. Albert, S. Alves, M. André, M. Ardid, S. Ardid, J.-J. Aubert, *et al.*, "Search for magnetic monopoles with the complete ANTARES dataset," May 2025.

[49] Pierre Auger Collaboration, "Pierre Auger Observatory website." `https://www.auger.org/`.

[50] H.E.S.S. Collaboration, "H.E.S.S. website." `https://www.mpi-hd.mpg.de/HESS/`.

[51] G. Spengler, "Signatures of ultrarelativistic magnetic monopoles in imaging Cherenkov telescopes," Master's thesis, Humboldt-Universität zu Berlin, 2009.

[52] G. Spengler and U. Schwanke, "Signatures of ultrarelativistic magnetic monopoles in imaging atmospheric Cherenkov telescopes," in *32nd International Cosmic Ray Conference*, 2011.

[53] VERITAS Collaboration, "VERITAS website." `https://veritas.sao.arizona.edu/`.

[54] J. Holder, "Atmospheric cherenkov gamma-ray telescopes," 2015.

[55] D. Hanna, S. O'Brien, and T. Rosin, "Studies of VERITAS photomultipliers after eight years of use," *Nucl. Instrum. Methods Phys. Res. A*, vol. 1027, p. 166235, Mar. 2022.

[56] Hamamatsu Photonics K.K., "Photomultiplier Tubes [info sheet]," 2020. https://www.hamamatsu.com/content/dam/hamamatsu-photonics/sites/documents/99_SALES_LIBRARY/etd/PMT_TPMZ0002E.pdf.

[57] D. B. Kieda, "The gamma ray detection sensitivity of the upgraded VERITAS observatory," in *33rd International Cosmic Ray Conference*, 2013.

[58] A. Acharyya, C. B. Adams, P. Bangale, J. T. Bartkoske, P. Batista, W. Benbow, *et al.*, "Indirect search for dark matter with a combined analysis of dwarf spheroidal galaxies from VERITAS," *Phys. Rev. D*, vol. 110, p. 063034, Sep. 2024.

[59] A. Weinstein, "The VERITAS trigger system," in *30th International Cosmic Ray Conference*, 2007.

[60] J. Hall, V. V. Vassiliev, D. B. Kieda, J. Moses, T. Nagai, and J. Smith, "VERITAS CDFs," in *28th International Cosmic Ray Conference*, pp. 2851–2854, 2003.

[61] M. Lundy, "Summer Undergrad Meeting 2 [presentation]," 2023.

[62] A. M. Hillas, "Differences between gamma-ray and hadronic showers," *Space Sci. Rev.*, vol. 75, pp. 17–30, 1996.

[63] VERITAS Collaboration, "Eventdisplay git repository." https://github.com/VERITAS-Observatory/EventDisplay_v4.

[64] VERITAS Collaboration, "VEGAS git repository [private]." https://github.com/VERITAS-Observatory/VEGAS.

[65] A. Donath, R. Terrier, Q. Remy, A. Sinha, C. Nigro, F. Pintore, *et al.*, "Gammapy: A Python package for gamma-ray astronomy," *A&A*, vol. 678, p. A157, 2023.

[66] CTAO Collaboration, "CTAO website." https://www.ctao.org/.

[67] S. Fegan and V. Vassiliev, "Analysis of muon images for VERITAS," Mar. 2007.

[68] M. Gaug, S. Fegan, A. Mitchell, M.-C. Maccarone, T. Mineo, and A. Okumura, "Using muon rings for the calibration of the cherenkov telescope array: A systematic review of the method and its potential accuracy," *ApJS*, vol. 243, p. 11, July 2019.

[69] G. Maier, "`VTS-SimPipe` git repository." `https://github.com/VERITAS-Observatory/VTS-SimPipe`.

[70] C. Duke, "GrOptics git repository." `https://github.com/groptics/GrOptics`.

[71] A. N. Otte, "CARE git repository." `https://github.com/nepomukotte/CARE`.

[72] D. Heck and T. Pierog, "Extensive Air Shower Simulation with CORSIKA: A User's Guide," 2024.

[73] T. Antoni, W. D. Apel, F. Badea, K. Bekk, A. Bercuci, H. Blümer, , *et al.*, "The cosmic-ray experiment KASCADE," *Nucl. Instrum. Methods Phys. Res. A*, vol. 513, no. 3, pp. 490–510, 2003.

[74] C. Duke and A. Okumura, "GrOptics User's Guide Version 2.2," 2012.

[75] K. Bernlöhr, "Cherenkov Light in CORSIKA [presentation]," 2005.

[76] J. Tyler, "Muon identification with VERITAS using the Hough transform," Oct. 2012.

[77] G. J. Feldman and R. D. Cousins, "Unified approach to the classical statistical analysis of small signals," *Phys. Rev. D*, vol. 57, pp. 3873–3889, Apr. 1998.

[78] MAGIC Collaboration, "MAGIC website." `http://www.magic.iac.es/`.